DEVELOPMENT OF BIO-NANOTECHNOLOGY SYSTEMS FOR SERS BASED DETECTION OF BIO-MOLECULES

A Dissertation

Presented to the Faculty of the Graduate School

of Cornell University

In Partial Fulfillment of the Requirements for the Degree of

Doctor of Philosophy

by

Adam Joseph Lowe

August 2011

DEVELOPMENT OF BIO-NANOTECHNOLOGY SYSTEMS FOR SERS BASED DETECTION OF BIO-MOLECULES

Adam Joseph Lowe, Ph.D.

Cornell University 2011

Targeted detection of bio-molecules *in vivo* and in the environment is a key area of research. Surface enhanced Raman spectroscopy (SERS) is emerging as a non-invasive platform for detection of a large variety of biomolecules. Here, bio-nanotechnology was investigated to further enhance the capabilities of SERS as a bio-sensor platform. Specifically, a system was developed using oligonucleotide labeled nanoparticles for multiplex detection of small nucleotide polymorphisms in the K-Ras oncogene at a 10 pM detection limit. The binding kinetics and fluorescence quenching of CTAB coated gold nanorods were also investigated for use in detection of hydrophobic biomolecules. Fluorescence quenching of Nile Red and IR-786 was found to be independent of binding affinity, as determined by surface plasmon resonance. A novel method of functionalizing proteins to nanoparticles was developed for use in SERS and other nanoparticles based platforms. The system uses selenocysteine mediated cleavage of a protein splicing element known as an intein. The selenocysteine activated protein can then be functionalized to any selenocysteine reactive surface or functional group in a pH dependent manner. After development using a maltose binding protein model, fluorescein labeling of an intein tagged single chain antibody against the A33 cancer antigen was confirmed by florescence activated cell sorting.

BIOGRAPHICAL SKETCH

Adam Joseph Lowe was born on February 12th, 1985 in Salisbury, MD to Wayne Wingate Lowe and Susan Harshman Lowe. He grew up on the Eastern Shore of Maryland, nestled between the Chesapeake Bay and the Atlantic Ocean. Adam attended Salisbury Christian School from kindergarten through 12th grade, graduating valedictorian and received the Joshua Leadership Award. He went on to graduate from Salisbury University *Summa Cum Laude* in December 2006, completing his Bachelors of Science in Biology in three and a half years. While at SU, Adam was awarded the Wallace Q. French Memorial Environmental Scholarship, was inducted into the Phi Kappa Phi Honor Society, participated in the NSF REU program at Cold Spring Harbor Labs, and won the Biology Faculty Award.

Adam began his PhD in Microbiology from Cornell University in the fall of 2007 after being admitted as a Presidential Life Sciences Fellow. After three rotations, he chose to work for Prof. Carl Batt on applied biotechnology. In addition to his research, Adam worked in the Ludwig Institute for Cancer Research Bio-Production Facility. There he helped produce the cancer vaccines SM-14, NY-ESO-1, and Melan-A. Adam also worked with the Johnson school as the Chair of the Technology Advisory Board for the Big Red Venture Capital Fund. While in Ithaca, Adam enjoyed his friends, the occasional warm days Ithaca provides, and the Chapter House. Upon graduation, Adam was hired as a Principal Research Scientist for SRC Inc. in Syracuse, NY.

To my parents, who gave me the foundation upon which I have built everything.

ACKNOWLEDGMENTS

I would like to gratefully acknowledge Prof. Carl Batt for allowing me to work in his lab and for his mentorship during my tenure as a graduate student. While I learned many academic lessons as Cornell, I think the sage advice Carl gave me about life and how science really works will stick with me for much longer. I would also like to acknowledge my minor advisors Prof. Linda Nicholson and Prof. Matt DeLisa for always being willing to talk about science and open to bounce ideas off of. It is also important that I acknowledge Dr. Aaron Strickland for his help and friendship while he was with the lab.

I want to thank the Ludwig team of Cameron, Kyle, Jack, Rishard, Deuce, and Leo D. I really enjoyed the camaraderie and learned a lot from you all. A special acknowledgement goes to Cameron who worked shifts with me for 48 hours straight to get through Melan-A production.

Finally, I would like to acknowledge my friends and family who helped me get through what was sometimes a bumpy road. Specifically, I want to acknowledge my fiancée Nicholle for her never-ending love and support, even when it meant waking her up at 3 AM so I could go back to the facility. I also want to acknowledge Jennifer Nelson, Brian Forster, and Eric Strobel for always being willing to listen about another failed experiment or my latest and greatest idea.

TABLE OF CONTENTS

CHAPTER 1

DESIGNING FUNCTIONALIZED METALLIC NANOMATERIALS FOR SENSING BIO-MOLECULES BY SURFACE ENHANCED RAMAN SPECTROSCOPY

Abstract

This brief literature review addresses the key points of consideration when designing a surface enhanced Raman spectroscopy (SERS) based system for sensing bio-molecules. It begins by briefly explaining the history of Raman spectroscopy and the mechanisms behind the surface enhancement effect. Within this section, the review also addresses the excitation wavelength and distance dependence of SERS. It also discusses surface enhanced resonance Raman spectroscopy (SERRS), and tip enhanced Raman spectroscopy (TERS) as specialized SERS platforms. The review then analyzes Raman enhancer and surface functionalization choices as key design elements. Finally, the review concludes with previous applications of SERS, demonstrating its ability to function as a bioanalytical tool in a variety of roles.

Introduction & Essential SERS Principles

Raman Spectroscopy is the study of inelastic scattering of light, where a molecule is excited to a virtual state, then relaxes to a vibrational state slightly higher or lower in energy than its original ground state. This phenomena was first observed in the late 1920s[(1)] by Sir C.V. Raman for whom the field gained its namesake. Surface enhanced Raman spectroscopy (SERS) was accidentally discovered in 1974[(2)] when a group was studying pyridine absorbed onto a roughened silver substrate. The large amplification in Raman signal could not be accounted for by an increased number of molecules due to the larger surface area after surface roughening. From there, subsequent studies began to understand how nanostructured metals could enhance Raman signals, and realized the significance of SERS as an analytical tool.

Recent studies have revealed a two-part mechanism contributes to SERS enhancement.[(3-7)] First, SERS enhancers contribute to signal amplification electronically. An energy source excites the electron clouds of colloidal metals or other nanostructures, inducing a localized field of energy called a plasmon. Figure 1-1A shows the electric field and shift in the electron cloud that is propagated across two excited nanoparticles. Figure 1-1B diagrams the extinction efficiency of the field, plotting the ratio of particle cross section against the effective area of the field for a 35 nm Ag nanoparticle. $|E|^2$ denotes the absolute enhancement field intensity. The reason this shift occurs is the polarizability of the nanoparticles, which cannot occur in bulk materials.[(8-10)] The polarizability in turn comes from the incredibly high surface to area ratio and small size of nanostructures.[(11)] This "quantum" size effect occurs when

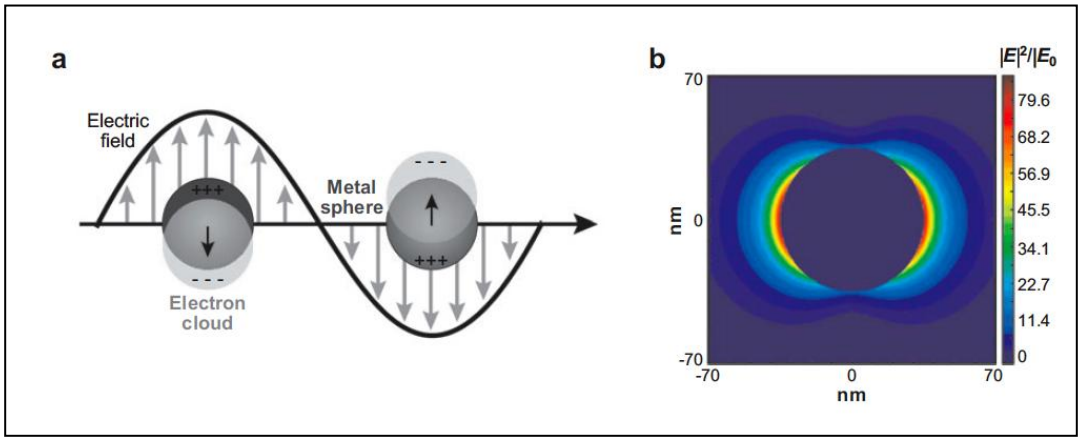

Figure 1-1 (*a*) Illustration of the localized surface plasmon resonance effect. (*b*) Extinction efficiency (ratio of cross section to effective area) of a spherical silver nanoparticle of 35-nm radius in vacuum. $|E|^2$ (absolute field enhancement) contours are shown for a wavelength corresponding to the plasmon extinction maximum, illustrating the strong distance dependence of enhancement. Peak $|E|^2$ = 85.

a gap forms between the valence electrons and the conducting electrons in the metal, which cannot occur in bulk form of the metal.[12] While theoretical and experimental evidence has shown that the electronic effect is the dominant contributor to SERS enhancement[13-15], a chemical enhancement[16] also occurs which is multiplicative[13] with the electronic enhancement. Chemical enhancement works by allowing charge transfer through the metallic surface to go from the highest occupied molecular orbital (HOMO) to the lowest unoccupied molecular orbital (LUMO) of the absorbed molecule, costing only half the energy required to go directly from the HOMO to LUMO energy levels.[13, 17] More recently, this has been further confirmed by detailed study of charge transfer of substituted pyridine rings, which found that chemical enhancement was mainly governed by the distance between HOMO and LUMO orbitals, and not the dipole moments induced by charge transfer from the pyridine ring to its substituted groups.[16]

It is important to note that the enhancement effects described here are dependent on distance and excitation wavelength.[18] It has been empirically determined that SERS enhancement is 10^{th} power dependent on distance from the enhancing field of the metal, thus SERS enhancement greatly drops as the absorbate moves away from the metal.[19, 20] Practically, this is also very important when trying to get a clear Raman signal using a fluorescent Raman reporter. While fluorophores often make excellent Raman reporters due to their high Raman active cross-sections, if they are not properly quenched, the fluorescence can overpower the Raman signal. In close proximity metals such as gold and silver can quench fluorescence,[12, 17, 21-26] while at intermediate distances, metal can actually enhance fluorescence.[27-30] The exact distances depend on both the fluorophore and the substrate. Consideration of these effects is key however when designing a SERS biosensing system that uses

fluorophore labeled detection. A typical setup for a SERS biosensor can be seen in Figure 1-2. Antibodies capture the biological target of interest onto a surface. The basal substrate (shown in gold) can then act as an enhancer or affinity labeled tags (silver spheres) can be added to provide SERS enhancement. These same tags can be labeled with Raman active substrates to provide a diagnostic signal if the intrinsic Raman signal of the biological target is too weak.

Excitation wavelength is also an important factor when designing a SERS biosensor because it may directly affect the degree of signal enhancement.[31, 32] A wavelength must be chosen that maximizes localized surface plasmon resonance absorbance while minimizing absorbance of the bulk metal. Since most Raman spectrophotometers have limited excitation wavelength choices, a general rule is that silver provides better Raman scattering at shorter wavelengths (485 nm- 532 nm) while gold provides better scattering in at longer wavelengths such as 785 nm. Aggregated colloids and engineered nanostructures with multiple or broad plasmon bands can often ignore excitation wavelength considerations as they provide excellent scattering across a range of excitation wavelengths.[33] Additionally, when the excitation wavelength induces an electronic transition in the analyte, its chemical enhancement of Raman scattering is often more significant than optimizing the localized surface plasmon resonance (LSPR) of the Raman enhancing substrate. This phenomena is known as surface enhanced resonance Raman spectroscopy (SERRS) and can often provide much larger signal enhancement than traditional SERS.[34, 35]

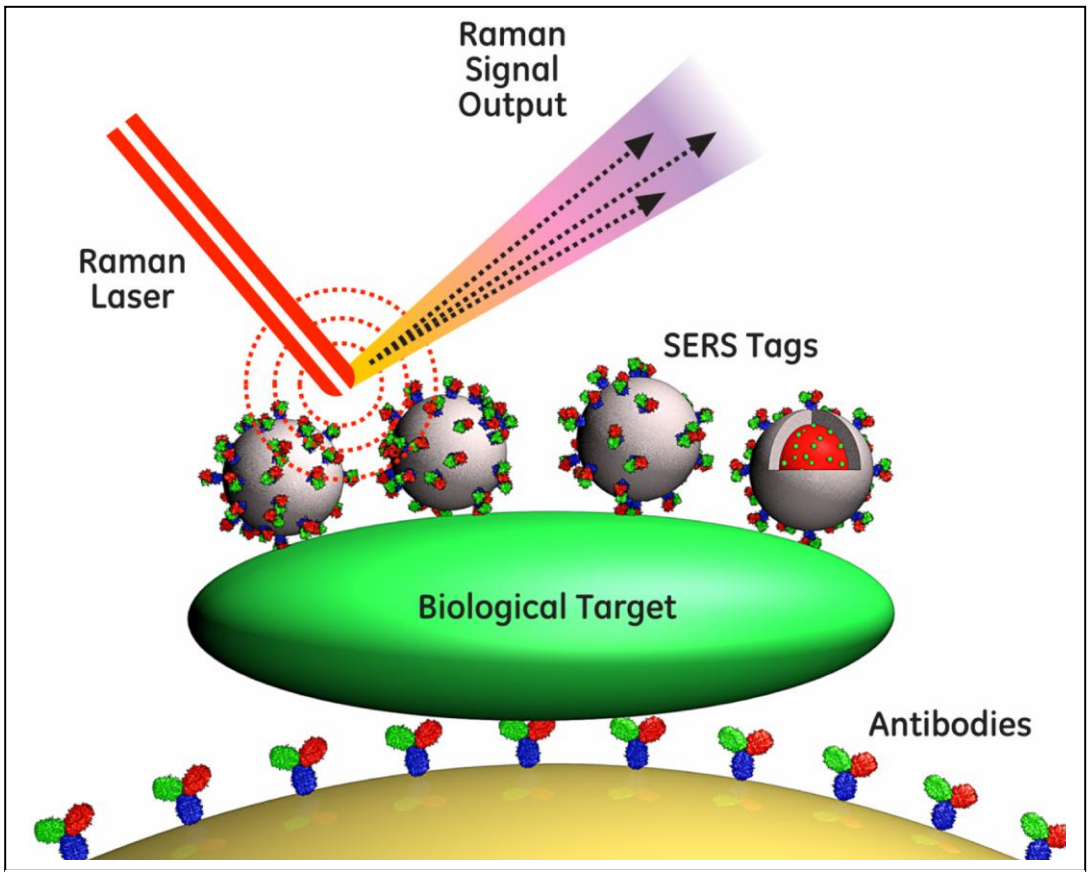

Figure 1-2 Typical setup for SERS biosensors. Antibodies or affinity elements bind the biological target of interest and labeled SERS tags act as enhancers and produce diagnostic spectra.

Taken from http://spie.org/Images/Graphics/Newsroom/Imported-2011/003645/003645_10_fig2.jpg. Accessed 7/14/2011.

SERS Platforms

Since the early 2000s, advances in the production of nanomaterials and progress in understanding their electronic properties has greatly broadened the use of SERS as an analytical tool. It has also broadened the variety of SERS based platforms used to do this analysis. Specialized forms of SERS such as SERRS, TERS, and solution SERS provide alternatives to metallic substrate based methods that may be better suited to specific analytic problems.

SERRS is an important type of SERS that is often used as an analytic technique without being specifically described as such. SERRS occurs when the excitation source matches the absorbance of the analyte bound to the Raman enhancer. SERRS may be used with a variety of enhancers such as solution SERS, roughened substrates, colloidal metals or engineered nanostructures. SERRS lends itself to DNA oligonucleotide based sensing systems[36-42], as fluorophore labeled probes are readily available and often match existing excitation wavelengths. SERRS is particularly sensitive to matching the excitation source with the absorbance wavelengths of the analyte, but it does not have to be a perfect match, as there will still be some absorbance "off-peak". Resonant Raman spectroscopy is even possible if the excitation wavelength does not match at all through Resonance Hyper-Raman Spectroscopy.[43] This setup requires two-photon excitation however and is a relatively "niche" mode of spectroscopy.

Tip-enhanced Raman spectroscopy (TERS)[44] is another unique version of SERS that is particularly useful for surface characterization and probing.[45-48] Figure 1-3 shows a diagram of a typical TERS setup. An atomic force microscopy (AFM) tip is coated

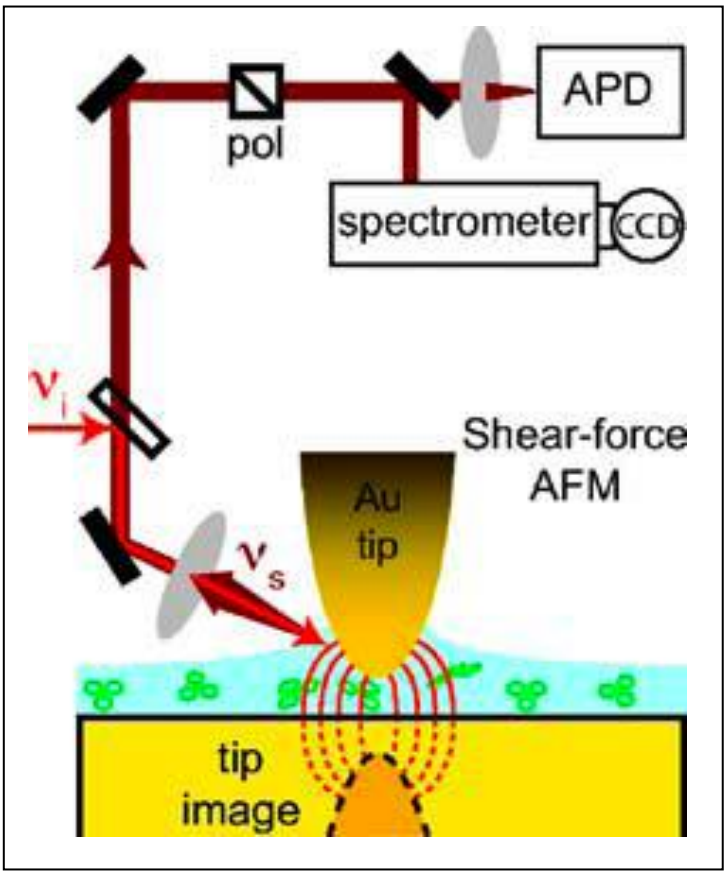

Figure 1-3 Schematic of the experimental arrangement for TERS. The incident light is focused onto the tip–sample gap. The tip enhanced and -scattered Raman response is spectrally filtered using a notch filter and is spectrally resolved by an imaging spectrometer with a liquid nitrogen-cooled charge-coupled device array, or integrally detected by means of an avalanche photodiode (*APD*). Polarization directions of both incident and scattered light beams can be controlled independently. The *blue layer* indicates a thin water film as may be present on the sample under ambient conditions. Reprinted with permission. © Springer Press. 2009.

with gold or a metallic nanoparticle is attached to the tip, then the tip is passed over the surface to be analyzed under laser excitation. This is particularly useful for probing bio-functionalized surfaces[49] or detecting functional groups on a cell or membrane surface.[50, 51] TERS also confers another degree of data because the AFM tip can still be used to gather AF data, providing even more information about the surface. A drawback of TERS is that it is still an emerging field, and does require some special equipment beyond a normal setup. More commercially available "turnkey" setups are emerging on the market, making them accessible to individuals uninterested in building one from scratch.

Particle Types & Properties

After choosing the most appropriate form of SERS and noting the excitation wavelengths available, the next most important decision is the choice of Raman enhancer. This choice, in conjunction with excitation wavelength, dictates the degree of Raman enhancement achievable. It also dictates the routes through which the enhancer can be functionalized and in which environment the metallic enhancer will be stable. While there is an abundance of interesting nanofabricated substrates for SERS[31, 33, 52-54], this review will focus on the discussion of metallic nanoparticles. Particles are often more suited for analysis of biological systems due to their ability to be added to solution, and often have more flexibility than substrate based systems.

Metallic Colloids

While there is no "optimal" Raman enhancer, gold and silver have become the field standards. These metals are popular due their high plasmon induction to surface area

ratio, wide availability, and thiol chemistry compatibility. Other metals such as Al, Li, Cu and Cd are Raman active but have not become popular due to lower overall Raman enhancement and difficulty to work with.[7, 55-57] The choice between silver and gold depends on the assay desired. For a given size of spherical nanoparticle, silver offers higher signal enhancement[58] and provides optimal enhancement when excited in the UV and short wavelength visible light bands. This matches well with assays using DNA functionalized nanoparticles which often utilize fluorophores that absorb in the same range as silver, enabling SERRS enhancement.[58-64] Silver is much more prone to precipitation than gold however, and must be fully passivated prior to exposure to biological samples or samples containing even modest salt concentrations. It should be noted that controlled aggegation of particles can be highly beneficial. Inter-particle enhancement can create "hot-spots" that greatly enhance overall Raman signal.[65-67] Silver is also not nearly as biocompatible as gold. Colloidal silver is highly microbicidal[68-71] and has been shown to cause morphology changes in mammalian cells.[72] In addition to being biocompatible, gold is also a good choice for Raman detection within tissues, as it can be excited in the near-IR range where tissue does not absorb light.[73-75]

Size and shape are the other two contributing factors when choosing a colloidal Raman enhancer. Generally speaking, a larger particle is better when choosing a nanoparticle due to a larger outer surface area for the LSPR to couple through.[76-79] This is limited however, up to a maximum of about 200 nm[78] due to signal dampening from the 'bulk' metal. It is important to note however that the particle must still be matched with excitation wavelength as previously discussed to maintain optimum signal enhancement. Choice of nanoparticle shape is a much more complex issue.[52, 80-82] Spheres are advantageous because they are the best-studied variety, are

easy to synthesize, and are commercially available if desired. They may also be dimerized in a controllable fashion to create Raman active hotspots for increased signal enhancement as seen in Figure 1-4.[83] Figure 1-4a illustrates the hot-spot interaction between two spheres and Figure 1-4b shows how an array of spherical dimers can be incorporated into a silica wafer.

Non-spherical metallic nanoparticles have also been extensively analyzed[82] and have demonstrated SERS enhancing properties for bio-detection[84-86]. Detailed calculations have been done on nanowires featuring irregular cross sections, calculating SERS enhancement up to 10^{12} under ideal conditions, which makes them very desirable SERS enhancers. Non-spherical nanoparticles are particularly interesting for SERS because the LSPR(s) of the particle are not evenly distributed. Edges on the particle are thinner and thus give rise to unique plasmonic fields. By changing the shapes and aspect ratios, it is possible to tune the LSPR(s) of the particles and thus change the enhancer to a detection system's needs. This can be very advantageous when working within biological constraints. Several groups have also been able to magnetize spherical[87] and non-spherical particles[88-90] by creating noble metal-iron oxide hybrids. The magnetization of the particle is a great advantage as the particle can be manipulated across a cell or membrane surface or be used to aggregate particles for high signal localization. The major drawback to non-spherical metallic nanoparticles is a more complex synthesis. Careful control of synthetic parameters is required to obtain monodispersed particles in the shape desired. Methods of synthesis include photoinduction, wet chemical reduction, and lithography and have been well reviewed.[91]

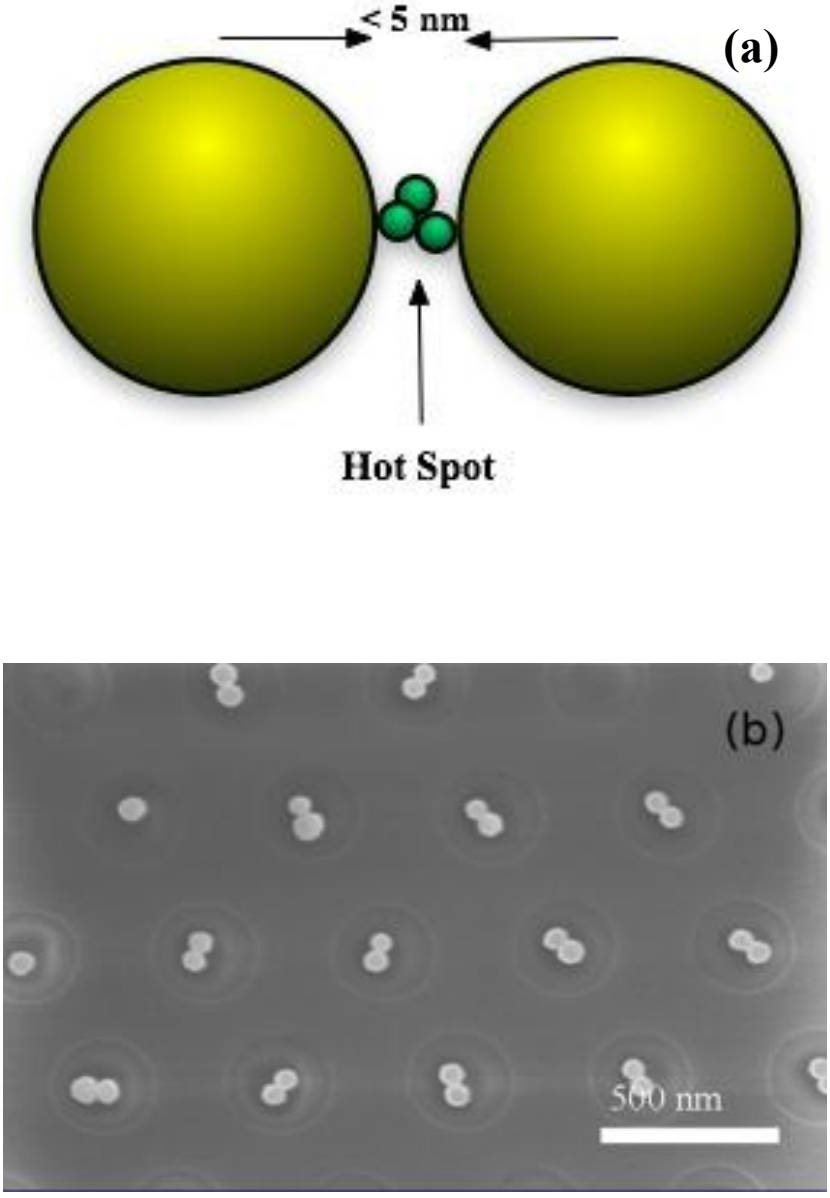

Figure 1-4 a) Diagram of two spherical nanoparticles interacting to create a Raman active hot spot. Note the distance of less than 5 nm required between the particles for the effect to occur. b) Gold dimer array fabricated by a combination of pattern replication, wafer processing techniques, and solvent evaporation. This repeated array creates a homogenous, Raman enhancing substrate for analysis. Reprinted with permission. © John Wiley & Sons Ltd. 2009.

CTAB Functionalized Gold Nanorods

Cetyltrimethylammonium bromide (CTAB) functionalized nanorods are a unique variety of nanoparticle that deserve special mention for SERS bio-detection. They are interesting because their aspect ratio is tunable and they can be selectively functionalized in a number of ways. The nanorods may be tuned by changing the aspect ratio of the particles, which in turn directly affects their transverse and longitudinal LSPR peaks. The location of these plasmons is critical for SERS enhancement, as Raman intensity has been shown to be a direct function of the aspect ratio.[92] These rods are also interesting because they may be preferentially functionalized on their terminal ends rather than on the sides.[93] This phenomenon is due to lack of CTAB on the (111) terminal faces because the (100) side faces allow for proper CTAB head group packing.[94] This allows a variety of bio-molecules such as oligonucleotides or antibodies to be selectively conjugated to the particle while maintaining the CTAB coating. The CTAB coating is a non-polar environment but has been able to detect non-polar small molecules by SERS[95] and has served as a carrier for florescent molecules which can be used as SERS reporters.[96] The CTAB may also be exchanged off completely once the particles are synthesized for subsequent functionalization with affinity groups and SERS interrogation of the bio-analyte of interest.[97-99] Overall, CTAB coated nanorods are a very good choice for Raman enhancer, but do require a moderately difficult synthesis for a monodispersed yield. The hydrophobicity of the CTAB bilayer may also not be compatible with some buffer systems or target molecules.

Functionalization for Molecular Recognition & Stability

While a molecule can be absorbed directly onto a Raman enhancer, most SERS based bio-detection systems will require functionalization of the enhancer with a moiety that has affinity and specificity for the target molecule. The choice of Raman enhancer often dictates how the particle will be functionalized to bind the target bio-molecule. Silver and gold nanoparticles are compatible with thiol chemistry for direct linkage of the capture probe to the particle. The coordination chemistry of the thiol bond to gold nanoparticles has been extensively researched[(100)] revealing a strong and stable bond system. Thiol bonds are often utilized in systems with oligonucleotide capture probes or aptamers, where the DNA is terminally thiolated and directly attached to the particles.[(101-105)] Oligonucleotide aptamers are particularly interesting because they can bind a large variety of molecule types in a manner similar to antibodies, though typically with less affinity.[(106-109)] These systems are well studied, and extensive progress has been made to optimize DNA loading[(110-112)] and particle stability[(113)]. Antibodies or other protein based affinity probes can also be directly conjugated to nanoparticle surfaces through the thiol of cysteine groups. It has been demonstrated that using naturally occurring and engineered cysteines for attachment can greatly alter protein function depending upon cysteine placement, with terminal cysteines causing the least alteration of function.[(114)]

Metallic nanoparticles can also be functionalized with linker groups such as amines, thiols, aldehydes, or alkynes. These groups are typically incorporated by encapsulating an uncapped particle with PEG containing the desired functional group at its solvent exposed terminus. Before using a long chain PEG or undertaking this approach it should be noted that Raman enhancement will be less than direct attachment to the

particle due to a longer distance from the target molecule to the metal enhancer. The most common method for linking proteins and other carboxyl or amine bearing molecules is 1-ethyl-3-(3-dimethylaminopropyl) carbodiimide (EDC)-*N*-Hydroxysuccinimide (NHS) chemistry where the carboxyl group is made amine reactive by preparation with EDC then NHS.[115, 116] This methodology is fairly non-specific however and some loss of function occurs due to functionalization through critical amine or carboxy R groups in the protein. Cysteines in the protein can be used to conjugate to maleimide functionalized PEG but have the same loss of function problem as previously mentioned for direct attachment. "Click chemistry" is also a popular alternative but has some implementation problems. The method requires a reaction between an alkyne and an azide, severely limiting the types of biomolecules that can be attached without further use of "adapter" molecules.[117]

An alternative method to put proteins on particles involves using an engineered intein. An intein is a self-splicing protein element that behaves similarly to exons and introns in RNA. The intein post-translationally splices itself out of the protein in a multistep transesterification-succinimide release process that also splices the two remaining domains of the proteins, known as exteins, together.[118] Several approaches have been used to attach proteins to nanoparticles via inteins. Some have used split inteins[119] while most other groups have used intein mediated protein ligation (IPL) to put proteins on particles. In IPL, a thiol containing compound such as MESNA is used to induce intein cleavage then the protein may be ligated to any thiol reactive group. A modified form of IPL has even been combined with click chemistry to achieve site specific conjugation.[120] Recently, some work has been done with inteins and recombinant engineering to incorporate selenocysteine (Sec) into proteins for attachment and reactivity.[121-123] Selenocysteine is reactive with the same groups as

thiols but is more nucleophilic[124, 125] and forms a more stable bond with gold.[126] Sec is especially interesting due to its low pKa; it is still reactive at lower pH values where cysteine has been protonanted. This means Sec can be used as a site-specific functionalizing agent in a pH dependent manner.

Non-covalent physical interactions may also be used to target bio-molecules for Raman enhancement. This is especially useful when trying to detect a class of molecules similar to each other. In addition to the examples previously discussed, the CTAB bilayer around of coated particles has been used in a variety of ways as a delivery vehicle and could be used in a similar manner to hold a capture group.[127-129] Protein absorption onto nanoparticles through non-covalent interactions, particularly through non-covalent affinity schemes has been extensively reviewed.[130] The strongest non-covalent bond used for labeling is the biotin-streptavadin interaction which has been extensively used to label particles for SERS.[102, 131-133] The drawback to this approach however, is that both the target and the enhancer need to be labeled which is not possible in many sensing schemes. This approach is more appropriate for easy labeling of reporter dyes to the nanoparticle if the target itself does not provide enough Raman signal.

Bio-Sensing Applications

It is beyond the scope of this review to analyze all the applications of SERS biosensors, but a few interesting uses stand out. SERS biosensors often use DNA as a capture probe for their target. While many have detected small molecules or specific sequences, only a few have interrogated small nucleotide polymophisms (SNPs).[64, 134-136] SNPs are an important research topic because these single mutations are the most common variations across a genome and can be used to directly detect alleles

responsible for a trait of interest.[137, 138] Lowe et. al, for example, was able to show multiplex detection of three cancer haplotypes and correlate Raman intensity to DNA copy number.[135] In addition to DNA targets, small molecules also make up a large portion of SERS based bio-sensor targets. While many DNA and protein capture probes are often used, synthetic oligosaccharides have also been used to specifically capture pesticides.[139] At the cellular level, SERS has been able to identify microbial species, manipulate microbial cells via optical Raman tweezer, and determine their spatial distribution *in vivo*.[140] Researchers have also been able to use SERS for "imaging" of tumors and other mammalian cell system, differentiating cells types based on their Raman spectra.[141, 142] SERS biosensors have also been actively used in environmental studies. This has been described in an excellent review, citing examples of detection of pollutants in air, water and soil as well as analysis of living tissue from the environment.[143] While almost all the studies previously mentioned have used SERS detectors as close to the sample as possible, stand-off SERS is also possible.[144] In this setup, the target can be meters away from the detector and excitation source, but the enhancing element must still be adjacent to the particle. This is particularly useful for detection of harmful chemical reagents or explosive components.

Concluding Thoughts

This dissertation research directly addresses several important questions in the field of SERS biosensors. The second chapter examines whether it is possible to detect SNPs using SERS and if so, if it could be done in a multiplex fashion. Building upon that work, the third chapter examines CTAB coated nanoparticles, which have been used as SERS enhancers. It specifically addresses how non-polar dyes traffick through the

CTAB bilayer and how the molecules' affinity affects FRET. Quenching of fluorescence is critically important to obtain a clear Raman spectrum. Finally, the fourth chapter addresses nanoparticle functionalization for use in SERS and other bio-nanotechnology platforms. The system developed demonstrates an amino acid specific, pH selective method for conjugating proteins to nanoparticles. This increases efficiency as compared to non-specific methods such as EDC-NHS chemistry, which can interrupt critical, structural amino acids on the proteins' surface.

REFERENCES

(1) Raman, C. V., and Krishnan, K. S. (1928) A new type of secondary radiation. *Nature 121*, 501-502.

(2) Fleischmann, M., Hendra, P. J., and McQuillan, A. J. (1974) Raman spectra of pyridine adsorbed at a silver electrode. *Chemical Physics Letters 26*, 163-166.

(3) Ding, S. Y., Wu, D. Y., Yang, Z. L., Ren, B., Xu, X., and Tian, Z. Q. (2008) Some Progresses in Mechanistic Studies on Surface-Enhanced Raman Scattering. *Chemical Journal of Chinese Universities-Chinese 29*, 2569-2581.

(4) Lombardi, J. R., and Birke, R. L. (2009) A Unified View of Surface-Enhanced Raman Scattering. *Accounts of Chemical Research 42*, 734-742.

(5) Schatz, G. C., Young, M. A., and Van Duyne, R. P. (2006) Electromagnetic mechanism of SERS. *Surface-Enhanced Raman Scattering: Physics and Applications 103*, 19-45.

(6) Tong, L. M., Zhu, T., and Liu, Z. F. Approaching the electromagnetic mechanism of surface-enhanced Raman scattering: from self-assembled arrays to individual gold nanoparticles. *Chemical Society Reviews 40*, 1296-1304.

(7) Wu, D. Y., Liu, X. M., Duan, S., Xu, X., Ren, B., Lin, S. H., and Tian, Z. Q. (2008) Chemical enhancement effects in SERS spectra: A quantum chemical study of pyridine interacting with copper, silver, gold and platinum metals. *Journal of Physical Chemistry C 112*, 4195-4204.

(8) Mock, J. J., Barbic, M., Smith, D. R., Schultz, D. A., and Schultz, S. (2002) Shape effects in plasmon resonance of individual colloidal silver nanoparticles. *Journal of Chemical Physics 116*, 6755-6759.

(9) Nelayah, J., Kociak, M., Stephan, O., de Abajo, F. J. G., Tence, M., Henrard, L., Taverna, D., Pastoriza-Santos, I., Liz-Marzan, L. M., and Colliex, C. (2007) Mapping surface plasmons on a single metallic nanoparticle. *Nature Physics 3*, 348-353.

(10) Smith, D. A., and Stokes, K. L. (2006) Discrete dipole approximation for magneto-optical scattering calculations. *Optics Express 14*.

(11) Brust, M., and Kiely, C. J. (2002) Some recent advances in nanostructure preparation from gold and silver particles: a short topical review. *Colloids and Surfaces a-Physicochemical and Engineering Aspects 202*, 175-186.

(12) Daniel, M. C., and Astruc, D. (2004) Gold nanoparticles: Assembly, supramolecular chemistry, quantum-size-related properties, and applications toward biology, catalysis, and nanotechnology. *Chemical Reviews 104*, 293-346.

(13) Campion, A., and Kambhampati, P. (1998) Surface-enhanced Raman scattering. *Chemical Society Reviews 27*, 241-250.

(14) Otto, A. (1991) SURFACE-ENHANCED RAMAN-SCATTERING OF ADSORBATES. *J Raman Spectrosc 22*, 743-752.

(15) Otto, A., and Futamata, M. (2006) Electronic mechanisms of SERS. *Surface-Enhanced Raman Scattering: Physics and Applications 103*, 147-182.

(16) Morton, S. M., and Jensen, L. (2009) Understanding the Molecule,àíSurface Chemical Coupling in SERS. *Journal of the American Chemical Society 131*, 4090-4098.

(17) Lombardi, J. R. (1986) THE YUKAWA POTENTIAL IN MOMENTUM

SPACE - ANALYTIC BEHAVIOR OF THE EIGENFUNCTIONS. *Journal of Chemical Physics 85*, 949-952.

(18) Stiles, P. L., Dieringer, J. A., Shah, N. C., and Van Duyne, R. R. (2008) Surface-Enhanced Raman Spectroscopy. *Annual Review of Analytical Chemistry 1*, 601-626.

(19) Kennedy, B. J., Spaeth, S., Dickey, M., and Carron, K. T. (1999) Determination of the distance dependence and experimental effects for modified SERS substrates based on self-assembled monolayers formed using alkanethiols. *Journal of Physical Chemistry B 103*, 3640-3646.

(20) Kovacs, G. J., Loutfy, R. O., Vincett, P. S., Jennings, C., and Aroca, R. (1986) DISTANCE DEPENDENCE OF SERS ENHANCEMENT FACTOR FROM LANGMUIR-BLODGETT MONOLAYERS ON METAL ISLAND FILMS - EVIDENCE FOR THE ELECTROMAGNETIC MECHANISM. *Langmuir 2*, 689-694.

(21) Algar, W. R., Massey, M., and Krull, U. J. (2009) The application of quantum dots, gold nanoparticles and molecular switches to optical nucleic-acid diagnostics. *Trac-Trends in Analytical Chemistry 28*, 292-306.

(22) Barazzouk, S., Kamat, P. V., and Hotchandani, S. (2005) Photoinduced electron transfer between chlorophyll a and gold nanoparticles. *Journal of Physical Chemistry B 109*, 716-723.

(23) Ganbold, E. O., Park, J. H., Ock, K. S., and Joo, S. W. Gold Nanoparticle-Based Detection of Hg(II) in an Aqueous Solution: Fluorescence Quenching and Surface-Enhanced Raman Scattering Study. *Bulletin of the Korean*

Chemical Society 32, 519-523.

(24) Kato, N., and Caruso, F. (2005) Homogeneous, competitive fluorescence quenching immunoassay based on gold nanoparticle/polyelectrolyte coated latex particles. *Journal of Physical Chemistry B 109*, 19604-19612.

(25) Kerker, M. (1985) THE OPTICS OF COLLOIDAL SILVER - SOMETHING OLD AND SOMETHING NEW. *Journal of Colloid and Interface Science 105*, 297-314.

(26) Lim, S. Y., Kim, J. H., Lee, J. S., and Park, C. B. (2009) Gold Nanoparticle Enlargement Coupled with Fluorescence Quenching for Highly Sensitive Detection of Analytes. *Langmuir 25*, 13302-13305.

(27) Aslan, K., and Geddes, C. D. (2008) A review of an ultrafast and sensitive bioassay platform technology: Microwave-accelerated metal-enhanced fluorescence. *Plasmonics 3*, 89-101.

(28) Aslan, K., Gryczynski, I., Malicka, J., Matveeva, E., Lakowicz, J. R., and Geddes, C. D. (2005) Metal-enhanced fluorescence: an emerging tool in biotechnology. *Current Opinion in Biotechnology 16*, 55-62.

(29) Aslan, K., Lakowicz, J. R., and Geddes, C. D. (2005) Metal-enhanced fluorescence using anisotropic silver nanostructures: critical progress to date. *Analytical and Bioanalytical Chemistry 382*, 926-933.

(30) Lakowicz, J. R. (2005) Radiative decay engineering 5: metal-enhanced fluorescence and plasmon emission. *Analytical Biochemistry 337*, 171-194.

(31) Camden, J. P., Dieringer, J. A., Zhao, J., and Van Duyne, R. P. (2008) Controlled Plasmonic Nanostructures for Surface-Enhanced Spectroscopy and

Sensing. *Accounts of Chemical Research 41*, 1653-1661.

(32) McFarland, A. D., Young, M. A., Dieringer, J. A., and Van Duyne, R. P. (2005) Wavelength-scanned surface-enhanced Raman excitation spectroscopy. *Journal of Physical Chemistry B 109*, 11279-11285.

(33) Liu, S. Q., and Tang, Z. Y. Nanoparticle assemblies for biological and chemical sensing. *Journal of Materials Chemistry 20*, 24-35.

(34) Smith, W. E. (1993) SURFACE-ENHANCED RESONANCE RAMAN-SCATTERING, in *Metallobiochemistry, Part C* pp 482-495, Academic Press Inc, San Diego.

(35) Smith, W. E. (2008) Practical understanding and use of surface enhanced Raman scattering/surface enhanced resonance Raman scattering in chemical and biological analysis. *Chemical Society Reviews 37*, 955-964.

(36) Cederquist, K. B., Golightly, R. S., and Keating, C. D. (2008) Molecular beacon-metal nanowire interface: Effect of probe sequence and surface coverage on sensor performance. *Langmuir 24*, 9162-9171.

(37) Faulds, K., Jarvis, R., Smith, W. E., Graham, D., and Goodacre, R. (2008) Multiplexed detection of six labelled oligonucleotides using surface enhanced resonance Raman scattering (SERRS). *Analyst 133*, 1505-1512.

(38) Faulds, K., MacAskill, A., MacRae, D., Dougan, J., and Graham, D. DNA Sequence Detection Using Surface Enhanced Resonance Raman Spectroscopy (SERRS) in a Homogeneous Multiplexed Assay. *Xxii International Conference on Raman Spectroscopy 1267*, 82-83.

(39) Hering, K. K., Moller, R., Fritzsche, W., and Popp, J. (2008) Microarray-based

detection of dye-labeled DNA by SERRS using particles formed by enzymatic silver deposition. *Chemphyschem 9*, 867-872.

(40) Strelau, K. K., Kretschmer, R., Moller, R., Fritzsche, W., and Popp, J. SERS as tool for the analysis of DNA-chips in a microfluidic platform. *Analytical and Bioanalytical Chemistry 396*, 1381-1384.

(41) Thompson, D. G., Faulds, K., Smith, W. E., and Graham, D. Precise Control of the Assembly of Dye-Coded Oligonucleotide Silver Nanoparticle Conjugates with Single Base Mismatch Discrimination Using Surface Enhanced Resonance Raman Scattering. *Journal of Physical Chemistry C 114*, 7384-7389.

(42) Yichun, L., Mingya, Z., Guiye, S., Yajun, L., Baiqu, H., and Guoliang, Y. (2008) Biocompatible ZnO/Au nanocomposites for ultrasensitive DNA detection using resonance Raman scattering. *Journal of Physical Chemistry B*, 6484-9.

(43) Kelley, A. M. (2008) Resonance Raman and Resonance Hyper-Raman Intensities: Structure and Dynamics of Molecular Excited States in Solution. *J. Phys. Chem. A 112*, 11975-11991.

(44) Pettinger, B. Single-molecule surface- and tip-enhanced raman spectroscopy. *Molecular Physics: An International Journal at the Interface Between Chemistry and Physics 108*, 2039 - 2059.

(45) C, B., U, N., J, P., and V, D. (2008) Cell wall investigations utilizing tip-enhanced Raman scattering. *Journal of Microscopy 229*, 533-539.

(46) Cialla, D., Deckert-Gaudig, T., Budich, C., Laue, M., Moller, R., Naumann,

D., Deckert, V., and Popp, J. (2009) Raman to the limit: tip-enhanced Raman spectroscopic investigations of a single tobacco mosaic virus. *J Raman Spectrosc 40*, 240-243.

(47) Neacsu, C., Berweger, S., and Raschke, M. (2007) Tip-Enhanced Raman Imaging and Nanospectroscopy: Sensitivity, Symmetry, and Selection Rules. *NanoBioTechnology 3*, 172-196.

(48) Neugebauer, U., Rosch, P., Schmitt, M., Popp, J., Julien, C., Rasmussen, A., Budich, C., and Deckert, V. (2006) On the way to nanometer-sized information of the bacterial surface by tip-enhanced Raman spectroscopy. *Chemphyschem 7*, 1428-1430.

(49) Domke, K. F., Zhang, D., and Pettinger, B. (2007) Tip-Enhanced Raman Spectra of Picomole Quantities of DNA Nucleobases at Au(111). *Journal of the American Chemical Society 129*, 6708-6709.

(50) Budich, C., Neugebauer, U., Popp, J., and Deckert, V. (2008) Cell wall investigations utilizing tip-enhanced Raman scattering. *Journal of Microscopy 229*, 533-539.

(51) Neugebauer, U., Schmid, U., Baumann, K., Ziebuhr, W., Kozitskaya, S., Deckert, V., Schmitt, M., and Popp, J. (2007) Towards a Detailed Understanding of Bacterial Metabolism—Spectroscopic Characterization of Staphylococcus Epidermidis. *Chemphyschem 8*, 124-137.

(52) Lin, X. M., Cui, Y., Xu, Y. H., Ren, B., and Tian, Z. Q. (2009) Surface-enhanced Raman spectroscopy: substrate-related issues. *Analytical and Bioanalytical Chemistry 394*, 1729-1745.

(53) Masson, J. F., Murray-Methot, M. P., and Live, L. S. Nanohole arrays in chemical analysis: manufacturing methods and applications. *Analyst 135*, 1483-1489.

(54) Tripp, R. A., Dluhy, R. A., and Zhao, Y. P. (2008) Novel nanostructures for SERS biosensing. *Nano Today 3*, 31-37.

(55) Ren, B., Liu, G. K., Lian, X. B., Yang, Z. L., and Tian, Z. Q. (2007) Raman spectroscopy on transition metals. *Analytical and Bioanalytical Chemistry 388*, 29-45.

(56) Tian, Z. Q., Ren, B., and Wu, D. Y. (2002) Surface-enhanced Raman scattering: From noble to transition metals and from rough surfaces to ordered nanostructures. *Journal of Physical Chemistry B 106*, 9463-9483.

(57) Zeman, E. J., and Schatz, G. C. (1987) An Accurate Electromagnetic Theory Study of Surface Enhancement Factors for Ag, Au, Cu, Li, Na, Al, Ga, in, Zn, and Cd. *Journal of Physical Chemistry 91*, 634-643.

(58) Stokes, R. J., Macaskill, A., Lundahl, P. J., Smith, W. E., Faulds, K., and Graham, D. (2007) Quantitative enhanced Raman scattering of labeled DNA from gold and silver nanoparticles. *Small 3*, 1593-601.

(59) Faulds, K., Jarvis, R., Smith, W. E., Graham, D., and Goodacre, R. (2008) Multiplexed detection of six labelled oligonucleotides using surface enhanced resonance Raman scattering (SERRS). *Analyst 133*, 1505-12.

(60) Faulds, K., McKenzie, F., Smith, W. E., and Graham, D. (2007) Quantitative simultaneous multianalyte detection of DNA by dual-wavelength surface-enhanced resonance Raman scattering. *Angew Chem Int Ed Engl 46*, 1829-31.

(61) Faulds, K., Smith, W. E., and Graham, D. (2004) Evaluation of surface-enhanced resonance Raman scattering for quantitative DNA analysis. *Anal Chem 76*, 412-7.

(62) Fruk, L., Grondin, A., Smith, W. E., and Graham, D. (2002) A new approach to oligonucleotide labelling using Diels-Alder cycloadditions and detection by SERRS. *Chemical Communications*, 2100-2101.

(63) Graham, D., and Faulds, K. (2008) Quantitative SERRS for DNA sequence analysis. *Chem Soc Rev 37*, 1042-51.

(64) Graham, D., Mallinder, B. J., Whitcombe, D., Watson, N. D., and Smith, W. E. (2002) Simple multiplex genotyping by surface-enhanced resonance Raman scattering. *Anal Chem 74*, 1069-74.

(65) Graham, D., Stevenson, R., Thompson, D. G., Barrett, L., Dalton, C., and Faulds, K. Combining functionalised nanoparticles and SERS for the detection of DNA relating to disease. *Faraday Discussions 149*, 291-299.

(66) Larmour, I. A., Faulds, K., and Graham, D. Improved Versatility of Silver Nanoparticle Dimers for Surface-Enhanced Raman Spectroscopy. *Journal of Physical Chemistry C 114*, 13249-13254.

(67) Braun, G. B., Lee, S. J., Laurence, T., Fera, N., Fabris, L., Bazan, G. C., Moskovits, M., and Reich, N. O. (2009) Generalized Approach to SERS-Active Nanomaterials via Controlled Nanoparticle Linking, Polymer Encapsulation, and Small-Molecule Infusion. *Journal of Physical Chemistry C 113*, 13622-13629.

(68) Morones, J. R., Elechiguerra, J. L., Camacho, A., Holt, K., Kouri, J. B.,

Ramirez, J. T., and Yacaman, M. J. (2005) The bactericidal effect of silver nanoparticles. *Nanotechnology 16*, 2346-2353.

(69) Lok, C.-N., Ho, C.-M., Chen, R., He, Q.-Y., Yu, W.-Y., Sun, H., Tam, P. K.-H., Chiu, J.-F., and Che, C.-M. (2006) Proteomic Analysis of the Mode of Antibacterial Action of Silver Nanoparticles. *Journal of Proteome Research 5*, 916-924.

(70) Jung, W. K., Koo, H. C., Kim, K. W., Shin, S., Kim, S. H., and Park, Y. H. (2008) Antibacterial Activity and Mechanism of Action of the Silver Ion in Staphylococcus aureus and Escherichia coli. *Appl. Environ. Microbiol. 74*, 2171-2178.

(71) Fabrega, J., Renshaw, J. C., and Lead, J. R. (2009) Interactions of Silver Nanoparticles with Pseudomonas putida Biofilms. *Environmental Science & Technology 43*, 9004-9009.

(72) Bhabra, G., Sood, A., Fisher, B., Cartwright, L., Saunders, M., Evans, W. H., Surprenant, A., Lopez-Castejon, G., Mann, S., Davis, S. A., Hails, L. A., Ingham, E., Verkade, P., Lane, J., Heesom, K., Newson, R., and Case, C. P. (2009) Nanoparticles can cause DNA damage across a cellular barrier. *Nat Nano advance online publication*.

(73) Moody, B., Haslauer, C. M., Kirk, E., Kannan, A., Loboa, E. G., and McCarty, G. S. In Situ Monitoring of Adipogenesis with Human-Adipose-Derived Stem Cells Using Surface-Enhanced Raman Spectroscopy. *Appl Spectrosc 64*, 1227-1233.

(74) Qian, J., Jiang, L., Cai, F. H., Wang, D., and He, S. L. Fluorescence-surface

enhanced Raman scattering co-functionalized gold nanorods as near-infrared probes for purely optical in vivo imaging. *Biomaterials 32*, 1601-1610.

(75) Schutz, M., Steinigeweg, D., Salehi, M., Kompe, K., and Schlucker, S. Hydrophilically stabilized gold nanostars as SERS labels for tissue imaging of the tumor suppressor p63 by immuno-SERS microscopy. *Chemical Communications 47*, 4216-4218.

(76) Hui-Wen, C., Yiming, L., and Jung-Yen, Y. Effects of Shape and Size on Field Enhancement of Au Nanoparticles on SERS-active Substrates. *Proceedings 2010 10th IEEE International Conference on Nanotechnology and Joint Symposium with Nano Korea 2010 KINTEX (IEEE-NANO 2010)*, 732-5.

(77) Kwan, K., Dongha, S., Kyung Lock, K., and Kuan Soo, S. Electromagnetic field enhancement in the gap between two Au nanoparticles: the size of hot site probed by surface-enhanced Raman scattering. *Physical Chemistry Chemical Physics*, 3747-52.

(78) Li, L.-m., Fang, P.-p., Yang, Z.-l., Huang, W.-d., Wu, D.-y., Ren, B., and Tian, Z.-q. (2009) Size dependent SERS activity of gold nanoparticles studied by 3D-FDTD simulation. *Spectroscopy and Spectral Analysis*, 1222-6.

(79) Seney, C. S., Gutzman, B. M., and Goddard, R. H. (2009) Correlation of Size and Surface-Enhanced Raman Scattering Activity of Optical and Spectroscopic Properties for Silver Nanoparticles. *Journal of Physical Chemistry C 113*, 74-80.

(80) Abalde-Cela, S., Aldeanueva-Potel, P., Mateo-Mateo, C., Rodriguez-Lorenzo, L., Alvarez-Puebla, R. A., and Liz-Marzan, L. M. Surface-enhanced Raman

scattering biomedical applications of plasmonic colloidal particles. *Journal of the Royal Society Interface 7*, S435-S450.

(81) Pastoriza-Santos, I., Alvarez-Puebla, R. A., and Liz-Marzan, L. M. Synthetic Routes and Plasmonic Properties of Noble Metal Nanoplates. *European Journal of Inorganic Chemistry*, 4288-4297.

(82) Sau, T. K., Rogach, A. L., Jackel, F., Klar, T. A., and Feldmann, J. Properties and Applications of Colloidal Nonspherical Noble Metal Nanoparticles. *Adv Mater 22*, 1805-1825.

(83) Alexander, K. D., Hampton, M. J., Zhang, S., Dhawan, A., Xu, H., and Lopez, R. (2009) A high-throughput method for controlled hot-spot fabrication in SERS-active gold nanoparticle dimer arrays. *J Raman Spectrosc 40*, 2171-2175.

(84) Barbosa, S., Agrawal, A., Rodriguez-Lorenzo, L., Pastoriza-Santos, I., Alvarez-Puebla, R. A., Kornowski, A., Weller, H., and Liz-Marzan, L. M. Tuning Size and Sensing Properties in Colloidal Gold Nanostars. *Langmuir 26*, 14943-14950.

(85) Camargo, P. H. C., Cobley, C. M., Rycenga, M., and Xia, Y. (2009) Measuring the surface-enhanced Raman scattering enhancement factors of hot spots formed between an individual Ag nanowire and a single Ag nanocube. *Nanotechnology 20*, 434020.

(86) Xie, J. P., Zhang, Q. B., Lee, J. Y., and Wang, D. I. C. (2008) The Synthesis of SERS-Active Gold Nanoflower Tags for In Vivo Applications. *ACS Nano 2*, 2473-2480.

(87) Han, B., Choi, N., Kim, K. H., Lim, D. W., and Choo, J. Application of Silver-Coated Magnetic Microspheres to a SERS-Based Optofluidic Sensor. *Journal of Physical Chemistry C 115*, 6290-6296.

(88) Kim, K., Choi, J. Y., Lee, H. B., and Shin, K. S. Silanization of Ag-Deposited Magnetite Particles: An Efficient Route to Fabricate Magnetic Nanoparticle-Based Raman Barcode Materials. *Acs Applied Materials & Interfaces 2*, 1872-1878.

(89) Liu, G. L., Lu, Y., Kim, J., Doll, J. C., and Lee, L. P. (2005) Magnetic nanocrescents as controllable surface-enhanced Raman scattering nanoprobes for biomolecular imaging. *Adv Mater 17*, 2683-+.

(90) Zhang, L., Dong, W. F., Tang, Z. Y., Song, J. F., Xia, H., and Sun, H. B. Surface-enhanced Raman scattering substrates of high-density and high-homogeneity hot spots by magneto-metal nanoprobe assembling. *Optics Letters 35*, 3297-3299.

(91) Pastoriza-Santos, I., Alvarez-Puebla, R. A., and Liz-Marzán, L. M. Synthetic Routes and Plasmonic Properties of Noble Metal Nanoplates. *European Journal of Inorganic Chemistry 2010*, 4288-4297.

(92) Orendorff, C. J., Gearheart, L., Jana, N. R., and Murphy, C. J. (2006) Aspect ratio dependence on surface enhanced Raman scattering using silver and gold nanorod substrates. *Physical Chemistry Chemical Physics 8*, 165-170.

(93) Caswell, K. K., Wilson, J. N., Bunz, U. H., and Murphy, C. J. (2003) Preferential end-to-end assembly of gold nanorods by biotin-streptavidin connectors. *J Am Chem Soc 125*, 13914-5.

(94) Johnson, C. J., Dujardin, E., Davis, S. A., Murphy, C. J., and Mann, S. (2002) Growth and form of gold nanorods prepared by seed-mediated, surfactant-directed synthesis. *Journal of Materials Chemistry 12*, 1765-1770.

(95) Alkilany, A. M., Frey, R. L., Ferry, J. L., and Murphy, C. J. (2008) Gold nanorods as nanoadmicelles: 1-naphthol partitioning into a nanorod-bound surfactant bilayer. *Langmuir 24*, 10235-9.

(96) Alper, J., Crespo, M., and Hamad-Schifferli, K. (2009) Release Mechanism of Octadecyl Rhodamine B Chloride from Au Nanorods by Ultrafast Laser Pulses. *The Journal of Physical Chemistry C 113*, 5967-5973.

(97) Strickland, A. D., and Batt, C. A. (2009) Detection of carbendazim by surface-enhanced Raman scattering using cyclodextrin inclusion complexes on gold nanorods. *Anal Chem 81*, 2895-903.

(98) Wijaya, A., and Hamad-Schifferli, K. (2008) Ligand customization and DNA functionalization of gold nanorods via round-trip phase transfer ligand exchange. *Langmuir 24*, 9966-9969.

(99) Wijaya, A., Schaffer, S. B., Pallares, I. G., and Hamad-Schifferli, K. (2008) Selective Release of Multiple DNA Oligonucleotides from Gold Nanorods. *ACS Nano 3*, 80-86.

(100) Toma, H. E., Zamarion, V. M., Toma, S. H., and Araki, K. The coordination chemistry at gold nanoparticles. *Journal of the Brazilian Chemical Society 21*, 1158-1176.

(101) Darbha, G. K., Rai, U. S., Singh, A. K., and Ray, P. C. (2008) Gold-nanorod-based sensing of sequence specific HIV-1 virus DNA by using hyper-Rayleigh

scattering spectroscopy. *Chem-Eur J 14*, 3896-3903.

(102) Kim, N. H., Lee, S. J., and Moskovits, M. Aptamer-Mediated Surface-Enhanced Raman Spectroscopy Intensity Amplification. *Nano Letters 10*, 4181-4185.

(103) Pagba, C. V., Lane, S. M., Cho, H. S., and Wachsmann-Hogiu, S. Direct detection of aptamer-thrombin binding via surface-enhanced Raman spectroscopy. *Journal of Biomedical Optics 15*.

(104) Pagba, C. V., Lane, S. M., and Wachsmann-Hogiu, S. Raman and surface-enhanced Raman spectroscopic studies of the 15-mer DNA thrombin-binding aptamer. *J Raman Spectrosc 41*, 241-247.

(105) Wang, G. Q., Chen, Z. P., and Chen, L. X. Aptamer-Nanoparticle-Based Optical Probes. *Progress in Chemistry 22*, 489-499.

(106) Cerchia, L., Giangrande, P. H., McNamara, J. O., and de Franciscis, V. (2009) Cell-specific aptamers for targeted therapies. *Methods Mol Biol 535*, 59-78.

(107) Famulok, M. (1999) Oligonucleotide aptamers that recognize small molecules. *Curr Opin Struct Biol 9*, 324-9.

(108) Li, D., Song, S., and Fan, C. Target-responsive structural switching for nucleic acid-based sensors. *Acc Chem Res 43*, 631-41.

(109) Yan, A. C., and Levy, M. (2009) Aptamers and aptamer targeted delivery. *RNA Biol 6*, 316-20.

(110) Barhoumi, A., Zhang, D., and Halas, N. J. (2008) Correlation of Molecular Orientation and Packing Density in a dsDNA Self-Assembled Monolayer Observable with Surface-Enhanced Raman Spectroscopy. *Journal of the*

American Chemical Society 130, 14040-14041.

(111) Hurst, S. J., Lytton-Jean, A. K. R., and Mirkin, C. A. (2006) Maximizing DNA Loading on a Range of Gold Nanoparticle Sizes. *Analytical Chemistry 78*, 8313-8318.

(112) Taton, T. A. (2002) Preparation of gold nanoparticle-DNA conjugates. *Curr Protoc Nucleic Acid Chem Chapter 12*, Unit 12 2.

(113) Dougan, J. A., Karlsson, C., Smith, W. E., and Graham, D. (2007) Enhanced oligonucleotide‚Äìnanoparticle conjugate stability using thioctic acid modified oligonucleotides. *Nucleic Acids Research 35*, 3668-3675.

(114) Aubin-Tam, M.-E., Hwang, W., and Hamad-Schifferli, K. (2009) Site-directed nanoparticle labeling of cytochrome c. *Proceedings of the National Academy of Sciences*.

(115) Aubin-Tam, M. E., and Hamad-Schifferli, K. (2008) Structure and function of nanoparticle‚Äìprotein conjugates. *Biomedical Materials 3*, 034001.

(116) Drechsler, U., Fischer, N. O., Frankamp, B. L., and Rotello, V. M. (2004) Highly Efficient Biocatalysts via Covalent Immobilization of Candida rugosa Lipase on Ethylene Glycol-Modified Gold–Silica Nanocomposites. *Adv Mater 16*, 271-274.

(117) Lutz, J.-F., and Zarafshani, Z. (2008) Efficient construction of therapeutics, bioconjugates, biomaterials and bioactive surfaces using azide-alkyne "click" chemistry. *Advanced Drug Delivery Reviews 60*, 958-970.

(118) Klabunde, T., Sharma, S., Telenti, A., Jacobs, W. R., Jr., and Sacchettini, J. C. (1998) Crystal structure of GyrA intein from Mycobacterium xenopi reveals

structural basis of protein splicing. *Nat Struct Biol 5*, 31-6.

(119) Charalambous, A., Andreou, M., and Skourides, P. (2009) Intein-mediated site-specific conjugation of Quantum Dots to proteins in vivo. *Journal of Nanobiotechnology 7*, 9.

(120) Elias, D. R., Cheng, Z. L., and Tsourkas, A. An Intein-Mediated Site-Specific Click Conjugation Strategy for Improved Tumor Targeting of Nanoparticle Systems. *Small 6*, 2460-2468.

(121) Arner, E. S., Sarioglu, H., Lottspeich, F., Holmgren, A., and Bock, A. (1999) High-level expression in Escherichia coli of selenocysteine-containing rat thioredoxin reductase utilizing gene fusions with engineered bacterial-type SECIS elements and co-expression with the selA, selB and selC genes. *J Mol Biol 292*, 1003-16.

(122) Hondal, R. J., Nilsson, B. L., and Raines, R. T. (2001) Selenocysteine in native chemical ligation and expressed protein ligation. *J Am Chem Soc 123*, 5140-1.

(123) Jiang, Z., ArnÈr, E. S. J., Mu, Y., Johansson, L., Shi, J., Zhao, S., Liu, S., Wang, R., Zhang, T., Yan, G., Liu, J., Shen, J., and Luo, G. (2004) Expression of selenocysteine-containing glutathione S-transferase in Escherichia coli. *Biochemical and Biophysical Research Communications 321*, 94-101.

(124) Huber, R. E., and Criddle, R. S. (1967) Comparison of the chemical properties of selenocysteine and selenocystine with their sulfur analogs. *Arch Biochem Biophys 122*, 164-73.

(125) Nygard, B. (1967) Polarographic investigations of organic selenium compounds. III. Polarography of selenocystine-selenocysteine. *Ark. Kemi 27*,

341.

(126) Cortie, M. B., and McDonagh, A. (2009) *Nanoscience of Gold and Gold Surfaces*, Wiley-VCH Verlag GmbH & Co. KGaA.

(127) Fay, F., Quinn, D. J., Gilmore, B. F., McCarron, P. A., and Scott, C. J. Gene delivery using dimethyldidodecylammonium bromide-coated PLGA nanoparticles. *Biomaterials 31*.

(128) Siddiqui, A., Patwardhan, G. A., Liu, Y. Y., and Nazzal, S. Mixed backbone antisense glucosylceramide synthase oligonucleotide (MBO-asGCS) loaded solid lipid nanoparticles: In vitro characterization and reversal of multidrug resistance in NCI/ADR-RES cells. *International Journal of Pharmaceutics 400*, 251-259.

(129) Zhang, Y., Jiang, T., Zhang, Q., and Wang, S. Inclusion of telmisartan in mesocellular foam nanoparticles: Drug loading and release property. *European Journal of Pharmaceutics and Biopharmaceutics 76*, 17-23.

(130) Rana, S., Yeh, Y. C., and Rotello, V. M. Engineering the nanoparticle-protein interface: applications and possibilities. *Curr Opin Chem Biol 14*, 828-34.

(131) Guven, B., Basaran-Akgul, N., Temur, E., Tamer, U., and Boyaci, I. H. SERS-based sandwich immunoassay using antibody coated magnetic nanoparticles for Escherichia coli enumeration. *Analyst 136*, 740-748.

(132) Han, X. X., Kitahama, Y., Tanaka, Y., Guo, J., Xu, W. Q., Zhao, B., and Ozaki, Y. (2008) Simplified protocol for detection of protein-ligand interactions via surface-enhanced resonance Raman scattering and surface-enhanced fluorescence. *Analytical Chemistry 80*, 6567-6572.

(133) Jun, B. H., Noh, M. S., Kim, G., Kang, H., Kim, J. H., Chung, W. J., Kim, M. S., Kim, Y. K., Cho, M. H., Jeong, D. H., and Lee, Y. S. (2009) Protein separation and identification using magnetic beads encoded with surface-enhanced Raman spectroscopy. *Analytical Biochemistry 391*, 24-30.

(134) Huh, Y. S., Lowe, A. J., Strickland, A. D., Batt, C. A., and Erickson, D. (2009) Surface-enhanced Raman scattering based ligase detection reaction. *J Am Chem Soc 131*, 2208-13.

(135) Lowe, A. J., Huh, Y. S., Strickland, A. D., Erickson, D., and Batt, C. A. Multiplex Single Nucleotide Polymorphism Genotyping Utilizing Ligase Detection Reaction Coupled Surface Enhanced Raman Spectroscopy. *Analytical Chemistry 82*, 5810-5814.

(136) Wabuyele, M. B., Yan, F., and Vo-Dinh, T. Plasmonics nanoprobes: detection of single-nucleotide polymorphisms in the breast cancer BRCA1 gene. *Analytical and Bioanalytical Chemistry 398*, 729-736.

(137) Aouacheria, A., Navratil, V., Wen, W., Jiang, M., Mouchiroud, D., Gautier, C., Gouy, M., and Zhang, M. (2005) In silico whole-genome scanning of cancer-associated nonsynonymous SNPs and molecular characterization of a dynein light chain tumour variant. *Oncogene 24*, 6133-42.

(138) Nakitandwe, J., Trognitz, F., and Trognitz, B. (2007) Reliable allele detection using SNP-based PCR primers containing Locked Nucleic Acid: application in genetic mapping. *Plant Methods 3*, 2.

(139) Strickland, A. D., and Batt, C. A. (2009) Detection of Carbendazim by Surface-Enhanced Raman Scattering Using Cyclodextrin Inclusion Complexes

on Gold Nanorods. *Analytical Chemistry 81*, 2895-2903.

(140) Huang, W. E., Li, M., Jarvis, R. M., Goodacre, R., and Banwart, S. A. Shining light on the microbial world the application of Raman microspectroscopy. *Adv Appl Microbiol 70*, 153-86.

(141) Qian, X. M., and Nie, S. M. (2008) Single-molecule and single-nanoparticle SERS: from fundamental mechanisms to biomedical applications. *Chem Soc Rev 37*, 912-20.

(142) Vo-Dinh, T., Wang, H. N., and Scaffidi, J. Plasmonic nanoprobes for SERS biosensing and bioimaging. *J Biophotonics 3*, 89-102.

(143) Alvarez-Puebla, R. A., and Liz-Marzan, L. M. Environmental applications of plasmon assisted Raman scattering. *Energy & Environmental Science 3*, 1011-1017.

(144) Scaffidi, J. P., Gregas, M. K., Lauly, B., Carter, J. C., Angel, S. M., and Vo-Dinh, T. Trace molecular detection via surface-enhanced Raman scattering and surface-enhanced resonance Raman scattering at a distance of 15 meters. *Appl Spectrosc 64*, 485-92.

CHAPTER 2

MULTIPLEX SNP GENOTYPING UTILIZING LIGASE DETECTION REACTION COUPLED SERS

Adapted with permission from "Multiplex single nucleotide polymorphism genotyping utilizing ligase detection reaction coupled surface enhanced Raman spectroscopy" Analytical Chemistry (2010) Volume: 82, Issue: 13, Pages: 5810-5814.

Abstract:

Single nucleotide polymorphisms (SNPs) are one of the key diagnostic markers for genetic disease, cancer progression, and pharmcogenomics. The ligase detection reaction (LDR) is an excellent method to identify SNPs, combining low detection limits and high specificity. We present the first multiplex LDR-Surface Enhanced Raman Spectroscopy (SERS) SNP genotyping scheme. The platform has the advantage in that the diagnostic peaks of Raman are more distinct than fluorescence and, in theory, a clinically significant number of markers can be multiplexed in a single sample using different SERS reporters. Here we report LDR-SERS multiplex SNP genotyping of K-Ras oncogene alleles at 10 pM detection levels, optimization of DNA labeling as well as Raman conditions, and the linear correlation of diagnostic peak intensity to SNP target concentration in heterozygous samples. Genomic DNA from typed cells lines was obtained and scored for the K-Ras genotype. These advances are significant as we have further developed our new SNP genotyping platform and have demonstrated the ability to correlate genotype ratios directly diagnostic Raman peak signal intensity.

Introduction:

SNPs are clinically useful for disease diagnosis and the selection of the appropriate therapies.[1-3] The ability to genotype multiple SNPs in limited clinical samples is important due to their potential for heterogeneous distribution. For example, oncogenic K-Ras alleles have been detected at G12V, G12A, G13D, and Q61R.[4] The K-Ras genotype from a patient's tumor is highly informative, as tumors with different genotypes respond differently to treatment regiments.[5-7] Many methodologies have been previously developed for SNP genotyping. Strategies include primer elongation via PCR, enzymatic cleavage, hybridization, and LDR (oligonucelotide ligation), with most of them relying on a fluorescent spectra or mass spectrometry for signal output.[8] Fluorescence is limited as a multiplex reporter due to spectral overlap. Mass spectroscopy is able to deconvolute more complex mixtures since different mass tags can be used[9,10], but the equipment is cumbersome and difficult to integrate into a diagnostic device with a small footprint.

We have recently developed a technology that utilizes SERS to circumvent the spectral overlap of fluorescence spectroscopy while retaining sensitivity and accuracy of LDR for SNP detection.[11] Detection schemes utilizing SERS are advantageous over fluorescence as Raman peaks are approximately 1 nm[12] full width half maximum (fwhm) while fluorescent labels can be 100 times larger fwhm.[13] In addition to our LDR-SERS platform, Raman spectroscopy has been utilized for DNA identification and SNP detection using hybridization platforms [14,15] as well as PCR based systems.[16] Importantly, multiplex identification systems have been developed utilizing SERS technologies that require no additional data processing other than simple peak

recognition.[16-18]

Here we demonstrate the multiplex genotyping capacity of our LDR-SERS technology and how it may be used to identify multiple SNP alleles. Varying Raman enhancer and excitation wavelength conditions were tested to determine their effect on signal to noise ratio of each peak cluster. Additionally, the direct correlation between diagnostic peak intensity and template concentration was demonstrated. Finally, a three-plex detection system was demonstrated with a 10 pmol limit of detection.

Materials and Methods:

Ligase Detection Reaction:

Template DNA used in LDR reactions was genomic DNA extracted from non-diseased colon, DLD1, and SW1116 cell lines for WT, G12D, and G12A detection experiments respectively. The oligonucleotide sequences of all the probes used in these experiments are shown in Table 1. All DNA primers were synthesized (Integrated DNA Technologies Coralville, IA) and adapted by previous work done by Khanna *et al.*[4]. Thermostable 9º North DNA ligase and buffer were purchased from New England Biolabs (Beverly, MA). The LDR reaction contained the following in a 10 μL reaction: 20 pmol of template, 100 pmol of each primer, 1 μL of 9º N DNA ligase, 1 μL of supplied 9ºN DNA ligase 10 X Buffer, and water to 10 μL. The LDR reactions used the following thermocycler program in a MJ Research PTC-200 Peltier Thermo Cycler: 1) 90°C for 2 min 2) 90°C for 30 sec 3) 50°C for 4 min 4) Repeat Steps 2-3 29 times then 50°C for 10 min. 5) Hold at 4°C

LDR functionalization and purification:

The completed LDR reaction mixture was treated with 2 μL of DMSO, mixed, and allowed to sit for 2 mins. 100 picomoles of the NHS ester of thioctic acid was added to the treated LDR reaction and allowed to react for one hr. The reaction mixture was then added to 200 μL of 60 nm Ag or Au nanoparticles and allowed to react for 1 hr and purified as previously described.[11]

Raman spectroscopy measurements:

Raman measurements were made using an inVia Raman spectrometer (INVIA Medical Imaging Solutions, Ann Arbor, Michigan) coupled to a Leica microscope. The experiments were conducted by focusing the excitation laser on the electro-active microwell as previously described.[11 19] The 488 nm and 785 nm laser lines were used as optical excitation sources and the scattered signal was collected by a Peltier-cooled CCD detector. A 50 X (NA=0.55) objective lens was used to focus the laser beam spot onto the sample surface with diameter of about 2 μm. Wave-numbers ranging from 1100 cm^{-1} to 1800 cm^{-1} were examined for all SERS experiments.

Results and Discussion:

An example of our multiplex LDR-SERS scheme is presented in Figure 2-1. An oligonucleotide primer, common to all haplotypes for a given gene locus, binds downstream of a SNP. This primer contains an amine for conjugation to a Raman enhancing nanoparticle after ligation has occurred. A second primer containing a Raman active fluorophore and a discriminating base at the 3' end binds upstream of

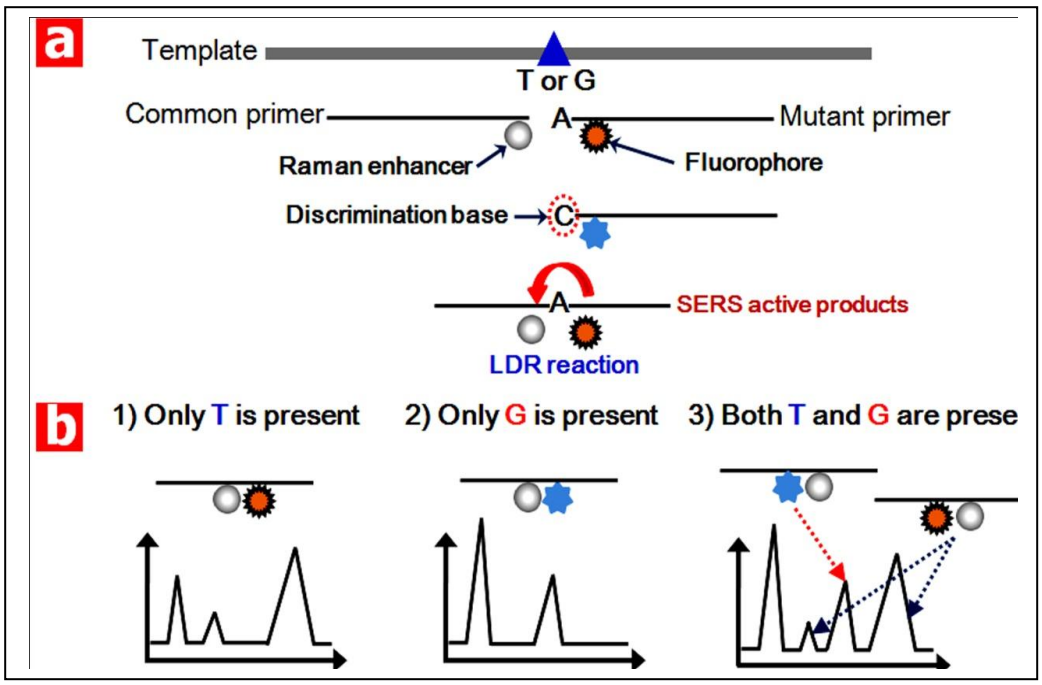

Figure 2-1: A) Overview of LDR/SERS ligation B) Schematic of multiplex SERS spectra. Silver spheres represent silver nanoparticles and colored circle represent fluorophores.

the SNP, adjacent to the first primer. This discriminating, terminal base allows for allele specificity, as ligation only occurs if the upstream primer matches perfectly with the DNA template. Therefore, Raman signal will only be detected if ligation of the two primers occurs, since the Raman enhancer must be very close to the signal source. Different Raman active fluorophores are placed on the SNP allelic specific primers, which produce a signature Raman profile as diagramed in Fig 1b.

As described in Table 1, a TAMRA fluorescent label was attached to the wild type discriminating primer while a fluorescein and 6-carboxyfluorescein (6-FAM) labels were attached to the G12D and G12A discriminating primers respectively. Samples containing all three templates produce an aggregate spectrum that has elements of all Raman reporters, but diagnostic peaks of each marker can still be discerned and quantified. After the ligation occurs, the Raman enhancer is attached to the DNA strand, purified, and then concentrated in an electroactive nanowell. [11,19]

Upon examining the differences in spectra, several possible diagnostic peaks were identified with the most prominent at approximately 1315 cm^{-1}, 1370 cm^{-1}, and 1488 cm^{-1} for fluorescein (G12D), TAMRA (WT), and 6-FAM (G12A) labeled DNA respectively. In order to optimize the SERS output signal and resolution between diagnostic peaks, the interplay between laser excitation wavelength and nanoparticle enhancers was investigated using a two-plex model. Figure 2-2a plots TAMRA labeled DNA SERS intensity as function of laser excitation wavelength and Raman enhancers. While the 785 nm excitation source (Fig 2A3 & 2A4) did provide three-fold more intense peaks at the 1500 cm^{-1} cluster in the TAMRA sample, the 488 nm excitation source gave much more distinct peaks, reducing the peak width of the 1370

cm^{-1} diagnostic peak by a factor of three in both the silver and gold enhanced samples. A similar pattern was seen for fluorescein-labeled DNA in figure 2-2b. The 488 nm laser provided an approximately three-fold higher signal as compared to the 785 nm excitation source for the peak at 1650 cm^{-1} and a 1.4 fold average enhancement when comparing the silver enhanced samples. This is most likely attributable to a resonance Raman effect, where both dyes are excitable to their first electronic state at 488 nm but not at 785 nm.[16 20] Resonance Raman effects can greatly increase Raman signal, which has been previously shown in assays detecting DNA base changes using hybridization format.[14]

An average 1.33 SNR enhancement of silver compared to gold was achieved in the TAMRA sample excited at 785 nm. In the fluorescein labeled sample, an average 3.2 SNR was achieved over gold when excited at 488 nm. SNR of the fluorescein labeled samples excited at 785 nm was not readily comparable in silver versus gold enhancements due to the large peak broadness of the gold enhanced samples. The metal dependent, Raman enhancement trends conform to previously observed behavior that silver is often a better Raman enhancer than gold.[21]

Table 2-1. Primers used in LDR-SERS experiments

Template/Primer	**Sequence for LDR (5′ – 3′)**
Common LDR Primer	5Phos[1]/TGG CG/AmT[2]/ AGG CAA GAG TGC CTT GAC
G12D Mutant LDR Primer	GAA TAT AAA CTT GTG GTA G/FlurT[3]/T GGA GCT G***A***
G12A Mutant LDR Primer	GAA TAT AAA CTT GTG GTA G/6FAM[4]/T GGA GCT G***C***
Wild type LDR Primer	GAA TAT AAA CTT GTG GTA G/TAM[5]/T GGA GCT G***G***

[1]5Phos denotes a 5' phosphorylation; [2]AmT denotes an aminated thymine; [3]FlurT denotes a fluorescein dT. [4]6FAM denotes a 6-Carboxyfluorescein dT [5]TAM denotes a TAMRA dT. The 3′ base in mutant and wild type LDR primers (bold and italic) allow for specific discrimination of the two templates

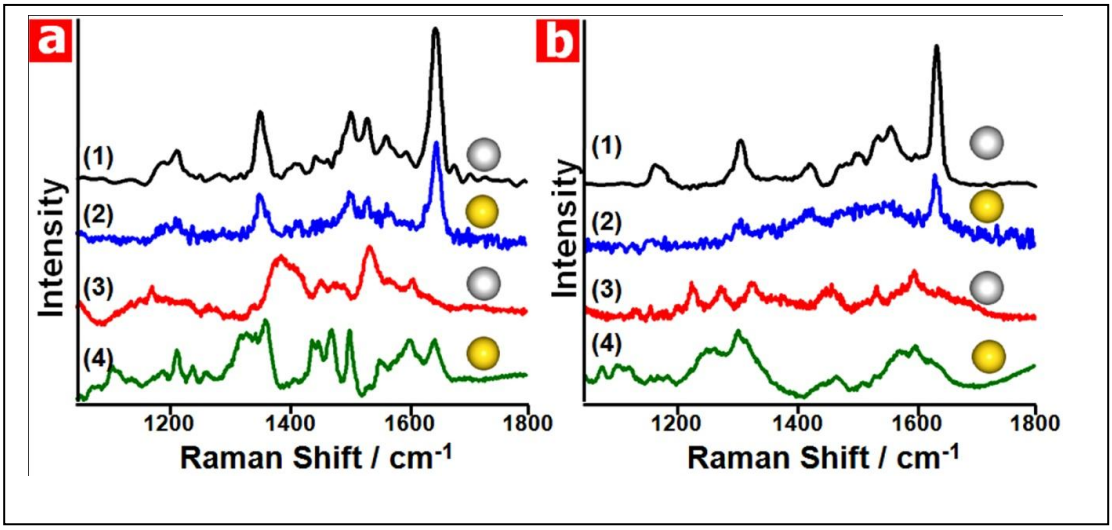

Figure 2-2: Investigation of Raman enhancers and excitation source. Samples 1 and 2 were excited at 488 nm while samples 3 and 4 were excited at 785 nm. Odd numbered samples contained silver Raman enhancers and even numbered samples contained gold Raman enhancers as indicated by colored spheres. A) Wild Type TAMRA labeled DNA. B) G12D mutant fluorescein labeled DNA

This effect is due to the localized surface plasmon resonance of the aggregated silver particles having a greater maximum absorbance than gold and better matching the excitation wavelength. Again, higher Raman signal output may be obtained by matching the excitation wavelength to the absorbance wavelength of the fluorescent label, inducing an electronic transition to achieve surface enhanced resonance Raman (SERRS). Quantitatively maximizing Raman signal based on nanoparticle composition and excitation wavelength has been thoroughly analyzed previously.[22] Design and selection of Raman molecules for multiplex analysis have also been previously investigated.[23-25]

Figure 2-3 shows two-plex data obtained for a mixture of WT and G12D targets using both LDR primers. Figure 2-3a shows the SERS spectra profiles of a mixture of WT and G12D with silver or gold as the SERS enhancer (silver for 1 and 3, gold for 2 and 4) and excitation wavelength of 488 nm (1 and 2) and 785 nm (3 and 4). The multiplex sample conformed to the trends observed in Figure 2-2, with silver nanoparticles demonstrating 1.5 and 2 fold SNR enhancement for the fluorescein and TAMRA diagnostic peaks respectively when excited at 488 nm as compared to gold. The 488 nm laser reduced the peak width of the fluorescein and TAMRA diagnostic peaks by a factor of 1.8 and 1.2 respectively as compared to the 785 nm excitation source for silver enhanced samples. Figure 2-3b shows a resultant two-plex spectra with the fluorescein and TAMRA spectra overlaid, demonstrating that the diagnostic fluorescein peak at ~1315 cm^{-1} is clearly distinguishable from the diagnostic TAMRA peak at ~1370 cm^{-1}, which identify the G12D mutant and wild type genotypes respectively. These spectra were obtained from silver enhanced samples excited at

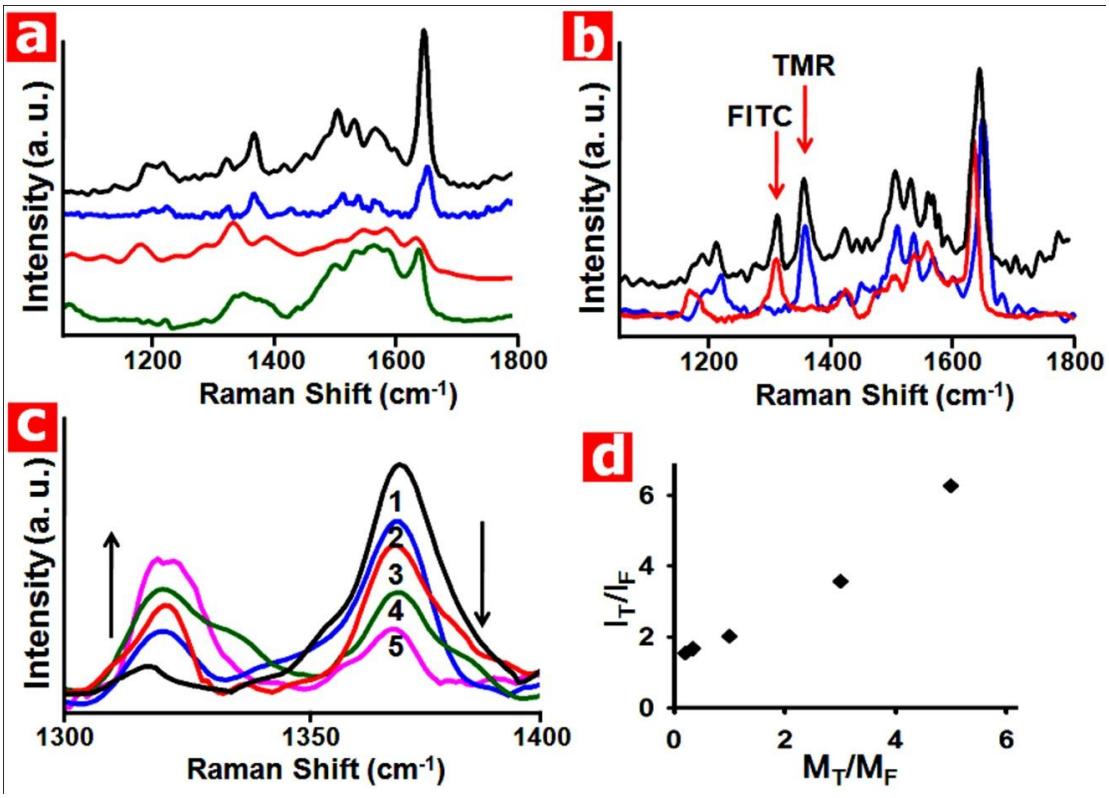

Figure 2-3: Two-plex SNP Samples. A) Mixed genotype SERS spectra. B) Overlay of singleplex SERS spectra with WT in dark grey and mutant in light grey against the multiplex spectrum in black. TAMRA and fluorescein diagnostic peaks are highlighted with labeled arrows. C) Diagnostic peak intensities of mix genotype samples, varying the LDR template concentration of mutant to wild type template DNA as: 1) 0.1:1 2) 0.5:1 3) 1:1 4) 3:1 5) 5:1. D) Plot of template molar ratio against diagnostic peak intensity. I denotes intensity, M denotes moles, T denotes TAMRA, and F denotes Fluorescein.

488 nm. Figure 2-3c depicts the correlation of SNP concentration to signal intensity. In the mixed sample, the population of mutant (fluorescein) to wild type (TAMRA) DNA template was varied in the LDR reaction of at ratios of 0.1:1, 0.5:1, 1:1, 3:1, and 5:1 in samples 1-5 respectively. As expected, as the ratio of mutant to WT SNPs is increased, the 1315 cm^{-1} signal increases while the 1370 cm^{-1} signal decreases.

Figure 2-3d plots the molar ratio of WT to mutant template concentration against signal intensity of the diagnostic peaks as obtained from Figure 2-3c. A linear trend is generated with diagnostic signal intensity directly correlating to the genotype molar ratio. Unlike PCR, LDR does not produce exponential amplification of the product since the product of the ligation is not a template for the LDR primers. The signal is linear with the initial target concentration.

Figure 2-4 demonstrates three-plex capabilities of the system. In the presence of all three diagnostic primers, LDR reactions were run with one, two, or three templates then functionalized with silver nanoparticles and their Raman spectra analyzed. Figure 2-4A1 shows a diagnostic peak for the G12D mutant (fluorescein) at approximately 1315 cm^{-1} . Figures 2-4A2 and 2-4A3 are representative spectra for WT (TAMRA) and G12A (6-FAM) haplotypes respectively. While 1370 cm^{-1} was potentially a diagnostic peak for TAMRA-labeled WT templates it overlaps with the 6-FAM peak seen for the G12A allele. An alternative diagnostic peak for the WT spectrum can be seen at ~1225 cm^{-1} however and can be used for WT haplotype identification. The G12A haplotype has a unique diagnostic peak at ~ 1488 cm^{-1}. Figure 2-4A4 demonstrates that the presence of all three diagnostic primers in the reaction not inhibit two-plex detection, as diagnostic peaks for WT and G12D mutations are

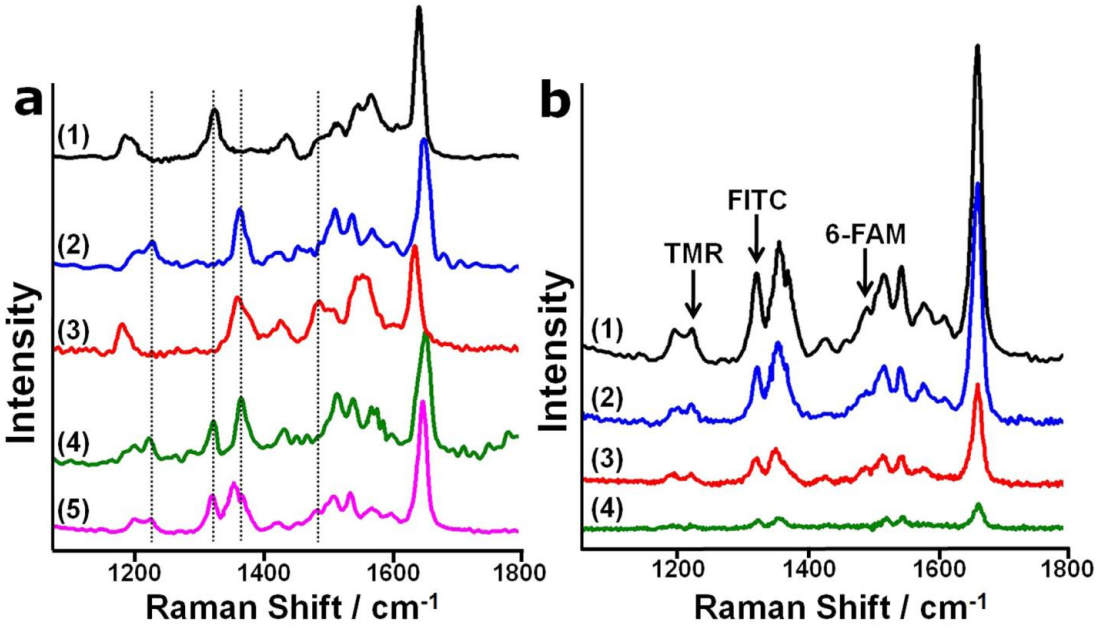

Figure 2-4: Multiplex SNP Samples. A) 1. G12D (Fluorescein) Mutant 2) WT KRAS (TAMRA) 3) G12A (6-FAM) Mutant 4) WT & G12D 2-plex 5) WT, G12D, G12A 3-plex. Dotted lines indicate diagnostic peaks. B) Dilution series of LDR three-plex containing variable amounts of template. 1) 20 pmol 2) 10 pmol 3) 5 pmol 4) 2 pmol

present. Figure 2-4A5 demonstrates detection of all three haplotypes with diagnostic peaks for all three alleles clearly present. Figure 2-4B shows a dilution series that demonstrates a 10 pmol limit of detection.

Conclusions:

Here we have demonstrated an important step toward a LDR-SERS detection platform for SNPs. This system allows accurate discrimination of multiple alleles, and does not require a microarray format or capillary electrophoresis.[26] Additionally, it displays the ability to quantify SNP allelic ratios based on relative signal intensity. This technology is an important advancement in moderate scale SNP detection as it retains the advantages previously shown with LDR and increases the potential for multiplex detection in a relatively simple technology platform. SERS multiplex detection of oligonucleotides labeled with common fluorophore tags has been previously demonstrated.[27 28] It is important to note that fluorophores are often used as Raman tags due to their wide availability on oligonucleotides, but any chromophore or molecule with a high Raman cross section and unique spectral signature could be used as a label.[29, 30] This opens up a very large spectral space for detection and multiplexing possibilities. Multiplexing is particularly amenable to this system because even if diagnostic peaks overlap, their sources can still be determined through spectral fitting analysis, which identifies peaks not discovered by linear analysis and direct observations. [28] Furthermore, isotopically different variants of a given probe may be detected as different signals allowing for further multiplexing.[31] Due to the adaptability and sensitivity of our system, we believe our technology is a step towards

an eventual point-of-care genotype analysis system for clinically relevant SNPs. In order to achieve this point-of-care goal, attachment of Raman enhancers to oligonucleotides prior to the ligase detection reaction must be achieved and is currently being investigated.

.

References:

(1) Ching, A.; Caldwell, K. S.; Jung, M.; Dolan, M.; Smith, O. S.; Tingey, S.; Morgante, M.; Rafalski, A. J. *BMC Genet* **2002**, *3*, 19.

(2) Mehta, A. M.; Jordanova, E. S.; Corver, W. E.; van Wezel, T.; Uh, H. W.; Kenter, G. G.; Jan Fleuren, G. *Genes Chromosomes Cancer* **2009**, *48*, 410-418.

(3) Nam, R. K.; Zhang, W. W.; Trachtenberg, J.; Seth, A.; Klotz, L. H.; Stanimirovic, A.; Punnen, S.; Venkateswaran, V.; Toi, A.; Loblaw, D. A.; Sugar, L.; Siminovitch, K. A.; Narod, S. A. *Clin Cancer Res* **2009**.

(4) Khanna, M.; Park, P.; Zirvi, M.; Cao, W.; Picon, A.; Day, J.; Paty, P.; Barany, F. *Oncogene* **1999**, *18*, 27-38.

(5) Colomer, R.; Monzo, M.; Tusquets, I.; Rifa, J.; Baena, J. M.; Barnadas, A.; Calvo, L.; Carabantes, F.; Crespo, C.; Munoz, M.; Llombart, A.; Plazaola, A.; Artells, R.; Gilabert, M.; Lloveras, B.; Alba, E. *Clin Cancer Res* **2008**, *14*, 811-816.

(6) Fasching, P. A.; Kollmannsberger, B.; Strissel, P. L.; Niesler, B.; Engel, J.; Kreis, H.; Lux, M. P.; Weihbrecht, S.; Lausen, B.; Bani, M. R.; Beckmann, M. W.; Strick, R. *J Cancer Res Clin Oncol* **2008**, *134*, 1079-1086.

(7) Gusella, M.; Padrini, R. *Pharmacogenomics* **2007**, *8*, 985-996.

(8) Kim, S.; Misra, A. *Annu Rev Biomed Eng* **2007**, *9*, 289-320.

(9) Tost, J.; Gut, I. G. *Clin Biochem* **2005**, *38*, 335-350.

(10) Tang, K.; Fu, D. J.; Julien, D.; Braun, A.; Cantor, C. R.; Koster, H. *Proc Natl Acad Sci U S A* **1999**, *96*, 10016-10020.

(11) Huh, Y. S.; Lowe, A. J.; Strickland, A. D.; Batt, C. A.; Erickson, D. *J Am Chem Soc* **2009**, *131*, 2208-2213.

(12) McCreery, R. L. *Raman spectroscopy for chemical analysis*; John Wiley & Sons: New York, 2000.

(13) Lakowicz, J. R., Third Edition. ed.; Springer Science+Business Media, LLC: [S.l.], 2006.

(14) Cao, Y. C.; Jin, R.; Mirkin, C. A. *Science* **2002**, *297*, 1536-1540.

(15) Mahajan, S.; Richardson, J.; Brown, T.; Bartlett, P. N. *J Am Chem Soc* **2008**, *130*, 15589-15601.

(16) Graham, D.; Mallinder, B. J.; Whitcombe, D.; Watson, N. D.; Smith, W. E. *Anal Chem* **2002**, *74*, 1069-1074.

(17) Jun, B. H.; Kim, J. H.; Park, H.; Kim, J. S.; Yu, K. N.; Lee, S. M.; Choi, H.; Kwak, S. Y.; Kim, Y. K.; Jeong, D. H.; Cho, M. H.; Lee, Y. S. *J Comb Chem* **2007**, *9*, 237-244.

(18) Sun, L.; Yu, C.; Irudayaraj, J. *Anal Chem* **2008**, *80*, 3342-3349.

(19) Huh, Y. S.; Chung, A. J.; Cordovez, B.; Erickson, D. *Lab Chip* **2009**, *9*, 433-439.

(20) Faulds, K.; McKenzie, F.; Smith, W. E.; Graham, D. *Angew Chem Int Ed Engl* **2007**, *46*, 1829-1831.

(21) Zeman, E. J.; Schatz, G. C. *Journal of Physical Chemistry* **1987**, *91*, 634-643.

(22) Stokes, R. J.; Macaskill, A.; Lundahl, P. J.; Smith, W. E.; Faulds, K.; Graham, D. *Small* **2007**, *3*, 1593-1601.

(23) Faulds, K.; Smith, W. E.; Graham, D. *Anal Chem* **2004**, *76*, 412-417.

(24) Graham, D.; Faulds, K. *Chem Soc Rev* **2008**, *37*, 1042-1051.

(25) Graham, D.; Faulds, K.; Thompson, D.; Mackenzie, F.; Stokes, R.; Macaskill, A. *Biochem Soc Trans* **2009**, *37*, 441-444.

(26) Tobler, A. R.; Short, S.; Andersen, M. R.; Paner, T. M.; Briggs, J. C.; Lambert, S. M.; Wu, P. P.; Wang, Y.; Spoonde, A. Y.; Koehler, R. T.; Peyret, N.; Chen, C.; Broomer, A. J.; Ridzon, D. A.; Zhou, H.; Hoo, B. S.; Hayashibara, K. C.; Leong, L. N.; Ma, C. N.; Rosenblum, B. B.; Day, J. P.; Ziegle, J. S.; De La Vega, F. M.; Rhodes, M. D.; Hennessy, K. M.; Wenz, H. M. *J Biomol Tech* **2005**, *16*, 398-406.

(27) Faulds, K.; Jarvis, R.; Smith, W. E.; Graham, D.; Goodacre, R. *Analyst* **2008**, *133*, 1505-1512.

(28) Lutz, B. R.; Dentinger, C. E.; Nguyen, L. N.; Sun, L.; Zhang, J.; Allen, A. N.; Chan, S.; Knudsen, B. S. *ACS Nano* **2008**, *2*, 2306-2314.

(29) Fruk, L.; Grondin, A.; Smith, W. E.; Graham, D. *Chemical Communications* **2002**, 2100-2101.

(30) Sun, L.; Yu, C.; Irudayaraj, J. *Anal Chem* **2007**, *79*, 3981-3988.

(31) Pradeep, N. P.; Shirshendu, K. D.; Davisson, V. J.; Dor, B.-A. *Journal of Raman Spectroscopy* **2009**, *9999*, n/a.

CHAPTER 3

Fluorescence Quenching and Binding Kinetics of Lipophilic Stains in CTAB Coated Gold Nanorods

Abstract:

We have examined the fluorescence quenching and binding kinetics of the lipophilic stains Nile Red and IR-786 by CTAB coated gold nanorods. Analysis of quenching showed IR-786 was quenched approximately ten times more efficiently than Nile Red under identical conditions, due to its emission peak matching the absorbance plasmon of the gold particles. We additionally examined the binding characteristics of the stains to test their affinity for the CTAB coated nanorods using a surface plasmon resonance platform. Nile red and IR-786 displayed similar K_ds of 10.3 ± 0.68 μM and 13.33 ± 0.72 μM respectively, as determined by global fit analysis. Here we demonstrate the quenching ability of gold nanorods for lipophilic dyes, and for the first time, describe the binding characteristics of the stains using a surface plasmon resonance platform. This platform permits the measurement of analyte diffusion into bilayer-functionalized nanoparticles in real time with a high degree of analytical precision and demonstrates the ability to model nanorod bilayer trafficking kinetics under a variety of conditions.

Introduction:

Cetyltrimethyl Ammonium Bromide (CTAB) coated nanorods have become important to the field of nanotechnology for their use in small molecule detection[(1)], effects on cell morphology[(2)], and cellular imaging.[(3)] These particles are particularly interesting because of their bimodal absorbance plasmon, as well as their CTAB coating, which is located only along the longitudinal axis of the rods, leaving the terminal ends available for regiospecific functionalization.[(4-6)] The longitudinal plasmon band of the particles is highly tunable,[(7),(8)] becoming more red shifted as the aspect ratio of the particles is increased.[(9)] This tunability is useful as the absorbance peak can be adjusted for Förster resonance energy transfer **(**FRET**)** or Raman experiments.[(10-12)] While the fluorescence quenching mechanism of nanocrystals (quantum dots) by CTAB nanorods has been investigated,[(11),(13)] the interaction of highly lipophilic fluorescent stains with CTAB nanorods has not previously been explored. Characterization of fluorescence quenching capabilities and binding kinetics of CTAB coated nanorods is highly relevant, as CTAB nanorods can be excellent carriers for various substances that interact with biological systems. They have been shown to selectively release rhodamine B[(14)] as well as DNA[(15)], depending on laser stimulation conditions. Nanorods functionalized with folate have been used for localized hyperthermic therapy demonstrating the importance of both biological functionalization as well as light absorption properties.[(16)] CTAB itself has been shown to be a good carrier of biomolecules, carrying DNA vaccines for muscosal delivery,[(17)] and have preferential uptake by tumor vasculature over healthy vasculature due to excess anionic lipids in the tumor vasculature.[(18)] Here we

characterize the fluorescence quenching characteristics of CTAB nanorods with the stains Nile red and IR-786, and further investigate the binding kinetics of the stains, demonstrating the potential of SPR to be used as a model for analyte trafficking in nanorods.

Nile red (Nile blue oxazone) is a well characterized, lipophilic stain originally described in 1907.[19] It is strongly fluorescent, but only in hydrophobic environments and is generally used as a lysochrome. *In situ*, Nile red allows for specific detection of intracellular lipid vesicles when excited at approximately 500 nm and yellow fluorescence is observed (515-560 nm).[20] Stronger, red fluorescence that is less sensitive to the hydrophobicity of the environment is detected when Nile red is excited at approximately 550 nm and emission greater than 590 nm is observed.[20] IR 786 is a cationic, lipophilic stain designed to absorb and emit in the near IR, avoiding the intrinsic autofluorescence of tissue when excited with visible light. IR-786 has been shown to be particularly useful for studying myocardial blood flow[21] as well as brown adipose tissue which regulates adaptive thermogenesis.[22], [23] We have chosen to use Nile red and IR-786 due to the specific placement of their emission peaks and their lipophilicity. The Nile red emission maximum falls between the two absorption peaks of the nanorods while the emission maximum of IR-786 closely matches the longitudinal absorbance maximum of the nanorods. This demonstrates how stains may be matched to particles of specific aspect ratios and absorbance peaks. The stains were also chosen for their lipophilicity, assuring their interaction with the CTAB bilayer.

To examine the binding kinetics of each of the stains, a surface plasmon resonance platform was chosen. Examining the binding affinities of the dyes to the particles additionally demonstrates that the fluorescence quenching of the particles was a function of absorbance wavelength and not differential binding. Surface plasmon resonance has been used extensively to characterize the binding of antibodies to immobilized antigens[24-26] as well as small molecules to ligands[27-29] and lipid bilayers.[30-32] To our knowledge, this investigation is the first to test the binding of a ligand directly to a CTAB bilayer without other receptors such as surface protein[33-35] via surface plasmon resonance. This platform is useful because it applies broadly to surface functionalized nanoparticles that are used as carriers for non-covalently bound ligands. Other methods rely on fluorescence or specific functional groups to track ligand release while SPR simply relies on the change in refractive index as binding occurs. The combination of determining fluorescence quenching capability and the binding kinetics of almost any analyte that will bind the functionalization layer makes this platform an especially powerful tool for monolayer or bi-layer coated nanoparticles used as carriers.

Experimental Section:

All reagents were purchased in the highest purity available. Silver nitrate, chloroauric acid, sodium borohydride, ascorbic acid, IR-786 iodide and Nile red were purchased from Sigma Aldrich (St. Louis, MO). Hexadecyl-trimethyl-ammonium bromide (CTAB) was purchased from Fluka (Sigma Aldrich, St. Louis, MO). It has

been noted that there can be significant variability in successful synthesis of CTAB coated nanorods due to lot to lot variability of CTAB.[36] We therefore report the CTAB catalog number, lot number and filling code as 52365, 1340943, and 53407250 respectively. Reichert Analytical Instruments (Depew, NY) provided bare, gold SPR chips (Catalog no. 13206060).

Nanorod Preparation and Characterization.

Biaxially coated CTAB Nanorods were prepared and purified as described previously.[37] [1] A 40.24 ± 1.33 x 13.68 ± 0.98 nm size and rod shape were confirmed by transmission electron micrograph on a JEOL 1200EX transmission electron microscope as seen in Figure 3-1, using 200 mesh grids. Variability in nanorods size is denoted as standard deviation and was determined by measuring 20 different rods in each of 10 different fields of view at a given magnification. After concentration via centrifugation at 8000 G for 10 minutes and resuspension in water, the final nanoparticle concentration was found to have an absorbance equivalent to 16.5 AU at 775 nm which corresponds to approximately 2.0 mg/ml of particles. Mass of the particles was characterized by determination of their dry weight after purification from excess CTAB.

Fluorescence Measurements.

Fluorescence Measurements were taken on a Perkin Elmer LS50B fluorimeter. All samples were prepared identically and contained 1 mM CTAB, 50 nM Nile Red or IR-786, 0.05% (v/v) DMSO and nanorod concentrations as noted in the text. Fluorescent

scans were taken from 550 nm to 875 nm. Each sample was measured 10 times and their output signals averaged. Three independent samples were run for each concentration and stain. Excitation slits were set to 10 nm, emission slits were set to 5 nm, and dwell time was 500 nm/min. Nile Red was excited at 545 nm and IR-786 was excited at 745 nm.

Surface Plasmon Resonance Measurements.

Surface plasmon resonance measurements were taken on a dual channel Reichert Surface Plasmon Resonance Spectrophotometer SR7000DC. Bare gold SPR chips were cleaned with ethanol prior to use and dried with nitrogen gas. The chip surface was functionalized by flowing Buffer A (1 mM CTAB and 0.05% (v/v) DMSO) in aqueous solution through both channels at 25 µl/min overnight. This same buffer was used as sample buffer between injections. Samples containing Buffer A and varying concentrations of Nile Red or IR-786 were injected for 540 seconds, and after this time buffer was again applied and the sample was allowed to dissociate for 200 seconds. The chip was then washed with water for 200 seconds, clearing off the CTAB bilayer and sample. Buffer A was then flowed over the chip for 200 seconds to refunctionalize the chip. Response curves were aligned, cleaned, and analyzed for equilibrium fit in Scrubber (BioLogic Software, Campbell, Australia). Scrubber was also utilized to subtract out the refractive index change caused by DMSO in the solvent system, by utilizing the "DMSO" function and running a DMSO standard curve. BIAevaluation (Biacore Life Sciences, Piscataway, NJ) was utilized for global fit analysis of the SPR data.

Results and Discussion:

UV/Vis Absorption and Fluorescence Quenching:

CTAB coated gold nanorods were prepared by standard seed mediated growth methodology and characterized by TEM (Figure 3-1). The size of the rod shaped particles was determined to be 40.24 ± 1.33 x 13.68 ± 0.98. An absorbance spectrum of nanorods was taken from 400 to 800 nm (Figure 3-2) showing the bimodal absorbance peaks characteristic of nanorods. The aspect ratio of these rods was approximately 3, with absorption maxima at approximately 550 nm and 800 nm for the latitudinal and longitudinal absorption plasmons respectively. The intensity of the longitudinal peak was approximately 2.8 times more intense than the latitudinal absorption peak. The absorption minimum of the nanorods was noted to be approximately 650 nm. In order to test the fluorescence quenching capacity of the rods, the stains Nile red and IR-786 were chosen to fall between the two absorbance peaks and match the longitudinal absorbance maximum of the nanorods respectively. Both Nile Red and IR-786 require a non-polar environment to fluoresce, so a relatively non-polar solvent of 0.05% (v/v) DMSO and 1 mM CTAB in water was used. This solution is above the critical micellular concentration of CTAB(38), which will induce micelle formation and fluorescence from the stains. This buffer was found to provide high levels of fluorescence for both stains, and inclusion of CTAB in the buffer also prevents the nanorods from precipitating which occurs at lower levels of CTAB in solution. Nile red was excited at 545 nm, producing an emission

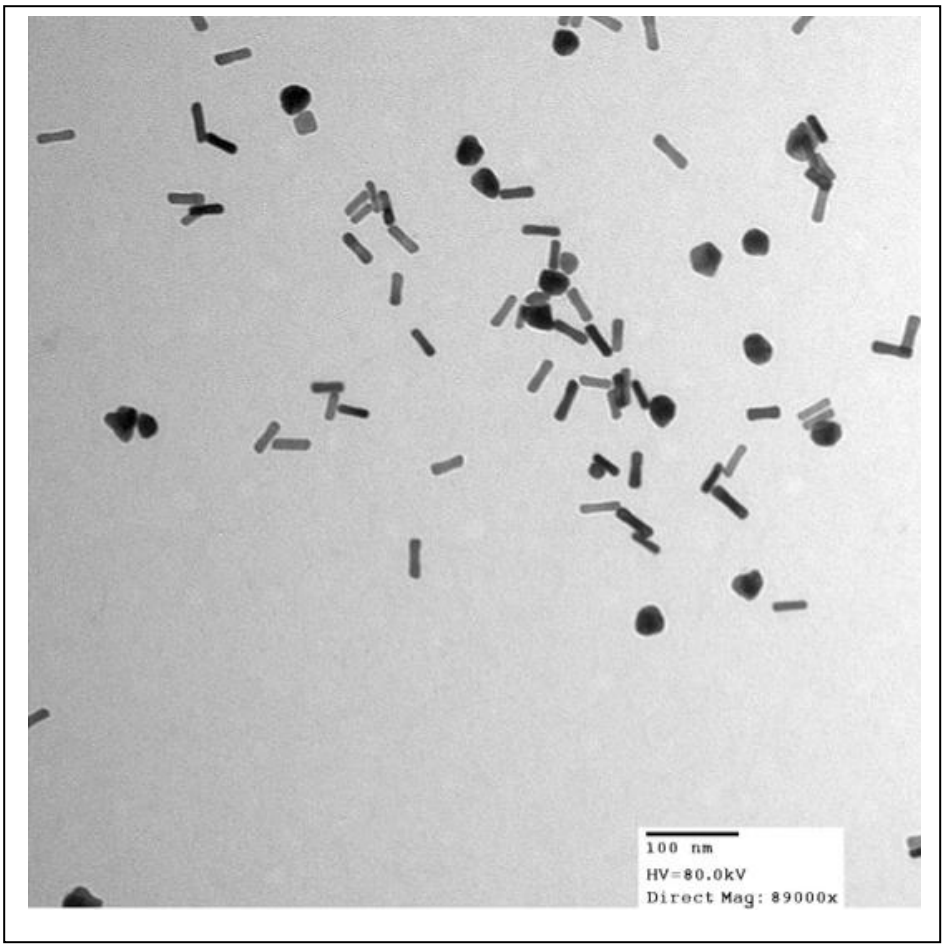

Figure 3-1.TEM image of CTAB coated nanorods at 89000x magnification.

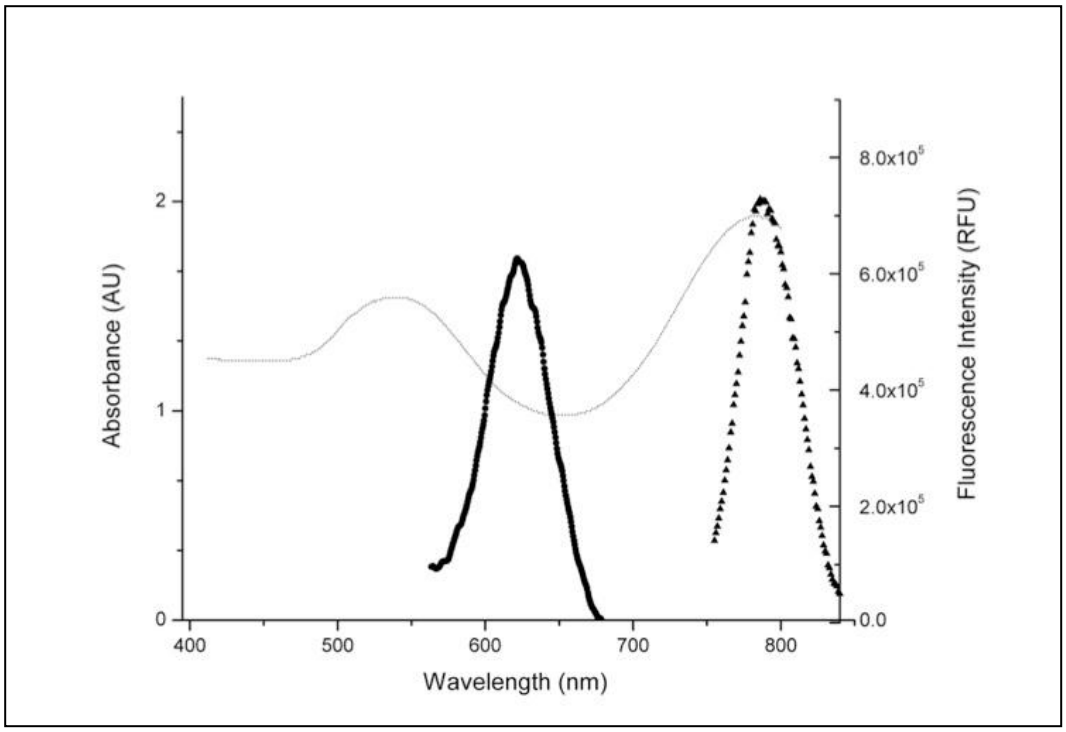

Figure 3-2: UV/Vis absorption spectrum of nanorods (solid grey line, AU) and fluorescent emission peaks of Nile red (black circles, RFU) and IR-786 (black triangles, RFU). The Nile Red falls between the two absorbance plasmons of the nanorods while the IR-786 matches the longitudinal absorbance plasmons.

maximum around 625 nm while IR-786 was excited at 770 nm producing an emission maximum around 790 nm as seen in Figure 3-2. Additionally, Figure 3-2 illustrates how the emission maxima of Nile red and IR-786 falls between absorbance peaks and match the latitudinal absorbance maximum of the nanorods respectively.

Increasing amounts of nanorods were added to buffer solutions containing 50 nM stain to test their fluorescence quenching capacity. Figure 3-3 shows a fluorescence-quenching curve plotting particles added against the percent of control fluorescence at 525 nm for Nile red and 790 nm for IR-786. A saturation curve was observed for both stains with Nile red reaching complete quenching after 104 μg of particles had been added while IR-786 was nearly completely quenched after only 10 μg of particles had been added. This correlates to an approximate tenfold increase in quenching capacity of IR-786 over Nile red. This would be expected as the absorbance maximum of the rods matches well with the emission maximum of the IR-786. Due to the fluorescence quenching behavior exhibited by the nanorods, we were interested in the binding kinetics of stains to the rods. Additionally, determining the relative binding affinities would differentiate whether quenching was only a function of absorbance-emission matching or whether differential binding of the stains contributed.

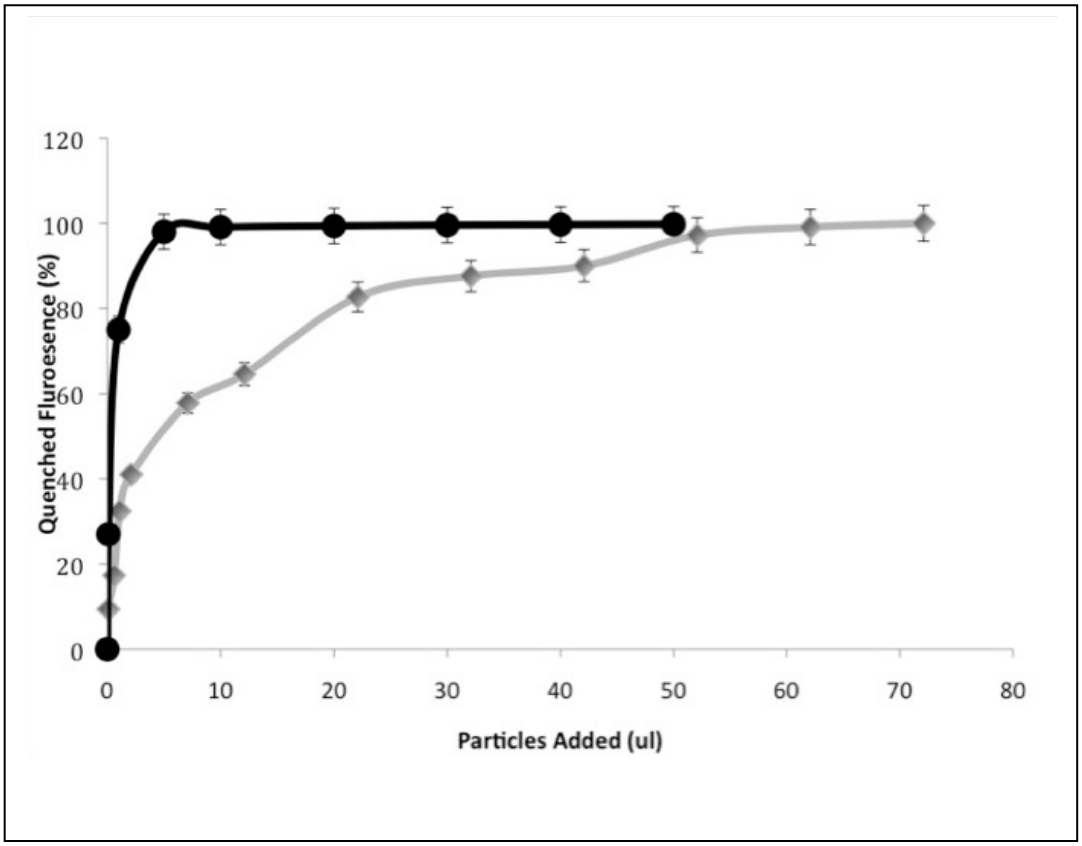

Figure 3-3: Fluorescence quenching curve of Nile red (grey diamonds) and IR-786 (black circles) by nanorods, plotting particles added against percent of control fluorescence quenched at respective emission maxima. Both dyes reached saturation, indication complete quenching, with IR-786 being quenched approximately 10 times faster than Nile red.

Binding Kinetics of Nile Red and IR-786:

To investigate the binding kinetics of the lipophilic stains to CTAB coated nanorods, a bare gold SPR chip was functionalized with CTAB and the binding kinetics of the stains were determined by surface plasmon resonance. Figure 3-4 depicts the observed response curve when functionalizing the gold SPR chip for the first time with the CTAB buffer solution. In Figure 3-4, the water sections of the chromatogram illustrate the change in response from water being injected through sample valve then the buffer line as the sample valve is shut off. During the bilayer formation phase, the running buffer was changed to CTAB/DMSO solution and a rapid increase in response is observed as CTAB begins to functionalize the chip. Interestingly, without any change in conditions, another response spike is seen near the end of segment CD. The initial upward trend corresponds to the accumulation of CTAB micelles on the gold chip surface. It is safe to assume CTAB micelle formation as the solution is above CTAB's critical micelle concentration of 0.8 mM.[(38)] The second spike in refractive index response is most likely attributable to a change on the chip's surface from a conglomeration of micelles to a CTAB bilayer. The removal section of the graph illustrates a water injection to clear the chip. In the refunctionalization phase, water injection was stopped and the CTAB buffer was again passed over the chip. The response curve immediately returned to the bilayer level of response. The micellular intermediate only appeared during the first functionalization of a new chip, never after subsequent clearings with water. This behavior was observed with several different chips used. The micellular intermediate

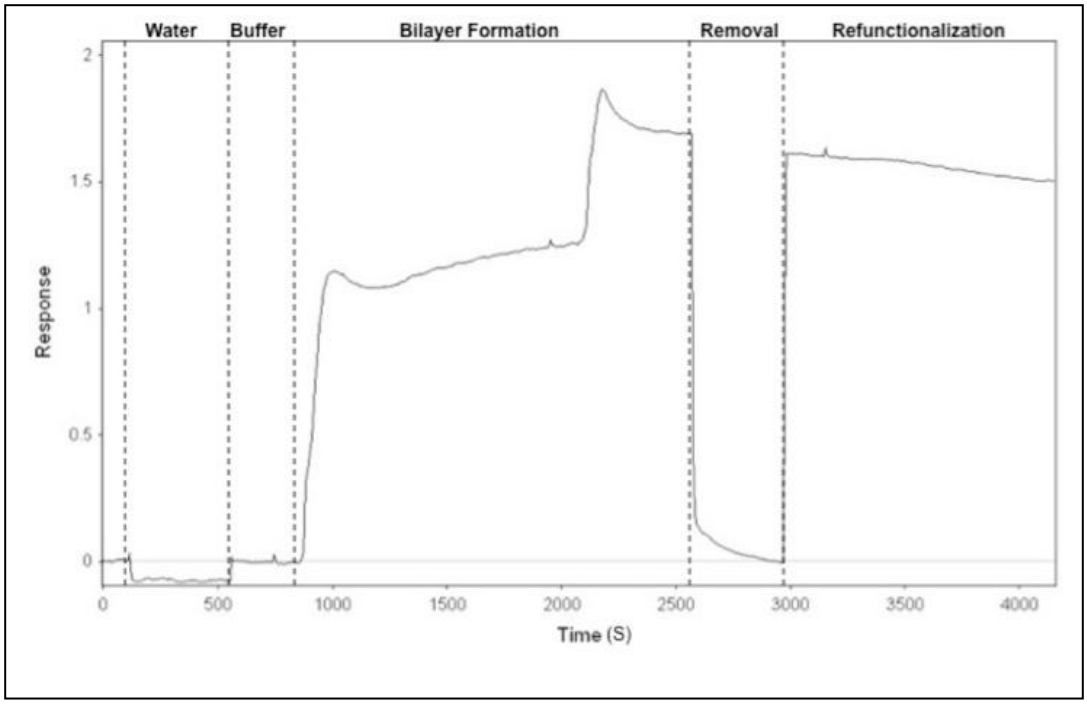

Figure 3-4: Initial functionalization of SPR chip plotting flow time against signal response at 25 µl/min. As noted on the graph water is flowed through the sample valve then the buffer line. The chip is then functionalized with CTAB and stripped with water. The chip is then refuctionalized and buffer is allowed to flow overnight.

was not observed when a flow rate faster than 25 µl/min was used to functionalize the chip.

After establishing the CTAB bilayer on the SPR chip, Nile red or IR-786 were injected in increasing concentration from 20 nM to 1 uM. Note that the injection buffer containing the dyes also contained CTAB above the critical micelluar concentration, thus the dyes were contained in micelles and were not exposed to aqueous solution. Figure 3-5A plots the response level against time as Nile red was injected and allowed to dissociate from the CTAB functionalized chip. The solid, black lines represent the response recorded by the instrument while the dashed, grey lines demonstrate a global fit performed on the data using the Langmuir model built into the Biaevaluation software. Figure 3-5B plots increasing analyte concentration against response levels detected at equilibrium. The Langmuir model built into Scrubber SPR analysis software was used to fit the curve to the data points in Figure 3-5B. Both the global fit as seen in Figure 3-5A and the equilibrium fit in Figure 3-5B correlate well with a Langmuir binding profile. Utilizing Scrubber SPR analysis software, an equilibrium fit was first performed using the data from Figure 3-5B to determine an equilibrium dissociation constant (K_{Deq}) of 9.2 µM of Nile red binding to CTAB with a K_a of 1.1 x 10^5 $M^{1-}s^{-1}$. The Langmuir curve fit the model well with a chi-square value of 1.92. A chi square value of less than ten demonstrates a good statistical fit for sensograms with normal noise levels.

The response curves were then analyzed with BIAevalution using a global fit analysis. A Langmuir model, a Langmuir model with mass transport, and a competing reaction model were used for data fitting analysis. Due to the small molecular weight

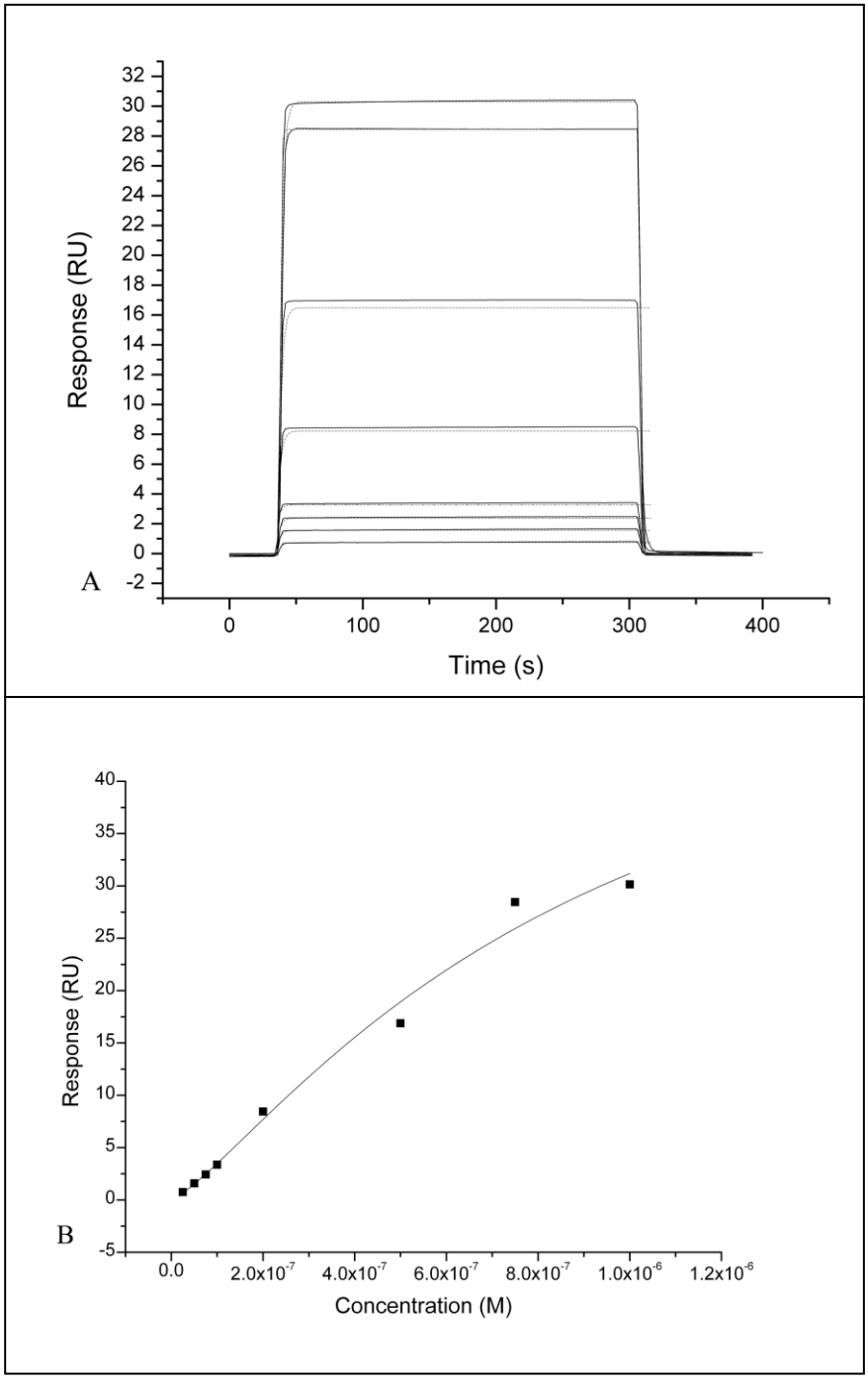

Figure 3-5: Nile red SPR data. A) Raw response curve over time depicting injection, equilibrium, and dissociation. Black, solid lines plot signal recorded while grey, dashed lines depict a Langmuir fit to the data. Response curves correspond to concentrations of 20 nM, 50 nM, 75 nM, 100 nM, 200 nM, 500 nM, 750 nM, and 1 µM. B) Plot of Nile red concentration against response at equilibrium. Langmuir fit seen in grey.

of Nile Red and observed K_a of less than 1.0 x 10^6 $M^{1-}s^{-1}$, mass transport significantly affecting kinetic values was unlikely but considered.[39] As expected, no meaningful fit was obtained. In the competing reaction model, a large variety of molecular weights and concentrations were modeled with no meaningful fit. The Langmuir model without mass transport provided the only meaningful fit, as seen from the chi-square values in Table 3-1. The global fit of Nile Red binding produced a K_D of 10.3 ± 0.68 µM with a K_a of 1.01 x 10^5 $M^{1-}s^{-1}$ and a chi-square value of 1.78. This demonstrates the global fit utilizing a Langmuir model matched the data very well and produced a dissociation constant very similar to that seen from the equilibrium fit. The IR-786 data was analyzed in a similar manner as seen in Figure 3-6, demonstrating a K_{Deq} of 12.82 µM and a chi-square value of 2.46 for the equilibrium fit. Global fit analysis again showed that a Langmuir model best fit the data, as opposed to the competition and Langmuir with mass transport models (Table 3-1). A K_D of 13.33 ± 0.72 µM was determined for IR-786 using the global, Langmuir fit with a chi-square value of 4.53. The slightly higher chi-square values for the IR-786 data as compared to the Nile Red data are due to the poorer fit at higher concentrations but still fall well within the ninety-five percent confidence index. Experiments were repeated at higher flow rates but no statistically significant change in binding profile was observed.

SPR experiments indicate that Nile Red and IR-786 bind to CTAB coated gold SPR chips with similar affinity, having K_Ds in the low micromolar range. These studies also indicate the stains tend to bind in a Langmuiric fashion to the CTAB

Stain	Model	Chi Square Value
IR-786	Langmuir (1:1)	4.51
IR-786	Langmuir with Mass Transfer	21.5
IR-786	Competing Reaction	213
Nile Red	Langmuir (1:1)	1.78
Nile Red	Langmuir with Mass Transfer	28.6
Nile Red	Competing Reaction	177

Table 3-1: Chi square values for global fit of SPR response curves.

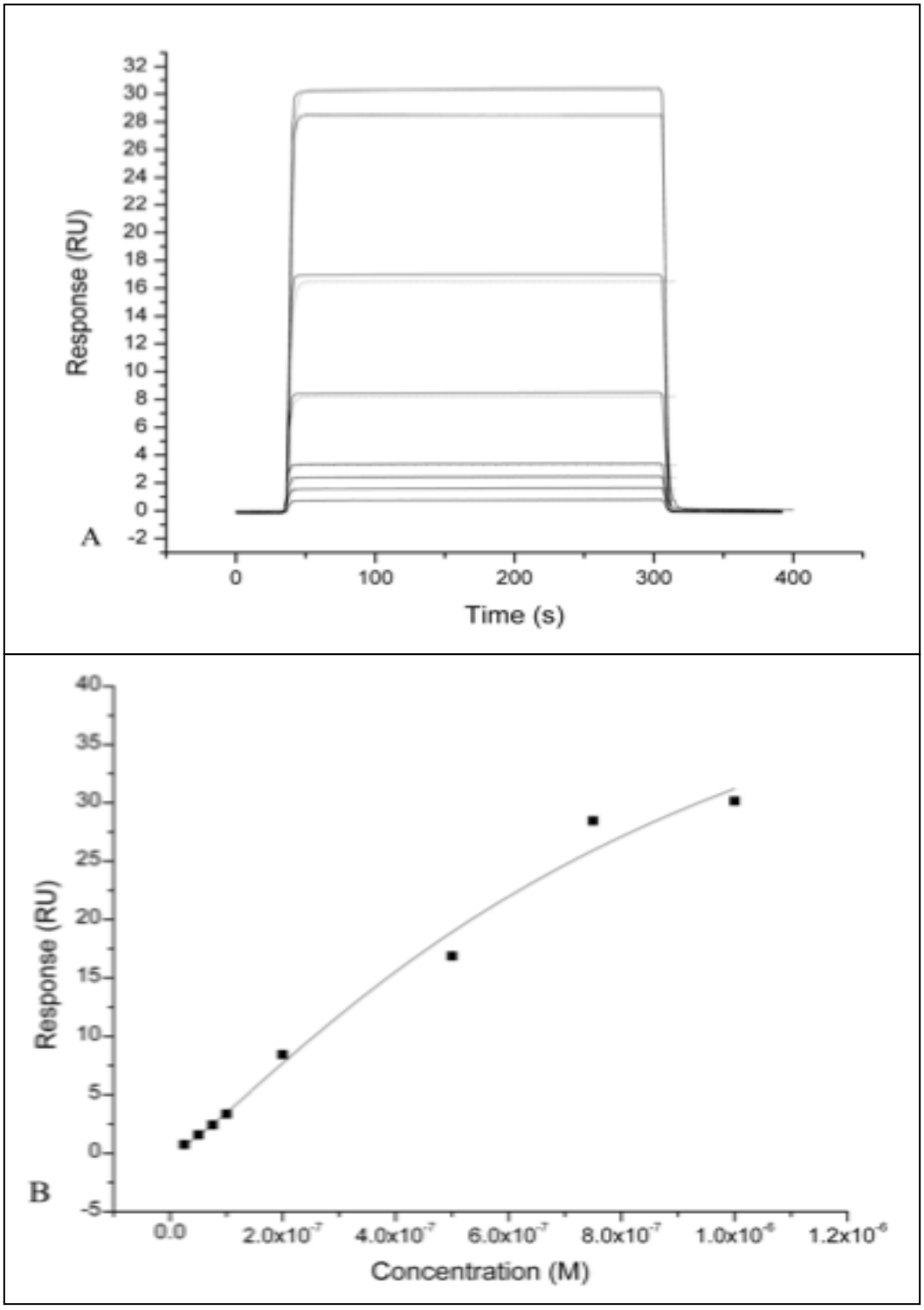

Figure 3-6: IR-786 SPR data. A) Raw response curve over time depicting injection, equilibrium, and dissociation. Black, solid lines plot signal recorded while grey, dashed lines depict a Langmuir fit to the data. B) Plot of Nile red concentration against response at equilibrium. Langmuir fit seen in grey.

bilayer. The determination of similar binding profiles of the two stains is important as it excludes differential binding profiles as the cause of the nanorods to quench IR-786 fluorescence ten times better than Nile red. The SPR studies were also able to show a transition from micelle to bilayer on the SPR chip, demonstrating that binding to the SPR chip was a good proxy to binding directly to CTAB coated nanorods.

Conclusions:

We concluded that CTAB coated nanorods are able to quench fluorescence of the lysochromes Nile red and IR-786, with IR-786 being quenched ten times more efficiently because its emission maximum matches the absorbance maximum of the nanorods. We additionally determined the dissociation constants of Nile red and IR-786 to be 10.3 ± 0.68 μM and 13.33 ± 0.72 μM respectively via surface plasmon resonance, which excludes preferential binding as the cause of different fluorescence quenching ratios. While conducting SPR experiments, we were also able to demonstrate a transition to a CTAB bilayer upon primary functionalization of the SPR chip. It is important to note, that although a control containing only CTAB micelles was not run during the SPR experiments, the effect of micelles during dye binding events does not alter the kinetics measurements because the curve fitting model accounts for the buffer baseline signal, which contains CTAB micelles. Since the buffer contained the same CTAB micelluar concentration as the dye solutions, the effect of the micelles was subtracted by the curve fitting software when a baseline was established and all response curves were normalized to that baseline. The lack of

influence from micelle binding on dye kinetics can be further extrapolated from the functionalization of the chip in Figure 4 and the signal response from Figures 5 and 6. During functionalization of the chip, a response intensity of only approximately 1.5 was obtained. At all concentrations measured, a higher equilibrium response was obtained as compared to the micelles alone. Since these values were used to fit K_{Deq}, and they fit the langmuiric model extremely well, this would further argue that the effect of micelle trafficking during dye binding events does not have a significant effect on dye dissociation constant measurements. Overall, the information gathered here demonstrates the potential for the energy-coupling and physical interactions of hydrophobic, biological stains with nanorods due to the high degree of tunabilty of rod absorption and the wide selection of stains available.

References:

1. Strickland AD, Batt CA (2009) Detection of carbendazim by surface-enhanced Raman scattering using cyclodextrin inclusion complexes on gold nanorods. Anal Chem 81 (8):2895-2903. doi:10.1021/ac801626x

2. Sisco PN, Wilson CG, Mironova E, Baxter SC, Murphy CJ, Goldsmith EC (2008) The Effect of Gold Nanorods on Cell-Mediated Collagen Remodeling. Nano Letters 8 (10):3409-3412

3. Murphy CJ, Gole AM, Stone JW, Sisco PN, Alkilany AM, Goldsmith EC, Baxter SC (2008) Gold nanoparticles in biology: beyond toxicity to cellular imaging. Acc Chem Res 41 (12):1721-1730. doi:10.1021/ar800035u

4. Caswell KK, Wilson JN, Bunz UH, Murphy CJ (2003) Preferential end-to-end assembly of gold nanorods by biotin-streptavidin connectors. J Am Chem Soc 125 (46):13914-13915. doi:10.1021/ja037969i

5. Chang JY, Wu H, Chen H, Ling YC, Tan W (2005) Oriented assembly of Au nanorods using biorecognition system. Chem Commun (Camb) (8):1092-1094. doi:10.1039/b414059a

6. Park HS, Agarwal A, Kotov NA, Lavrentovich OD (2008) Controllable side-by-side and end-to-end assembly of Au nanorods by lyotropic chromonic materials. Langmuir 24 (24):13833-13837. doi:10.1021/la803363m

10.1021/la803363m [pii]

7. El-Sayed MA (2001) Some interesting properties of metals confined in time and nanometer space of different shapes. Acc Chem Res 34 (4):257-264. doi:ar960016n [pii]

8. Creighton JA, Eadon DG (1991) ULTRAVIOLET VISIBLE ABSORPTION-SPECTRA OF THE COLLOIDAL METALLIC ELEMENTS. J Chem Soc-Faraday Trans 87 (24):3881-3891

9. Foss CA, Hornyak GL, Stockert JA, Martin CR (1994) Template-Synthesized Nanoscopic Gold Particles - Optical-Spectra and the Effects of Particle-Size and Shape. Journal of Physical Chemistry 98 (11):2963-2971

10. Orendorff CJ, Gearheart L, Jana NR, Murphy CJ (2006) Aspect ratio dependence on surface enhanced Raman scattering using silver and gold nanorod substrates. Physical Chemistry Chemical Physics 8 (1):165-170

11. Li X, Qian J, Jiang L, He SL (2009) Fluorescence quenching of quantum dots by gold nanorods and its application to DNA detection. Appl Phys Lett 94 (6):-

12. Liang GX, Pan HC, Li Y, Jiang LP, Zhang JR, Zhu JJ (2009) Near infrared sensing based on fluorescence resonance energy transfer between Mn:CdTe quantum dots and Au nanorods. Biosens Bioelectron 24 (12):3693-3697. doi:S0956-5663(09)00270-X [pii]

10.1016/j.bios.2009.05.008

13. Matsuda K, Ito Y, Kanemitsu Y (2008) Photoluminescence enhancement and quenching of single CdSe/ZnS nanocrystals on metal surfaces dominated by plasmon resonant energy transfer. Appl Phys Lett 92 (21):-

14. Alper J, Crespo M, Hamad-Schifferli K (2009) Release Mechanism of Octadecyl Rhodamine B Chloride from Au Nanorods by Ultrafast Laser Pulses. The Journal of Physical Chemistry C 113 (15):5967-5973. doi:10.1021/jp809646e

15. Wijaya A, Schaffer SB, Pallares IG, Hamad-Schifferli K (2008) Selective Release of Multiple DNA Oligonucleotides from Gold Nanorods. ACS Nano 3 (1):80-86. doi:10.1021/nn800702n

16. Huff TB, Tong L, Zhao Y, Hansen MN, Cheng J-X, Wei A (2007) Hyperthermic effects of gold nanorods on tumor cells. Nanomedicine 2 (1):125-132. doi:doi:10.2217/17435889.2.1.125

17. Singh M, Briones M, Ott G, O'Hagan D (2000) Cationic microparticles: A potent delivery system for DNA vaccines. Proc Natl Acad Sci U S A 97 (2):811-816

18. Peetla C, Labhasetwar V (2009) Effect of molecular structure of cationic surfactants on biophysical interactions of surfactant-modified nanoparticles with a model membrane and cellular uptake. Langmuir 25 (4):2369-2377. doi:10.1021/la803361y

10.1021/la803361y [pii]

19. Thorpe JF (1907) Reaction of certain colouring matters of the oxazine series. J Chem Soc 91:324-336

20. Greenspan P, Mayer EP, Fowler SD (1985) Nile Red - a Selective Fluorescent Stain for Intracellular Lipid Droplets. J Cell Biol 100 (3):965-973

21. Nakayama A, del Monte F, Hajjar RJ, Frangioni JV (2002) Functional near-infrared fluorescence imaging for cardiac surgery and targeted gene therapy. Mol Imaging 1 (4):365-377

22. Morrison SF (2004) Central pathways controlling brown adipose tissue thermogenesis. News Physiol Sci 19:67-74

23. Nakayama A, Bianco AC, Zhang CY, Lowell BB, Frangioni JV (2003) Quantitation of brown adipose tissue perfusion in transgenic mice using near-infrared fluorescence imaging. Mol Imaging 2 (1):37-49

24. Mouvet C, Harris RD, Maciag C, Luff BJ, Wilkinson JS, Piehler J, Brecht A, Gauglitz G, Abuknesha R, Ismail G (1997) Determination of simazine in water samples by waveguide surface plasmon resonance. Analytica Chimica Acta 338 (1-2):109-117

25. Bokken GC, Corbee RJ, van Knapen F, Bergwerff AA (2003) Immunochemical detection of Salmonella group B, D and E using an optical surface plasmon resonance biosensor. FEMS Microbiol Lett 222 (1):75-82. doi:S0378109703002507 [pii]

26. Karlsson R, Michaelsson A, Mattsson L (1991) Kinetic analysis of monoclonal antibody-antigen interactions with a new biosensor based analytical system. J Immunol Methods 145 (1-2):229-240

27. Mandine E, Gofflo D, Jean-Baptiste V, Sarubbi E, Touyer G, Deprez P, Lesuisse D (2001) Src homology-2 domain binding assays by scintillation proximity and surface plasmon resonance. J Mol Recognit 14 (4):254-260. doi:10.1002/jmr.542 [pii] 10.1002/jmr.542

28. Karlsson R, Stahlberg R (1995) Surface plasmon resonance detection and multispot sensing for direct monitoring of interactions involving low-molecular-weight analytes and for determination of low affinities. Anal Biochem 228 (2):274-280. doi:S0003-2697(85)71350-4 [pii]

10.1006/abio.1995.1350

29. Carrasco C, Rosu F, Gabelica V, Houssier C, De Pauw E, Garbay-Jaureguiberry C, Roques B, Wilson WD, Chaires JB, Waring MJ, Bailly C (2002) Tight binding of the antitumor drug ditercalinium to quadruplex DNA. Chembiochem 3 (12):1235-1241. doi:10.1002/1439-7633(20021202)3:12<1235::AID-CBIC1235>3.0.CO;2-I

30. Erb E-M, Chen X, Allen S, Roberts CJ, Tendler SJB, Davies MC, ForsÈn S (2000) Characterization of the Surfaces Generated by Liposome Binding to the Modified Dextran Matrix of a Surface Plasmon Resonance Sensor Chip. Analytical Biochemistry 280 (1):29-35

31. Lang H, Duschl C, Vogel H (2002) A new class of thiolipids for the attachment of lipid bilayers on gold surfaces. Langmuir 10 (1):197-210

32. Salamon Z, Wang Y, Tollin G, Macleod HA (1994) Assembly and molecular organization of self-assembled lipid bilayers on solid substrates monitored by surface plasmon resonance spectroscopy. Biochim Biophys Acta 1195 (2):267-275

33. Heyse S, Vogel H, Sanger M, Sigrist H (1995) Covalent attachment of functionalized lipid bilayers to planar waveguides for measuring protein binding to biomimetic membranes. Protein Sci 4 (12):2532-2544. doi:10.1002/pro.5560041210

34. Plant AL, Brigham-Burke M, Petrella EC, O'Shannessy DJ (1995) Phospholipid/alkanethiol bilayers for cell-surface receptor studies by surface plasmon resonance. Anal Biochem 226 (2):342-348. doi:S0003269785712341 [pii]

35. Ramsden JJ, Bachmanova GI, Archakov AI (1996) Immobilization of proteins to lipid bilayers. Biosens Bioelectron 11 (5):523-528. doi:0956566396867893 [pii]

36. Smith DK, Korgel BA (2008) The Importance of the CTAB Surfactant on the Colloidal Seed-Mediated Synthesis of Gold Nanorods. Langmuir 24 (3):644-649

37. Nikoobakht B, El-Sayed MA (2003) Preparation and growth mechanism of gold nanorods (NRs) using seed-mediated growth method. Chem Mater 15 (10):1957-1962

38. Li W, Han YC, Zhang JL, Wang BG (2005) Effect of ethanol on the aggregation properties of cetyltrimethylammonium bromide surfactant. Colloid J+ 67 (2):159-163

39. Oshannessy DJ, Brighamburke M, Soneson KK, Hensley P, Brooks I (1993) Determination of Rate and Equilibrium Binding Constants for Macromolecular Interactions Using Surface Plasmon Resonance: Use of Nonlinear Least Squares Analysis Methods. Analytical Biochemistry 212 (2):457-468

CHAPTER 4

SELENOCYSTEINE AS A pH DEPENDENT, HETEROBIFUNCTIONAL LINKER FOR PROTEIN CONJUGATION WITH SINGLE RESIDUE SELECTIVITY

Abstract:

We have developed a protein conjugation system that selectively functionalizes a protein through its C-terminus in a pH dependent manner, by fusing it to a self-splicing protein element known as an intein. This system is advantageous over non-specific functionalization systems such as EDC/NHS chemistry in that the linkage can occur at only one amino acid. The system uses selenocysteine (Sec) as both a cleavage-inducing agent for the intein and heterobifunctional linker. Maltose binding protein (MBP) fused to the *Mxe gyrase* A intein from *Saccharomyces cerevisiae* was expressed in *E. coli*. Sec was used to induce cleavage of MBP from the intein, in both lysate and while bound to a chitin chromatography column, leaving the Sec covalently bonded to MBP. MBP lysate and purified MBP were selectively labeled at pH 5 by reacting the selenocysteine tagged protein with maleimide labeled fluorescein and maleimide labeled nanoparticles. The system was further verified by expressing A33 single chain antibody (ScFv) in *Pichia pastoris* fused to the *Mxe gyrase* A intein with a C-terminal 6x-His tag. The ScFv was cleaved and tagged with the Sec then reacted with maleimide labeled fluorescein. The fluorescein functionalized ScFv successfully labeled SW1222 cancer cells as determined by FACS, demonstrating the efficacy of the system.

***Introduction**:*

Inteins are self-splicing protein elements that are very similar to introns in mRNA. They were originally discovered in *Saccharomyces cerevisiae*[1, 2] when two groups were studying the *VMA1* gene. The gene encodes a protein expected to be 118 kDa but instead produces a 69 kDa active product and a 50 kDa secondary protein. Through mRNA and protein sequence analysis, it was determined that the two outer catalytic domains (exteins) were spliced together post-translationally and the 50 kDa protein was spliced out (intein). Inteins splice themselves out through a multistep transesterification-succinimide release process that relies on a conserved cysteine and serine in the N and C exteins respectively.[3] The *Sce* VMA1 intein has been used extensively for biotechnology purposes since Chong et. al removed the conserved serine from the *Sce* VMA1, allowing cleavage to be induced *in vitro* by a reducing reagent such as DTT.[4] The system was adapted by New England Biolabs as a purification system, allowing users to purify proteins without having any permanent affinity tag or having to use a protease to cleave the tag.[5-8] Cleavage with DTT or 2-mercaptosulfonic acid (MESNA) also allows the protein to be functionalized through intein mediated protein ligation (IPL).[9, 10] The thioester created when MESNA liberates the protein from the intein can react with any cysteine to form a peptide bond, thus IPL allows the protein to be functionalized with peptides, protein, or any small molecule containing a cysteine or cysteine like moiety.

IPL has also been used to introduce selenocysteine into proteins by cleaving the protein of interest from the intein with a thiol and a selenocysteine labeled synthetic

peptide mixture, yielding the protein tagged with the selenocysteine labeled peptide.[11] Sec is a rare amino acid in mammals and is a desirable functional group *in vitro*. Sec is more nucleophilic than Cys and its pKa is only 5.2 while Cys has a pKa of 8.3.[12] This means that at relatively low pH values, Cys will be protonated while selenocysteine will still be reactive. Sec also has a much higher redox potential of -488 mV as compared to -233 mV of cysteine.[13] In addition to IPL, selenocysteine has been added to proteins through a variety of chemical and recombinant methods. Serine residues have been converted to Sec chemically[14] through activation with PMSF and hydrogen selenide. Selenocysteine labeled antibodies have been produced recombinantly in mammalian cell lines by engineering in the Sec Insertion Element (SECIS) into the 3' UTR, which suppresses the UGA stop codon and allows Sec insertion.[15, 16] The SECIS element functions by forming secondary structure in the mRNA, which recruits *cis* and *trans* acting elements to insert Sec.[17] Selenocysteine containing proteins have also been expressed in *E. coli* using an engineered SECIS element, a selenite substrate, and co-expression of the *selA*, *selB*, and *selC* genes which encode the selenocysteine synthase, the translation elongation factor SELB, and the $tRNA^{Sec}$ respectively. The system produced an enzyme with 25% of the native enzyme's specific activity with a yield of 20 mg/L of culture.[18] A similar approach was used to produce glutathione *S*-transferase in *E. coli* internally labeled with selenocysteine at a yield of 2.9 mg/L of culture.[19]

We present an amino acid specific, *in vitro* approach to label proteins with Sec by using the nucleophilicity of free Sec to cleave the target protein from an intein tag and simultaneously label the protein with Sec at its C-terminus. The protein can then be

further functionalized by combining it with any reactive functional group, such as a maleimide labeled fluorophore or surface (Figure 4-1). Conjugation only occurs at the Sec residue by using thiol and Se^- reactive linkers and titrating the pH such that only Sec is charged by taking advantage of its low pKa. This system is advantageous over *in vivo* systems in that it does not rely upon stop codon suppression, where many peptides are cut short instead of including the Sec amino acid. The system is also advantageous over synthetic and semi-synthetic methods in that selenium or Sec containing peptides do not have to be synthesized at considerable expense. Here we demonstrate cleavage of MBP-intein fusions by Sec, Sec dependent functionalization of MBP with maleimide labeled fluorescein in bacterial lysate and purified Sec-MBP, and functionalization of maleimide labeled nanoparticles. We additionally demonstrate the scope of the system by using Sec to purify a His tagged, A33 ScFv-Intein fusion and subsequently label it with fluorescein. The labeled antibody was then used for FACS with cells bearing the A33 cancer antigen and performed almost as well as a commercially available antibody. This system provides an easy way to purify, label, and conjugate proteins in an amino acid specific fashion.

Materials and Methods:

Expression of MBP-Intein-CBD:

The plasmid pMXB10, a derivative of pTXB1, was obtained from New England Biolabs (Ipswich, MA). It contains maltose binding protein fused to the *Mxe A* intein

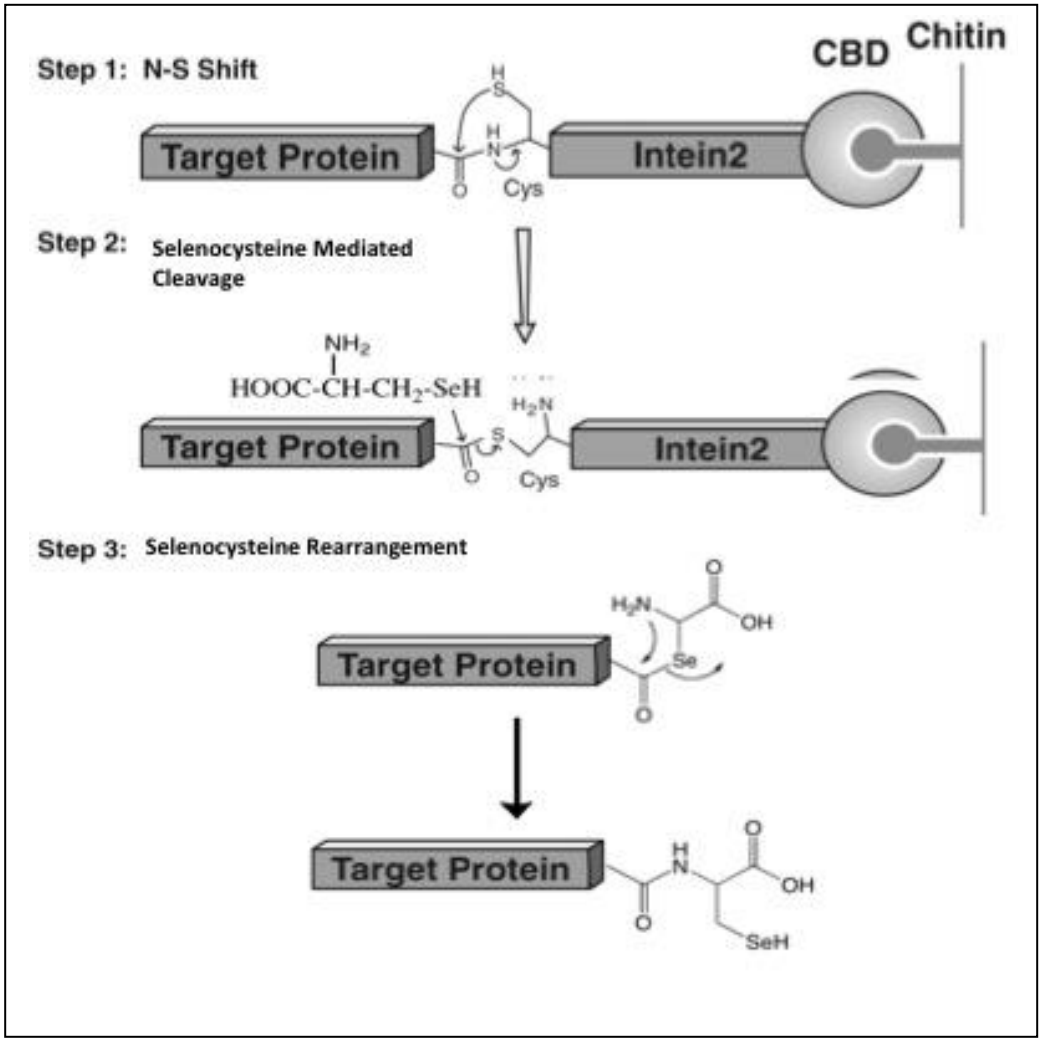

Figure 4-1. Selenocysteine Mediated Intein Cleavage Mechanism. N-terminal cysteine of the intein undergoes a N-S acyl shift making the carbonyl carbon very electropositive. In this arrangement, selenocysteine attacks the carbonyl carbon and cleaves the target protein-intein peptide bond. The target protein with the attached selenocysteine undergoes another rearrangement such that the Se moves to the side chain position, leaving it free to react. Figure adapted from New England Biolabs.

and a chitin binding domain (CBD) under control of the T7 promoter. The plasmid was transformed into BL21(DE3) *E. coli* cells and selected with ampicillin. A transformed colony was picked and inoculated into a 5 ml LB-Amp culture that was subsequently incubated overnight at 37°C. 200 µl of the overnight culture was inoculated into 20 ml of LB-Amp in a baffled flask and was shaken at 37°C until an OD_{600} of 0.6 was reached. Expression was induced with 0.35 mM IPTG for 3 hours after which time the cells were chemically lysed and the soluble fraction collected. Lysate was stored at 4°C. The lysate was resolved on a Bio-Rad (Hercules, CA) "Any kD" SDS-PAGE gel that was stained with Invitrogen SimplyBlue Safe Stain (Carlsbad, CA). An identical gel was transferred to nitrocellulose and a western blot was performed using HRP conjugated anti-MBP. Protein concentration was determined by Bradford Assay reagent as per the manufacturer's directions ("Sigma-Aldrich" St. Louis, MA).

MBP-Intein cleavage & Fluorescent Labeling from Bacterial Lysate:

L-selenocystine (Sigma Aldrich, St. Louis, MO) was reduced to L-selenocysteine and intein cleavage was induced by allowing 80 µl ethanol, 160 µl TCEP (50 mM), 320 µl pH 5 sodium citrate buffer (20 mM), 1.6 mg selenocystine and 60 µl MBP lysate (~5 mg/ml) to mix in a small glass vile for two hours. The L-selenocystine lost its yellow color upon reduction. To this solution, approximately 0.5 mg of fluorscein-5-maleimide (Thermo-Fisher, Rockford IL) was dissolved and allowed to shake via rocker for two hours in the dark at room temperature. The non-selenocysteine control was reacted in the same manner as the successful conjugation but the buffer system

contained 80 µl ethanol, 50 µl 100 mM MESNA, 320 µl pH 5 sodium citrate buffer (20 mM), and 60 µl MBP lysate (~5 mg/ml). After conjugation, the protein was resolved on two Bio-Rad "Any kD" SDS-PAGE gels. One was stained with Invitrogen SimplyBlue Safe Stain while the other was imaged fluorescently with a Bio-Rad GelDoc system under UV excitation. Labeling efficiency was calculated as per the manufacturer's protocol for fluorscein-5-maleimide.

MBP- Intein cleavage & Fluorescent Labeling from Purified MBP:

Chitin beads were obtained from New England Biolabs and packed at 1 ml/min into a C10-10 column (GE Healthcare, Piscataway, NJ) to a bed height of approximately 3 cm using an Akta Explorer (GE Healthcare, Piscataway, NJ) run by Unicorn Software (GE Healthcare, Piscataway, NJ). MBP-Intein-CBD lysate was diluted to 1.5 mg/ml with 25 mM pH 7 sodium phosphate buffer. 6 ml of the diluted lysate was loaded at 0.4 ml/min. The column was then washed with 3 column volumes of the 25 mM citrate buffer at pH 5 at 0.5 ml/min. A selenocysteine solution containing 1.6 ml ethanol, 6.4 ml pH 5 citrate buffer (25 mM), 16mg Se-Se, 1 ml TCEP (50 mM) was prepared and allowed to stir for 2 hours. After stirring, one column volume of this solution was added to column and allowed to sit for one hour, after which the solution was eluted off the column and collected. 0.5 mg of fluorscein-5-maleimide was added to the eluted solution and was rocked in the dark, at room temperature for two hours. 0.5 mg of fluorscein-5-maleimide and 0.5 ml of elution buffer were added to 2 ml of wash fraction and rocked for one hour in the dark. Finally, 0.5 mg of fluorscein-5-maleimide was added to 2 ml of the wash fraction and rocked in the dark for 1 hour

without adding selenocysteine. The solutions were then resolved by SDS-PAGE and imaged fluorescently in a manner identical to the lysate. Total protein concentrations for all fractions were determined by Bradford assay.

MBP Labeling of Gold Nanoparticles:

0.8 nm “Undecagold” nanoparticles functionalized with maleimide were obtained from Nanoprobes Inc. (Yaphank, NY) and were re-suspended in 1 ml of ultra-pure water from its lyophilized state. Purified MBP bound to Sec was prepared as described in the previous section, without adding fluorescein. A second batch of purified MBP was also prepared using 10 mM MESNA supplemented with 5 mM NaOH in 25 mM citrate buffer (pH 5) to elute the protein from the column instead of Sec. After elution the preparation was titrated to pH 5. Four solutions were prepared in 1.6 ml centrifuge tubes containing (1) 50 µl Sec Eluted MBP, 200 µl Ultrapure Water (2) 200 µl Mal.-Nanoparticles, 50 µl Ultrapure Water (3) 200 µl Mal.-Nanoparticles, 50 µl Sec eluted MBP (4) 200 µl Mal.-Nanoparticles, 50 µl MESNA eluted MBP. All four solutions were rocked for two hours in the dark. At the end of the particle incubation, nitrocellulose was incubated in a 1:1:8 - NuPage Transfer Buffer (Invitrogen, Carlsbad, CA):methanol:water solution for 10 minutes after which time the excess solution was removed while keeping the membrane slightly damp. 5 µl of each solution was spotted onto a separate spot on the activated nitrocellulose and allowed to bind for 30 minutes then aspirated off. The blot was briefly washed with blocking buffer and an image was taken at this point. A western blot procedure was then performed using the WesternBreeze Chromogenic Immunodetection Kit (Invitrogen,

Carlsbad, CA) using Anti-MBP-HRP as the primary antibody. After development of the western blot, a second image was taken.

Production of A33 ScFv-Intein-His:

The amino acid sequence for the single chain antibody against the A33 cancer antigen was obtained from previous work by our group.[20] This sequence was fused in frame with the amino acid sequence for the Mxe mini-intein and a 6x-His tag was added to the C-terminus.[21] It is important to note that the efficiency of intein cleavage is highly dependent upon the amino acid immediately upstream of the intein, and an alanine or other readily cleavable amino acid should be inserted if the last amino acid in the target protein is problematic, such as a proline.[21] This sequence was then codon optimized for expression in the methanotropic yeast *Pichia pastoris* and synthesized by Genscript Technologies Inc (Piscataway, NJ). The construct was then subcloned into the pPiczαA *P. pastoris* expression vector and transformed into a GS115 *P. pastoris* strain under Zeocin selection. Transformants were picked and grown for 72 hours at room temperature while shaking in 50 ml of MMHA medium.[22] 0.25% (v/v) methanol was added every 12 hours as the cell's only carbon source at which time intracellular and supernatant samples were collected.

Purification and Conjugation of A33 ScFv-Intein-His for FACS:

After 72 hours of growth, the *P. pastoris* cells were pelleted by centrifugation and were re-suspended in breaking buffer and lysed as previously described.(26) The *Pichia* lysate was then clarified by centrifugation at 14000 g and the supernatant

collected. 25 ml of the lysate was then loaded onto a 5 ml HisTrap FF Column (GE Healthcare BioSciences, Uppsala Sweden) at 2 ml/min. The column was then washed with 3 CVs of 25 mM sodium phosphate buffer at pH 7.4. The bound A33 was then eluted by intein cleavage with Sec elution buffer as described above and was stored at 4°C. After elution, the column was regenerated by washing with 1 CV of 0.1 M EDTA followed by a rinse with 5 CVs ultrapure water. The column was then recharged with 5 CV of 0.1 M nickel sulfate and rinsed with 10 CV of ultrapure water. A second batch of lysate was loaded onto the column and washed as described. It was then eluted with 1 CV of 0.5 M Imidazole in 25 mM citrate buffer so as to elute the whole construct without inducing intein cleavage. After elution, the pH of both fractions was adjusted to pH 5.

Fluorescence Activated Cell Sorting Assay:

For use in FACS, SW1222 human colorectal cells were grown in GIBCO minimum essential medium supplemented with fetal bovine serum, L-Glutamine, Penicillin, and streptomycin. The adherent cells were trypsinized, pelleted and resuspended at 10 million cells/ml. 100 µl of cell suspension was added to 4 separate tubes. The cells in the first tube were labeled with rabbit Anti-A33 monoclonal antibody (Santa Cruz Biotechnology, Santa Cruz, CA) then goat anti-rabbit IgG-FITC secondary antibody as per the manufacturer's recommendations for FACS. The second tube of cells was treated with approximately 1 µg of Sec eluted A33 ScFv and 0.5 mg of fluroscein-5-malimide. A third tube of cells was treated with approximately 1 µg of imidazole eluted A33 ScFv and 0.5 mg of fluroscein-5-malimide. A fourth tube contained 100 µl

of untreated cells. Both A33 treated tubes were allowed to react 1 hour on ice after which the excess antibody and fluorophore were removed by two wash and centrifugation cycles. All four cell treatments were tested using fluorescence-activated cell sorting on a Beckman Coulter flow cytometer using standard procedures in triplicate.

Results and Discussion

MBP-Intein-CBD Expression:

A MBP-intein-CBD fusion was expressed in BL21(DE3) *E. coli* and used as a model for selenocysteine mediated intein cleavage and functionalization of proteins. The soluble fraction of the induced, clarified lysate had a total protein concentration of 5.61 mg/ml as determined by Bradford assay. Expression of the MBP-Intein fusion was successful, as determined by Coomassie stained SDS-PAGE (Figure 4-2A). The induced, insoluble fraction of the induced lysate may be seen in Lane 1 of Figure 4-2A. A strong band at 72 kDa indicates expression of the full MBP-intein-CBD and a weak band at 41 kDa indicates some autocatalytic cleavage of the intein. Since the protein was found within the insoluble fraction it means that some of the recombinant protein was driven into inclusion bodies during overexpression and was not readily available for use. Lane 2 of Figure 4-2A shows the soluble, induced expression fraction. Another strong band at 72 kDa indicates full construct expression with a weaker cleaved band appearing again at 41 kDa. It is not surprising the auto-cleaved band is stronger in the soluble fraction, as it is more available for cleavage than in inclusion bodies where it is relatively protected. Lane 3 is the un-induced insoluble

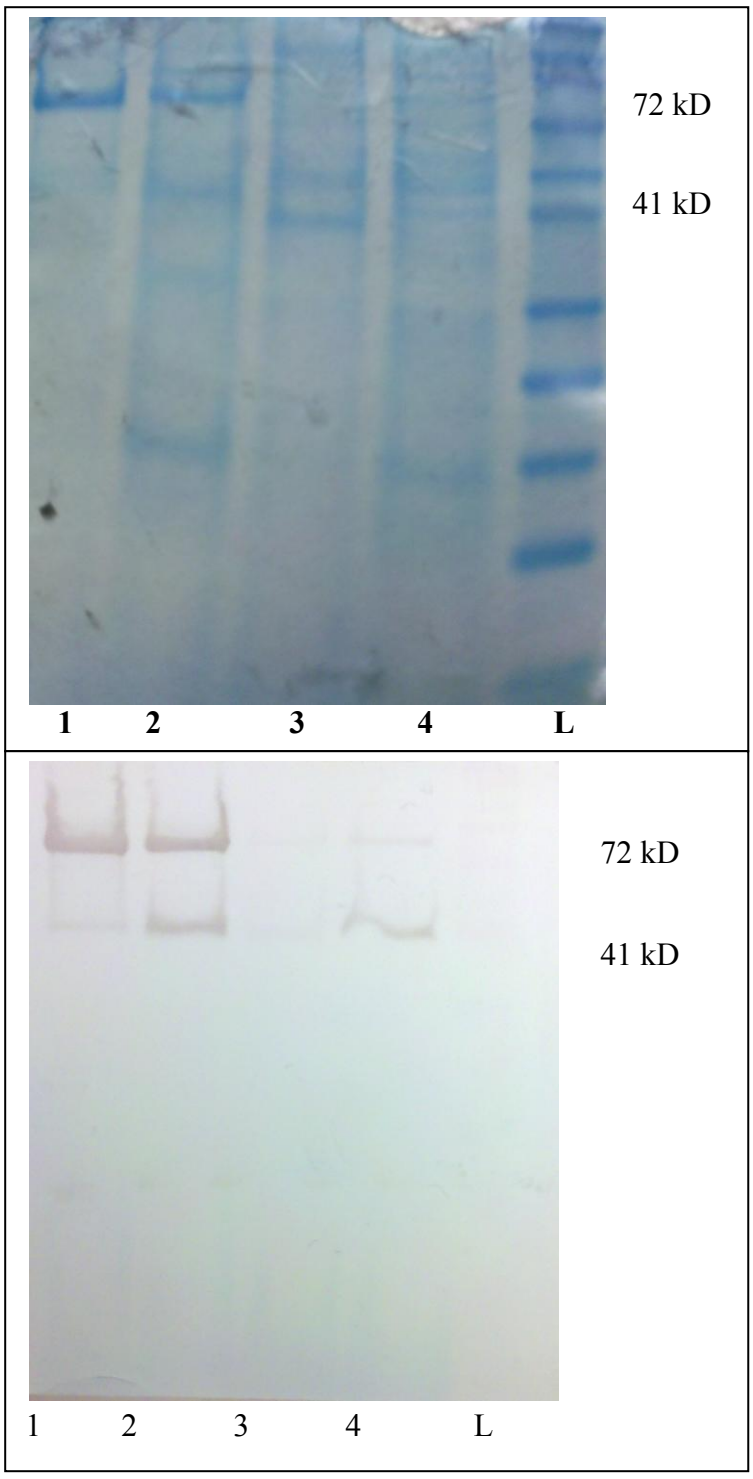

Figure 4-2. Expression of MBP-Intein-CBD fusion in BL21(DE3) *Escherichia coli*. Lanes 1-4 correspond to induced insoluble, induced soluble, uninduced insoluble, and uninduced soluble fractions respectively. L denotes ladder. A) Coomassie stained SDS-PAGE gel. B) Western Blot of SDS-PAGE gel using anti-MBP HRP.

fraction. No MBP bands are easily seen, indicating there is almost no MBP present in the uninduced, insoluble fraction, which is expected. No MBP can be easily identified in lane four which corresponds to the un-induced soluble fraction. Identity of the MBP fusion construct was confirmed with an anti-MBP western blot (Figure 4-2B). Lanes in Figure 4-2B correspond directly to lanes in Figure 4-2A. The more sensitive western blot detected some expression in both uninduced fraction, indicating some leaky expression from the T7 promoter.

Selenocysteine Cleavage & Labeling of MBP-Intein-CBD from Lysate:

After establishing expression of the MBP-Intein-CBD fusion, selenocysteine was tested to determine its ability to induce intein cleavage and subsequently label MBP with maleimide conjugated fluorescein. The Coomassie stained SDS-PAGE gel in Figure 4-3A shows intein cleavage from the fusion protein lysate while the fluorescent image in Figure 4-3B demonstrates pH and selenocysteine dependency of the labeling system. Lane 1 in Figure 4-3A is a control reaction of MBP-Intein-CBD lysate, treated with 2-mercaptosulfonic acid (MESNA) in pH 5 citrate buffer with a small amount of base, without selenocysteine. This was designed to induce cleavage at a higher pH then be titrated to pH 5 with prior to exposure to maleimide-fluorescein. By inducing cleavage without selenocysteine then titrating the reaction to pH 5, it demonstrates the pH selectivity of the system. At pH 5 the thiol in the MESNA tag is protonated and therefore unable to react with the maleimide labeled fluorescein, as seen from the lack of fluorescent band in Lane 1 of Figure 4-3B. The Sec cleavage reaction in pH 5 citrate buffer is show in Lane 2 of Figure 4-3A. The cleavage of the MBP-Intein

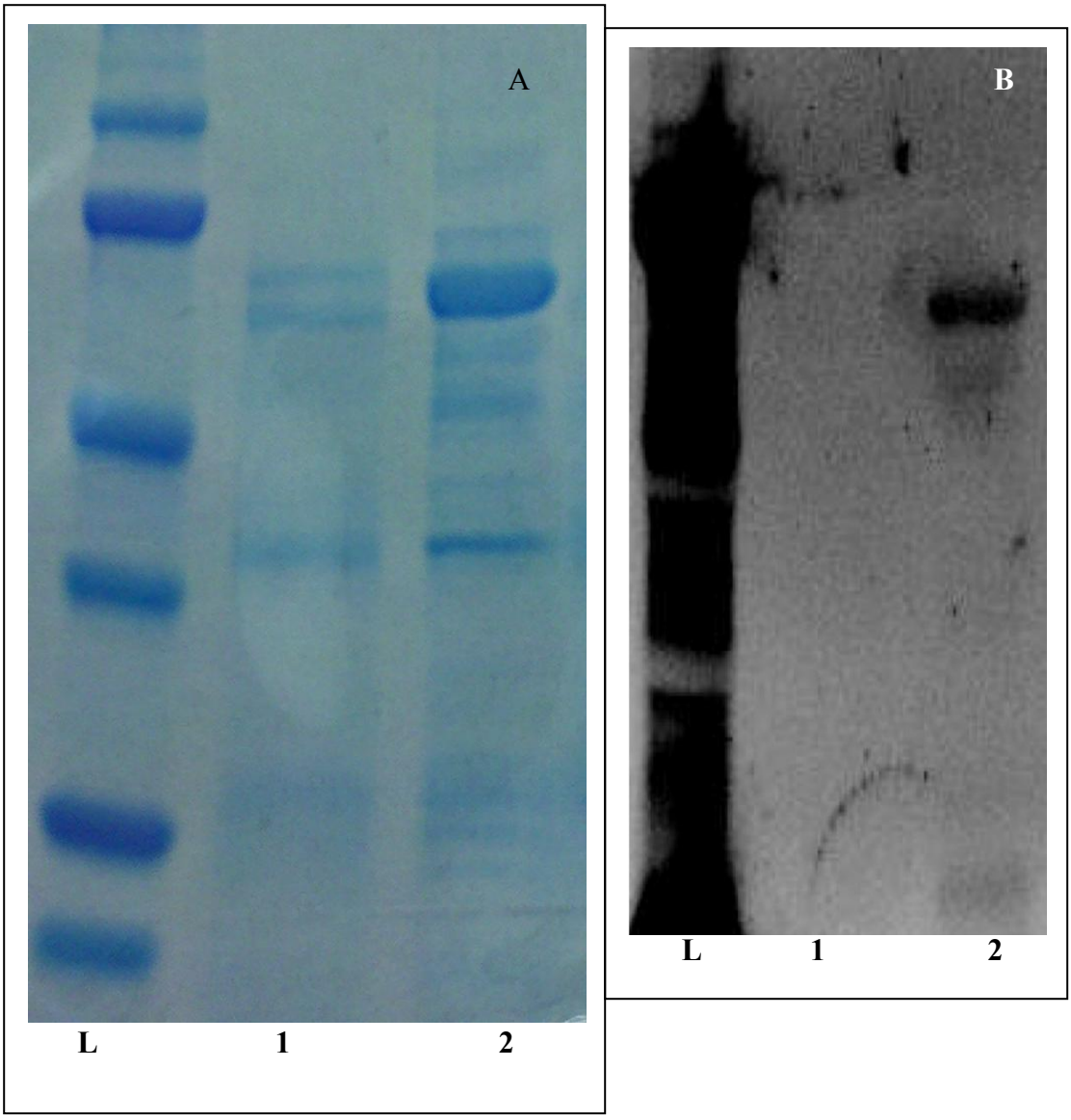

Figure 4-3 Labeling of MBP-Intein-CBD bacterial lysate with Fluorescein-5-Malimide. A) Coomassie stained SDS-PAGE gel of MBP *E. coli* lysate. B) Fluorescent image of SDS-PAGE gel of MBP *E. coli* lysate after being reacted with Fluorescein-5-Maleimide. L denotes ladder. Lane 1 contains MESNA treated lysate as a positive cleavage control. Lane 2 is selenocysteine cleaved protein. Images A & B are identical but not shown at the same scale.

clearly seen with a strong band at 41 kDa, and a very faint band at 72 kDa. Cleavage efficiency was calculated to be 95% by gel densitometry. In Lane 2 of Figure 4-3B, a strong fluorescent band is seen at 41 kDa indicating labeling of the MBP with maleimide-fluorescein through the Sec linker. A small degree of non-specific labeling is seen for other lysate proteins that may be degradation products or incomplete titration of cysteine groups. After removal of excess fluorescein by spin column, the labeling efficiency of fluorscein-5-maleimide to the cleaved MBP was calculated to be 87%.

Column Purification and Labeling of MBP-Intein-CBD:

The MBP-intein-CBD fusion was purified from a chitin column using selenocysteine as both cleavage and linking agent. After packing, approximately 9 mg of MBP lysate was loaded on a 3 ml chitin affinity column via FPLC. A 3 CV wash was performed and the fraction was collected containing about 6 mg of total protein. Activated Sec was then used to cleave the MBP from the intein and elute it off the column yielding approximately 1.5 mg purified MBP, after which it was conjugated to maleimide-fluorescein. Lane 1 of Figure 4-4 shows the fluorescent image of the Sec elution fraction. Not surprisingly, only the MBP band shows fluorescence in the purified fraction. Lane 2 of Figure 4-4 shows the fluorescent labeling of the wash fraction. Fluorescent labeling was achieved by adding Sec then fluorescein to the wash fraction to determine how much MBP was lost in the wash step. Significant MBP loss in the wash mostly occurred due to overloading the chitin beads and the relatively low pH of the wash buffer interfering the column's affinity. Lane 3 of Figure 4-4 shows the wash

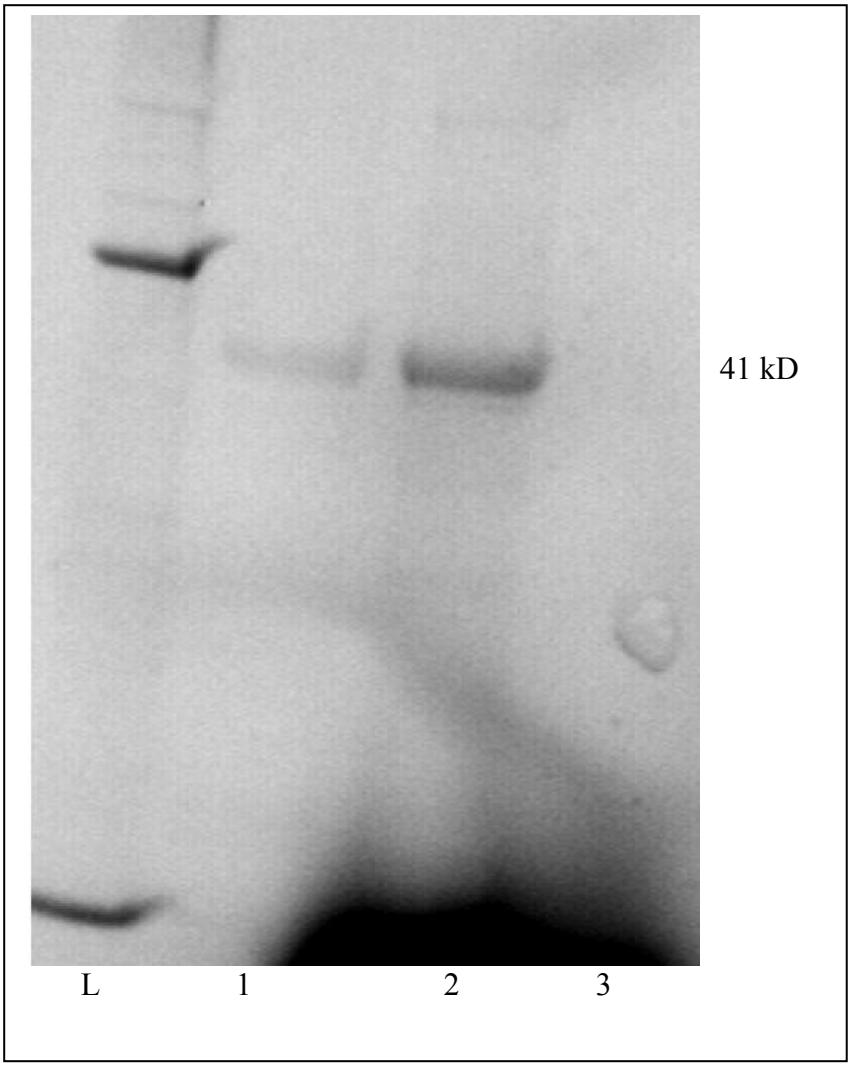

Figure 4-4. Fluorescent image of affinity purified MBP-Sec with Fluorescein-5-Maleimide labeling. L denotes ladder. Lane 1 contains the Sec eluted fraction exposed to Fluorescein-5-Maleimide. Lane 2 contains the wash fraction which was exposed to Sec and fluorescein to determine protein loss. Lane 3 contains the wash fractions exposed to Fluorescein-5-Maleimide without Sec.

fraction exposed to fluorescein without Sec. No labeling occurs, as expected, and demonstrates the Sec dependency of the labeling process.

MBP Labeling of Maleimide-Gold Nanoparticles:

In order to demonstrate the system's compatibility with labeling nanoparticles and other surfaces, maleimide functionalized 0.8 nm nanoparticles were obtained commercially and labeled with MBP-Sec. Purified MBP-Sec was obtained from a chitin column as described and incubated with the maleimide labeled gold nanoparticles to form permanent, covalently linked conjugates. Samples containing MBP-Sec alone, nanoparticles alone, and MESNA eluted MBP with particles at pH 5, and Sec eluted MBP and particles were prepared and individually spotted on activated nitrocellulose then aspirated off after hybridization, as seen in Figure 4-5A. As expected a yellow spot indicative of nanoparticles is observed in spots 2-4, all of which contained nanoparticles. Figure 4-5B illustrates the same nitrocellulose after a western blotting procedure with Anti-MBP-HRP. Spot 1 which contained the MBP only positive control blots positive, as expected. Spot 2 contained the particle only control and does not develop, as expected. Spot 3 which contained the Sec eluted MBP at pH 5 and maleimide particles developed positively, indicating successful conjugation to the nanoparticles. The fourth spot which contained MESNA eluted MBP at pH 5 did not develop. This is expected, as MESNA is not able to conjugate to the maleimide at pH 5 since its thiol is protonated. Unbound MBP is not seen in spot 4 because of nanoparticle exclusion of the protein from the blot and the short

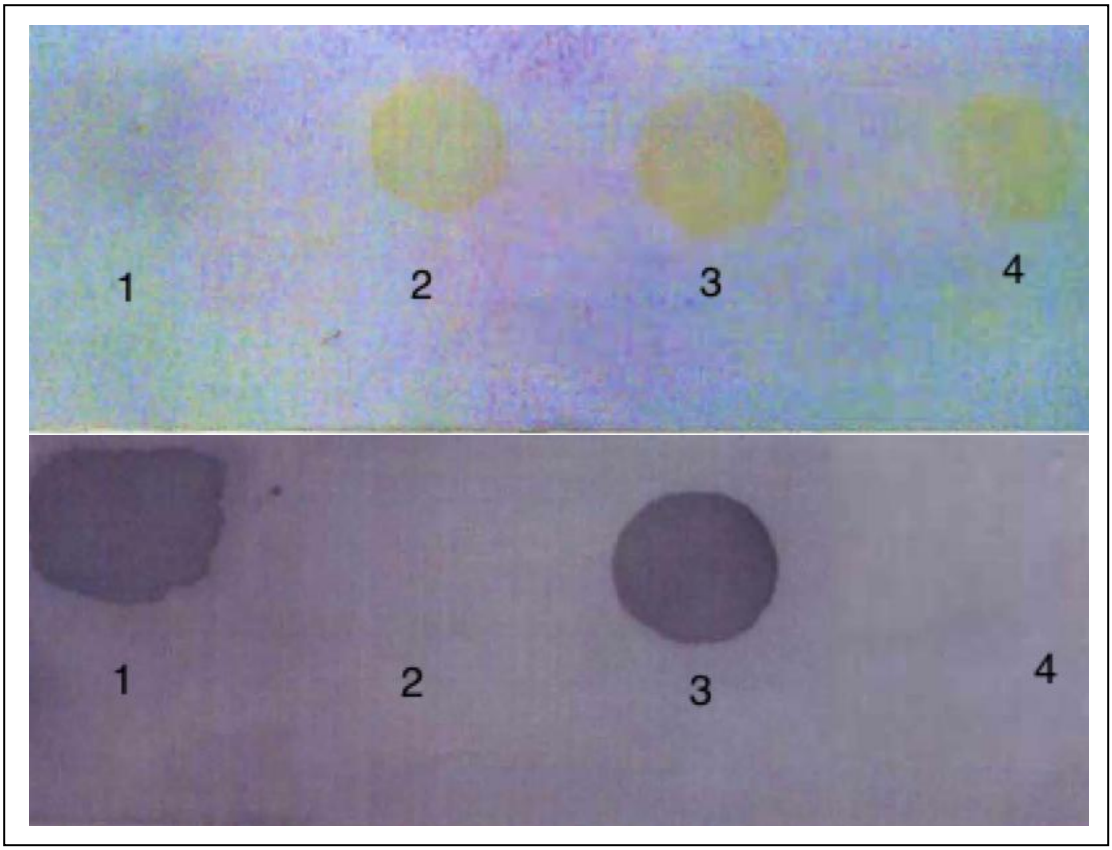

Figure 4-5. MBP Labeling of Maleimide-Gold Nanoparticles. Spots 1-4 contain MBP, nanoparticles, nanoparticles and Sec eluted MBP at pH 5, and nanoparticles and MESNA eluted MBP at pH 5 respectively.

development time of the western blot since spots 1 and 3 contained large amount of MBP and developed almost instantly.

While maleimide labeled particles were used to establish a permanently bonded MBP-particle conjugate, selenide could also bond directly to 60 nm gold particles. The ability of selenide to bond to gold and silver is well established.[23] The selenide bond is more stable and ~ 0.25 eV stronger than the corresponding thiol bond, though Se establishes lower surface coverage due to higher tilt angle of the conjugate.[23]

Production of A33-ScFv-Intein in *Pichia pastoris* & Maleimide-Fluorescein Labeling for FACS

MBP was used as a model to establish Sec as an intein cleavage and pH selective linking agent. After the system was developed, it was used to conjugate maleimide-fluorescein to a humanized single chain antibody against the A33 cancer antigen (A33ScFv) [22] which was then used for fluorescence activated cell sorting. A synthetic DNA construct, codon optimized for *Pichia pastoris*, was produced containing the A33 single chain antibody fused in-frame to the Mxe intein and a 6x-His tag added to the C-terminus. The construct was sub-cloned into the *P. pastoris* expression vector pPiczαA and transformed into the GS115 *P. pastoris* strain. While *Pichia* has been shown to secrete the A33 ScFv[22] and many other recombinant proteins[24, 25], the A33ScFv-Intein-His construct did not secrete. Expression was induced under a variety of temperatures and in GS115 strains containing foldases such as BIP and PDI[26], but

the construct still did not secrete. Due to the lack of secretion, *P. pastoris* expressing the fusion protein intracellularly was lysed and the ScFv construct was purified by immobilized metal affinity chromatography, eluting one preparation with Sec by intein cleavage and a second with imidazole for use as an uncleaved control.

Figure 4-6 demonstrates successful fluorescein labeling of the ScFv construct by FACS. Figure 4-6A compares unlabeled SW1222 cells which bear the A33 cancer antigen, to a positive control containing SW1222 cells labeled by commercially available monoclonal antibody bound by a fluorescein labeled secondary antibody. Fifty-three percent of the cell population was labeled with the fluorescent control. The relatively low percentage of labeling is not surprising for SW1222 cells as they secrete a significant amount of extracellular matrix and tend to aggregate, inhibiting labeling. Figure 4-6B shows cell labeling by Sec cleaved A33 that was labeled with maleimide-fluorescein. The fluorescently tagged ScFv labeled 49 percent of the SW1222 cell population (filled red block) as compared to unlabelled cells (unfilled black outine). This indicates the system was successful, as the ScFv had a labeling efficiency almost as high as the commercially available monoclonal antibody. Figure 4-6C demonstrates the Sec dependence of the labeling reaction. The uncleaved A33ScFv-Intein-His construct was eluted from the IMAC chromatography column using imidazole. It was then exposed to maleimide-fluorescein prior to labeling SW1222 cells. In this control only 11 percent of the cell population

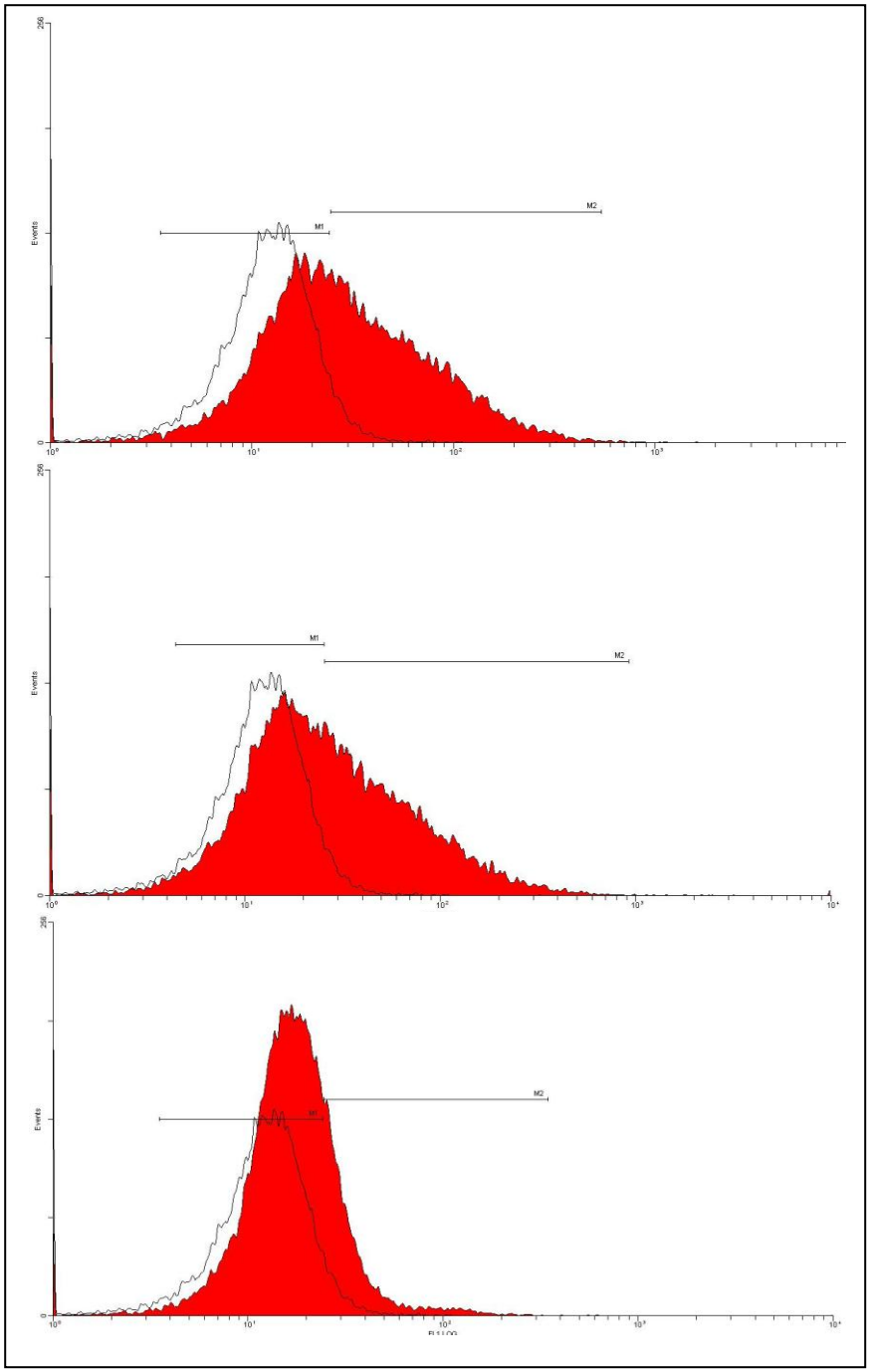

Figure 4-6. Fluorescence Activated Cell Sorting of SW1222 Cancer Cells labeled with Sec-Fluorescein-5-Maleimide functionalized A33 single chain antibody. Unfilled black outlines correspond to the unlabeled cell populations. The red, filled groups correspond to the labeled cell populations. A) Fluorescein labeled monoclonal Ab positive control B) Maleimide-fluorescein labeled ScFv C) ScFv exposed to maleimide-fluorescein without Sec.

was labeled positively as compared to the negative control. The 11% false positive labeling most likely stems from incomplete titration of cysteine residues present in the single chain.

Conclusions:

We have demonstrated a straightforward system for protein conjugation in a pH dependent, amino acid specific manner. We have shown the system's ability to selectively label proteins from lysate, elute and label a protein from an affinity column while cleaving the protein from the affinity tagged intein, and have demonstrated the system's ability to functionalize nanoparticles and maleimide labeled surfaces. Furthermore, we have demonstrated its ability to label a single chain antibody that was subsequently used for FACS. This system provides a direct means to label or conjugate proteins and introduces selenocysteine into the construct which is highly desirable for the chemical and biotechnological properties.

References:

(1) Hirata, R., Ohsumk, Y., Nakano, A., Kawasaki, H., Suzuki, K., and Anraku, Y. (1990) Molecular structure of a gene, VMA1, encoding the catalytic subunit of H(+)-translocating adenosine triphosphatase from vacuolar membranes of Saccharomyces cerevisiae. *J Biol Chem 265*, 6726-33.

(2) Kane, P. M., Yamashiro, C. T., Wolczyk, D. F., Neff, N., Goebl, M., and Stevens, T. H. (1990) Protein splicing converts the yeast TFP1 gene product to the 69-kD subunit of the vacuolar H(+)-adenosine triphosphatase. *Science 250*, 651-7.

(3) Klabunde, T., Sharma, S., Telenti, A., Jacobs, W. R., Jr., and Sacchettini, J. C. (1998) Crystal structure of GyrA intein from Mycobacterium xenopi reveals structural basis of protein splicing. *Nat Struct Biol 5*, 31-6.

(4) Chong, S., Mersha, F. B., Comb, D. G., Scott, M. E., Landry, D., Vence, L. M., Perler, F. B., Benner, J., Kucera, R. B., Hirvonen, C. A., Pelletier, J. J., Paulus, H., and Xu, M. Q. (1997) Single-column purification of free recombinant proteins using a self-cleavable affinity tag derived from a protein splicing element. *Gene 192*, 271-81.

(5) Fong, B. A., and Wood, D. W. Expression and purification of ELP-intein-tagged target proteins in high cell density E. coli fermentation. *Microb Cell Fact 9*, 77.

(6) Hong, I., Kim, Y. S., and Choi, S. G. Simple purification of human antimicrobial peptide dermcidin (MDCD-1L) by intein-mediated expression in E.coli. *J Microbiol Biotechnol 20*, 350-5.

(7) Lu, W., Sun, Z., Tang, Y., Chen, J., Tang, F., Zhang, J., and Liu, J. N. Split intein facilitated tag affinity purification for recombinant proteins with controllable tag removal by inducible auto-cleavage. *J Chromatogr A 1218*, 2553-2560.

(8) Wu, W. Y., Miller, K. D., Coolbaugh, M., and Wood, D. W. Intein-mediated one-step purification of Escherichia coli secreted human antibody fragments. *Protein Expr Purif 76*, 221-8.

(9) Ghosh, I., Considine, N., Maunus, E., Sun, L., Zhang, A., Buswell, J., Evans, T. C., Jr., and Xu, M. Q. Site-specific protein labeling by intein-mediated protein ligation. *Methods Mol Biol 705*, 87-107.

(10) Severinov, K., and Muir, T. W. (1998) Expressed protein ligation, a novel method for studying protein-protein interactions in transcription. *J Biol Chem 273*, 16205-9.

(11) Eckenroth, B., Harris, K., Turanov, A. A., Gladyshev, V. N., Raines, R. T., and Hondal, R. J. (2006) Semisynthesis and characterization of mammalian thioredoxin reductase. *Biochemistry 45*, 5158-70.

(12) Huber, R. E., and Criddle, R. S. (1967) Comparison of the chemical properties of selenocysteine and selenocystine with their sulfur analogs. *Arch Biochem Biophys 122*, 164-73.

(13) Jacob, C., Giles, G. I., Giles, N. M., and Sies, H. (2003) Sulfur and selenium: the role of oxidation state in protein structure and function. *Angew Chem Int Ed Engl 42*, 4742-58.

(14) Luo, G. M., Zhu, Z. Q., Ding, L., Gao, G., Sun, Q. A., Liu, Z., Yang, T. S., and

Shen, J. C. (1994) Generation of selenium-containing abzyme by using chemical mutation. *Biochem Biophys Res Commun 198*, 1240-7.

(15) Hofer, T., Skeffington, L. R., Chapman, C. M., and Rader, C. (2009) Molecularly defined antibody conjugation through a selenocysteine interface. *Biochemistry 48*, 12047-57.

(16) Hofer, T., Thomas, J. D., Burke, T. R., Jr., and Rader, C. (2008) An engineered selenocysteine defines a unique class of antibody derivatives. *Proc Natl Acad Sci U S A 105*, 12451-6.

(17) Hatfield, D. L., and Gladyshev, V. N. (2002) How Selenium Has Altered Our Understanding of the Genetic Code. *Mol. Cell. Biol. 22*, 3565-3576.

(18) Arner, E. S., Sarioglu, H., Lottspeich, F., Holmgren, A., and Bock, A. (1999) High-level expression in Escherichia coli of selenocysteine-containing rat thioredoxin reductase utilizing gene fusions with engineered bacterial-type SECIS elements and co-expression with the selA, selB and selC genes. *J Mol Biol 292*, 1003-16.

(19) Jiang, Z., ArnÈr, E. S. J., Mu, Y., Johansson, L., Shi, J., Zhao, S., Liu, S., Wang, R., Zhang, T., Yan, G., Liu, J., Shen, J., and Luo, G. (2004) Expression of selenocysteine-containing glutathione S-transferase in Escherichia coli. *Biochemical and Biophysical Research Communications 321*, 94-101.

(20) Pla, I. A., Damasceno, L. M., Vannelli, T., Ritter, G., Batt, C. A., and Shuler, M. L. (2006) Evaluation of Mut+ and MutS Pichia pastoris phenotypes for high level extracellular scFv expression under feedback control of the methanol concentration. *Biotechnol Prog 22*, 881-8.

(21) (2011), New England Biolabs.

(22) Damasceno, L. M., Pla, I., Chang, H.-J., Cohen, L., Ritter, G., Old, L. J., and Batt, C. A. (2004) An optimized fermentation process for high-level production of a single-chain Fv antibody fragment in Pichia pastoris. *Protein Expression and Purification 37*, 18-26.

(23) Mohr, F. (2009) *Gold Chemistry: Applications And Future Directions In The Life Sciences*, Wiley.

(24) Cereghino, G. P., Cereghino, J. L., Ilgen, C., and Cregg, J. M. (2002) Production of recombinant proteins in fermenter cultures of the yeast Pichia pastoris. *Curr Opin Biotechnol 13*, 329-32.

(25) Li, P., Anumanthan, A., Gao, X. G., Ilangovan, K., Suzara, V. V., Duzgunes, N., and Renugopalakrishnan, V. (2007) Expression of recombinant proteins in Pichia pastoris. *Appl Biochem Biotechnol 142*, 105-24.

(26) Damasceno, L. M., Anderson, K. A., Ritter, G., Cregg, J. M., Old, L. J., and Batt, C. A. (2007) Cooverexpression of chaperones for enhanced secretion of a single-chain antibody fragment in Pichia pastoris. *Appl Microbiol Biotechnol 74*, 381-9.

CHAPTER 5

CONCLUSIONS & FUTURE DIRECTION S

This body of work demonstrates the utilization of biochemistry, spectroscopy, and materials science to create better tools for SERS based investigation of biological systems. Specifically, a novel SERS biosensor for the detection of SNPs was developed, the binding kinetics and fluorescent quenching capacity of CTAB coated nanorods were investigated, and a novel protein functionalization system was created. These investigations complement each other because they researched key aspects of SERS based biosensors. The SNP sensor provided a new method of detection, the nanorod investigation provided information on nanorods useful as Raman enhancers, and the functionalization method is valuable for putting proteins on particles or surfaces for SERS experiments.

The LDR-SERS methodology provided a new platform for SNP detection which could ultimately be used as a point-of-care methodology for in-office screening of SNP profiles. In the future, multiple elements of the platform could be further researched. Increasing the number of probes that can be multiplexed would be critical for clinical use. Although diagnostic peaks can be visually indentified now, as the number of Raman spectra is increased, the peaks will begin to overlap. To solve this, further research needs to be done to deconvolute the mixed signals through principal component analysis or support vector analysis. To make the purification process less labor intensive, a method for addition of the Raman enhancing nanoparticles prior to the LDR reaction should be developed. DNA structure may have to be modified to add a hairpin or other reactive element to allow room for the ligase to interact with the DNA but also keep the nanoparticle in close proximity to the fluorophore located on the second oligonucleotide.

By investigating the fluorescence quenching and kinetic trafficking of CTAB coated nanorods, the study clarified how nanorods may be used as Raman enhancers. As previously mentioned, fluorescence quenching is important for SERS as a fluorescent signal can easily overwhelm a Raman signal. The ability of the nanorods to capture and hold non-polar molecules of interest is also critical to Raman detection of those substances. The study additionally showed that SPR could be used as a platform to model trafficking in a nanoparticle bilayer. In the future, several elements of this project could be further researched. It would be interesting to examine fluorescence quenching simultaneously with the SPR experiment. This is possible by measuring excitation and quenching optically above the chip while the light reflectance of the SPR is measured below the chip. This experiment could examine how a variety of variables interact, such as flow rate and concentration's affect on fluorescence quenching. Other interesting factors that could be investigated include how the aspect ratio of the rods or physiologically mimicking buffer conditions would affect trafficking behavior and quenching.

Development of the intein mediated, Sec dependent protein conjugation system could prove an excellent way to conjugate proteins to nanoparticles. The system allows easy, terminal conjugation of a protein to a selenocysteine residue in cell lysate or from a purification column. The selenocysteine residue then enables a variety of functionalization schemes to particles or surfaces through a reactive maleimide group or directly to the surface if it is gold or other noble metal. This project also has elements that could be further investigated. Direct conjugation of the selenocysteine to gold surfaces needs to be investigated and optimized, as it has not been empirically

tested yet in this system. Peptide ligation through the selenocysteine residue also needs to be tested and would add more utility to the system. Further optimization of the system could also be performed to find the minimum amount of selenocysteine required per mole of protein. The system currently uses excess Sec to help drive the reaction. Overall, each of these investigations contributes to an important component of SERS based biosensors and helps further scientists' ability to understand and utilize biological systems.

APPENDIX I

EXPRESSION AND PURIFICATION OF CGMP GRADE NY-ESO-1 FOR CLINICAL TRIALS

Adapted with permission from "Expression and purification of cGMP grade NY-ESO-1 for clinical trials." Lowe et. al. Biotech. Prog. 27(2). 435-441.

Abstract:

NY-ESO-1 is a cancer testis antigen expressed in numerous cancers. Initial tests have shown its efficacy as a cancer vaccine, stimulating the body's own immune response against the invading tumor. In order to produce enough material for phase I clinical trials, a process using current Good Manufacturing Practices to produce clinical grade material was developed and executed. His-tagged NY-ESO-1 was expressed in C41DE3 *Escherichia coli* under control of the T-7 promoter. NY-ESO-1 was produced in a 20L fed-batch fermentation utilizing a pH-stat control scheme. The protein was then purified from inclusion bodies using a three-column process that achieved a yield of over 3.4 g and endotoxin below the detection limit of 0.005 EU/µg protein.

Introduction:

The NY-ESO-1 protein, also know as CTAG1 and LAGE-2, is a cancer testis (CT) antigen that holds significant promise as an immunotherapeutic vaccine. It was first identified by serological analysis of recombinant cDNA expression libraries (SEREX) from tumor mRNA and host serum. Its expression has been detected by RT-PCR and immunohistochemistry in multiple cancers, including melanoma [1], neuroblastoma [2], and soft tissue sarcoma.[3] The gene is located in q28 region of the X chromosome and is a member of the CT-X antigen family.[4] NY-ESO-1 is one of the most immunogenic CT-antigens, eliciting immunity spontaneously and after vaccine administration [5]. Clinical responses were also detected in chemo-refractory cancers [5].

CT antigens make excellent vaccine candidates as their expression is limited to only cancerous cells and normal, testis germ cells [6]. Testis germ cells are MHC class 1 negative however [7] and will not elicit a cytotoxic response. To this end, NY-ESO-1 vaccines supplemented with the ISCOMATRIX adjuvant have been successful in melanoma vaccine trials [8]. NY-ESO-1 has also been shown to be a prognostic factor for malignant melanoma (MM). It was additionally demonstrated that MM expressing NY-ESO-1 was associated with thicker primary lesions, and had a higher frequency metastatic disease [9]. NY-ESO-1 vaccines were shown to be even more successful when combined with an anti-CTLA-4 antibody treatment, as CTLA-4 has been shown to downregulate T-cell signaling and activity [10]. Due to the protein's success in initial experiments, a critical need is growing for material used in limited phase-I clinical trials. Pilot-scale production of vaccine antigens, under current good manufacturing practices (cGMP), fills an important role where industrial scale production may not be

economically viable.

Here we have developed a process suitable for the pilot-scale production of cGMP grade His-tagged NY-ESO-1. Due to its extremely high hydrophobicity, the protein presented complex solubility and endotoxin removal challenges that were addressed during process development. After strain development, the process was scaled to a 2L fermentor using a fed-batch program and initial chromatographic development was conducted on the bench scale. Development and production was then moved into our cGMP-certified Biologics Production Facility.

Materials and Methods:

All materials were purchased at the highest purity possible and certificates of analysis from the manufacturer were retained. All equipment was cleaned and tested in accordance with cGMP guidelines. All of the staff was trained on and followed cGMP guidelines during production of the biopharmaceutical material. *Water for injection* grade water was used for all solutions (Hyclone Inc. Logan, UT). All chromatography was performed using an Akta Purifier (GE Healthcare, Piscataway, NJ) controlled by Unicorn software version 4.12 (GE Healthcare, Piscataway, NJ). All chromatography columns were packed in-house and validated for symmetry and plate count as directed by manufacturer. Protein and endotoxin concentrations were established using Bradford and Limulus Amebocyte Lysate assays respectively, as previously described [11].

Plasmid & Strain Construction:

The NY-ESO-1 sequence was obtained from the GenBank database (Gene 1485,

Genbank BC130362.1). A synthetic NY-ESO-1 gene was constructed via PCR. The overlapping oligonucleotides (Table 1) were assembled and subjected to two successive rounds of PCR amplification to generate a 579 bp fragment using Platinum Taq DNA Polymerase HF (Invitrogen Corp, Carlsbad, CA). In the first round, primers 1-10 (Table 1) were combined and cycled 20 times. For the second round, a one-tenth volume of the first round PCR was added to the second round that contained primers 11-12 and was cycled 30 times. The resulting fragment was then cloned into pCR2.1 (Invitrogen Corp., Carlsbad, CA) and sequenced with four-fold coverage. After successful sequencing, the construct was subcloned into pET-9a24a, a derivative of the pET9a vector, with the repressor binding site and *lacI* gene removed. The construct was then transformed into C41(DE3) *E. coli* (Lucigen Corp., Middleton, WI) and positive clones selected by Kanamycin resistance. The pRARE plasmid, which encodes tRNAs rarely used in bacteria, was then transformed into the cells using Chloramphenicol as a marker. From a single positive clone, master and working cell banks were established. The banks were fully characterized by re-sequencing and performing diagnostic restriction digests of the plasmids, identifying the C41 *E. coli* species by 16S sequencing and IPTG tolerance phenotype, and western blot analysis of lysate using anti-NY-ESO-1 monoclonal antibody before and after expression of NY-ESO-1 was induced (data not shown).

Fermentation:

A 1 ml aliquot from the working cell bank was completely thawed at room temperature and added to 50 ml of production culture medium, as previously described

Number	Oligonucelotide Sequence (5'-3')
1	CATATGCAAGCAGAAGGTCGTGGTACAGGTGGTTCTACGGGCGATGCTGATGGCCCAGGAGGT CCAGGCATTCCAGAT
2	AGGCGGGTGCAACTGGTGGCCGTGGTCCACGTGGTGCAGGAGCTGCTCGTGCATCAGGTCCAG GAGGAGGAGCACCTC
3	ATGGATGTTGTCGTTGTGGCGCACGTGGTCCGGAGAGCCGCCTGCTTGAGTTCTATCTTGCCA TGCCTTTCGCGACTC
4	GCACAGGATGCTCCACCGCTTCCGGTTCCTGGTGTGCTTCTGAAGGAGTTCACTGTGTCCGGC AACATTCTGACTATC
5	CACCGCCAACTGCAGCTCTCCATCAGTTCGTGTCTCCAGCAGCTTTCCCTGTTGATGTGGATC ACGCAGTGCTTCCTG
6	GACCACGGCCACCAGTTGCACCCGCCTCACCTGGACCACCTGCATTACCCCCTGGACCATCTG GAATGCCTGGACCTC
7	CGCCACAACGACAACATCCATTAAGACCAGAAGCTGCGCCACCATGTGGACCGCGAGGTGCTC CTCCTCCTGGACCTG
8	AAGCGGTGGAGCATCCTGTGCCAGACTACGGCGTGCCAGTTCAGCTTCCATTGGAGTCGCGAA AGGCATGGCAAGATA
9	ACGAACTGATGGAGAGCTGCAGTTGGCGGTGGTCTGCGGCGGTCAGTCGGATAGTCAGAATGT TGCCGGACACAGTGA
10	GCGGCCGCTTAACGGCGTTGCCCTGATGGAGGTTGAGCTAAAAACACAGGCAGGAAGCACTGC GTGATCCACATCA
11	CATATGCAAGCAGAAGGTCGTGGTACAGGTGGTTCTACG
12	GCGGCCGCTTAACGGCGTTGCCCTGAT

Table 1. Oligonucleotide Sequences for Gene Construction

[11], in a sterile 250 ml flask. This was cultured overnight at 37°C and 250 rpm. The culture was then inoculated into 350 ml of production media in a sterile 2 L shake flask. Cells were grown for 2 hours at 37˚C, after which they were aseptically introduced into a 30L BioFlo 4500 Bioreactor (New Brunswick Scientific, New Brunswick, NJ) containing 7L of production media. The reactor was controlled and data was logged using AFS-Biocommand Bioproessing software version 2.6 (New Brunswick Scientific, New Brunswick, NJ). During fermentation, dissolved oxygen (DO) was maintained at 40% of saturation and was controlled by a DO cascade of agitation (maximum of 1000 rpm) followed by supplementation with pure oxygen as needed. The temperature, pH, and gas flow were set to 37°C, 6.8, and 20 standard liters per minute respectively. pH was maintained during the batch phase of the fermentation with 5M NaOH. Upon consumption of the glucose in the batch phase, the base feed was turned off and 12.5 L of glucose feed containing IPTG was started, as previously formulated. [11]. Feed rate was controlled using a pH-stat feedback mechanism.

Harvest, Lysis, and Inclusion Body Isolation:

Fermentation culture was harvested into a sterile bioprocess bag, and then fed into a Carr Powerfuge Pilot (Pneumatic Scale Corp., Cuyahoga Falls, OH) spinning at maximum speed, from which the resulting cell pellet was collected. Approximately one half of the concentrated biomass was frozen at -20°C to be processed later in a manner identical to the first, while the second half was resuspended in 15 L of lysis buffer containing 50 mM Tris Base, 100 mM NaCl, 1 mM $MgSO_4$, 1 mM ß-mercaptoethanol, 1 ml “Turbo” DNase (Ambion, Inc., Austin, TX) at pH 8.0. Portions

of the cell suspension were sequentially blended in a 4 L Waring laboratory blender and transferred to a clean, sterile bioprocess bag. The disrupted cells were then passed through a Microfluidics Microfluidizer M100EH (Microfluidics International Corp., Newton, MA) at 23 Kpsi three times. The lysate was then pumped into a Millipore M-30 tangential flow filtration (TFF) (Billerica, MA) system equipped with two, 0.2 µm Centrasette II cassettes (Pall Corp., Port Washington, NY). Diafiltration was then performed on the lysate, first washing with 50 L of Tris buffer (50 mM Tris Base, 100 mM NaCl, 1 mM $Na_2EDTA \bullet 2H_2O$, 1 mM ß-mercaptoethanol at pH 8) then 50 L of phosphate buffer (50 mM phosphate, 500 mM NaCl, 1 mM ß-mercaptoethanol at pH 7.5). The inclusion body suspension was then concentrated 10-fold.

Solubilization and Filtration:

Processed inclusion bodies were solubilized for 16 hours while being mixed by an overhead mixer in 35 L of solubilization buffer [2% m/v deoxycholate (sodium salt), 8M urea, 50 mM phosphate, 200 mM NaCl, 100 mM KCl, 10 mM imidazole, 2.5 mM ß-mercaptoethanol at pH 7.5]. The solution was then passed through a 10" 1.2 µm low protein binding filter (LPBF) and subsequently a 10" 0.5 µm LPBF.

Immobilized Metal Affinity Chromatography & Buffer Exchange:

The filtered lysate was loaded at 100 mL/min onto a 5 L column containing nickel-bound Chelating Sepharose Fast Flow resin (GE Healthcare, Piscataway, NJ), previously equilibrated with two column volumes (CVs) of solubilization buffer. Each chromatography fraction was collected into sterile bioprocess bags. The program had the following design: 2 CV load, 7 CV solubilization buffer wash, 5 CV urea buffer (4M urea, 50 mM phosphate, 2.5 mM ß-mercaptoethanol at pH 7.5) wash, 5 CV 15%

imidazole buffer (formulated as urea buffer with 500 mM imidazole) diluted into urea buffer, and 3 CV elution with 100% imidazole buffer (1 M imidazole). The elution fraction was concentrated to 1 L using a Millipore ProFlux M12 TFF system with two 10 KDa Centramate cassettes (Pall). The retentate was then exchanged with 5 L of urea buffer and collected into a sterile bioprocess bag.

Anion Exchange Chromatography:

The buffer exchanged retentate was loaded at 50 ml/min onto a 1 L column containing Q Sepharose XL resin (GE Healthcare, Piscataway, NJ) at 50 ml/min. The purification program had the following design: 2 CV equilibration with urea buffer, 1 CV load, and 2 CV urea buffer wash/elution. The load flowthrough and wash were collected as one fraction in a sterile 10 L bioprocess bag.

Hydrophobic Interaction Chromatography:

The AXC flowthrough/wash fraction was diluted to a protein concentration of 0.4 mg/ml using urea buffer, and subsequently diluted with ammonium sulfate buffer (4 M urea, 50 mM sodium phosphate, 2 M ammonium sulfate, 2.5 mM ß-mercaptoethanol) such that the final concentration of ammonium sulfate was 0.7 M. This was loaded at 50 ml/min onto 1 L column containing Phenyl HP (GE Healthcare, Piscataway, NJ) resin that had been pre-equilibrated with urea buffer supplemented with 0.7 M ammonium sulfate. After loading, the column was washed with equilibration buffer for 2 CVs. The protein of interest was then eluted in three fractions using a HIC elution buffer [4M urea, 0.5% Triton (v/v), 50 mM sodium phosphate, and 2.5 mM ß-mercaptoethanol at pH 7.5]. Fractionation was controlled using the Unicorn software manually, based on 280 nm absorbance.

Final Buffer Exchange and Terminal filtration:

The fractions eluted off the HIC column were concentrated to 1 L as described above in an M-12 TFF system and then buffer exchanged with 6 L of final bulk buffer (4M urea, 50 mM phosphate, 145 mM NaCl, 50 mM glycine). The product was then passed through a sterile 0.22 µm disc filter (Millipore, catalog number MPGL06GF2) under sterile conditions into a bioprocess bag.

Results and Discussion:

Plasmid and Cell Bank Construction:

In order to improve expression of NY-ESO-1, a synthetic gene was constructed. This lowered the GC percentage from 67.4% to 56%, allowed for *E. coli* codon optimization, and minimized potential for stem-loop structures. This final construct was cloned into pET9a24a (Figure 1). Due to the deletion of *lacI* and the repressor-binding site, higher expression levels were achieved as compared to the stock plasmids. The C41 strain of *E. coli* cells was chosen due to its strong growth during batch and fed-batch (induction) phases, high levels of target protein expression and its historic ability to produce membrane proteins [12-15]. This allowed IPTG to be included in the glucose feed during the fermentation, which made the fermentation more streamlined and achieved high cell mass while achieving high protein yield. C41(DE3) cells, which are derived from BL21(DE3)[16], have at least one uncharacterized mutation which allows them to produce these normally toxic proteins.

Fermentation:

The fermentation profile of cells expressing NY-ESO-1 is shown in Figure 2. The fermentor was prepared, DO probe allowed to polarize, and then inoculated at

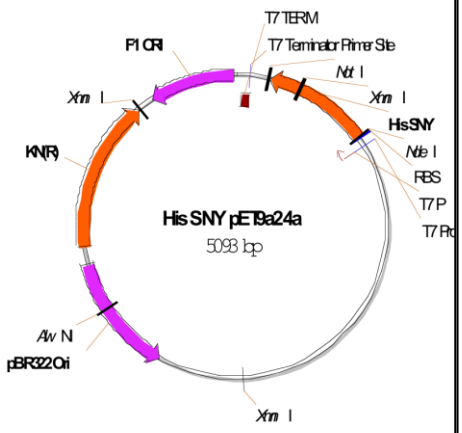

Feature	Description	Location	Purpose
CDS	His SNY	176-754	His tagged synthetic NY-ESO-1
	KN(R)	3719-4531	Kanamycin resistance gene
PBS	T7 Terminator	68-86	Primer binding site
	T7 Promoter	811-830	Primer binding site
PRO	T7 P	814-830	Expression promoter
RBS	RBS	760-765	Ribosomal binding site
ORI	pBR322 ORI	2977-3620	Origin of replication
	F1 ORI	4626-5081	Origin of replication
TERM	T7 TERM	25-71	Transcription terminator

MRGSHHHHHH GSMQAEGRGT GGSTGDADGP GGPGIPDGPG GNAGGPGEAG
ATGGRGPRGA GAARASGPGG GAPRGPHGGA ASGLNGCCRC GARGPESRLL
EFYLAMPFAT PMEAELARRS LAQDAPPLPV PGVLLKEFTV SGNILTIRLT
AADHRQLQLS ISSCLQQLSL LMWITQCFLP VFLAQPPSGQ RR ***

Figure 1. Top Panes – NY-ESO-1 in pET9a24a plasmid map and key. Bottom Pane- Amino Acid Sequence of NY-ESO-1. Asterisks indicate an ochre stop codon.

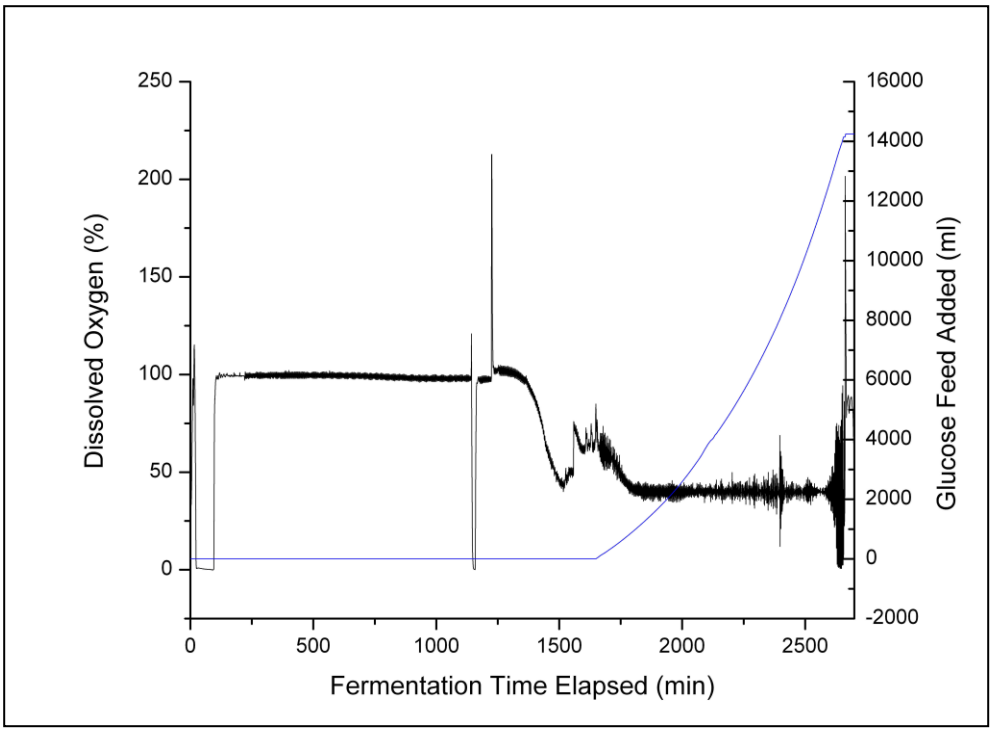

Figure 2. Fermentation profile of NY-ESO-1. Dissolved oxygen (black) and glucose feed (blue) measurements. A pH-stat control method was used to determine feed rate.

approximately 1150 minutes. In Figure 2, a sharp drop in DO is noticeable at approximately 1300 minutes, indicating the beginning of glucose consumption in the batch phase. Shortly thereafter, a DO spike indicated exhaustion of glucose. The software turned on the glucose feed, and the DO returned to the target DO of 40% of air saturation. As total biomass mass increased, DO was maintained by an increase in agitation and supplementation of pure oxygen. Figure 2 shows the rapid increase in feed rate to compensate for cell growth. Feeding rate was controlled by a pH feedback loop. In this strategy, available glucose is kept at a minimum and feeding rate is only affected by pH [17]. As bacteria grow, they acidify the media, thus pH can be used as a measure of growth. Approximately twenty-four hours after inoculation, the cells were harvested, achieving a cell density of 232.7 g/L wet cell weight.

Purification:

After harvest, the cells were lysed to obtain inclusion bodies, which were subsequently washed with by diafiltration. Tris and phosphate buffer washes differentially removed a significant amount of contaminating host proteins as seen in Figure 3, lanes 3-5. After concentration, solubilization in 8M urea, and filtration through 1.2 and 0.5 μm filters, the lysate was loaded onto a 5L nickel-charged IMAC column. The chromatogram in Figure 4 presents the purification of NY-ESO-1 on the IMAC column. After loading (Figure 4A1), the bound protein was washed with a deoxycholate/Triton-114 solution (Figure 4A2) to remove lipopolysaccharides (endotoxin) bound to the protein. During development, it was found that NY-ESO-1 strongly bound endotoxin, as do many other CT-Antigens [18]. This multi-detergent wash is key to drastically reducing endotoxin levels in the protein preparation.

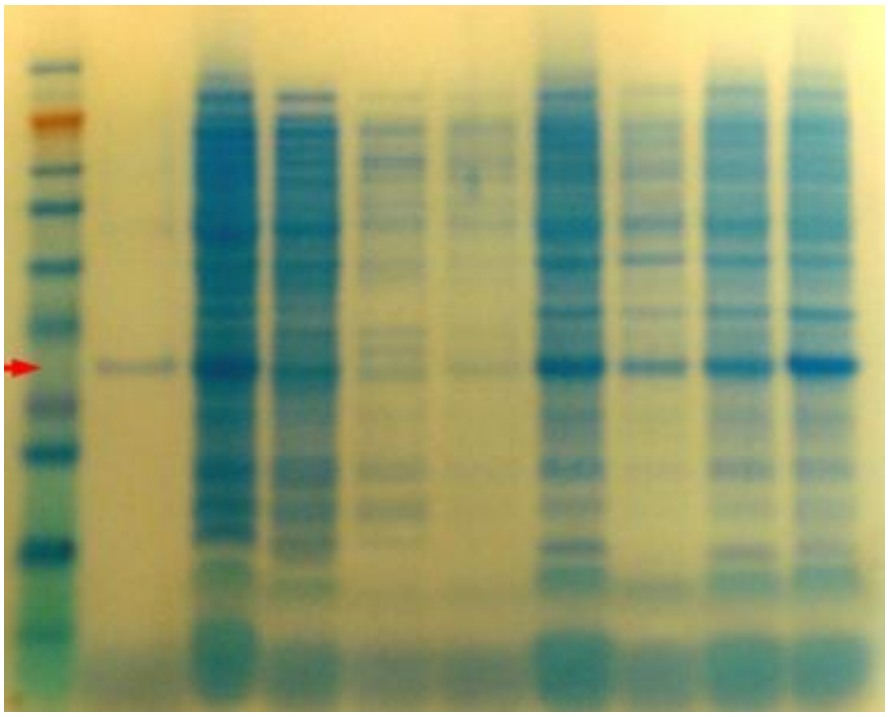

Figure 3. A: Coomassie-stained SDS-PAGE gel of TFF and IMAC column. Lanes 1–10 correspond to: ladder, NY-ESO-1 standard, crude lysate, Tris wash permeate, phosphate wash permeate, concentration permeate, TFF retentate, cassette wash retentate, and concentration retentate. Arrow corresponds to NY-ESO-1 monomer

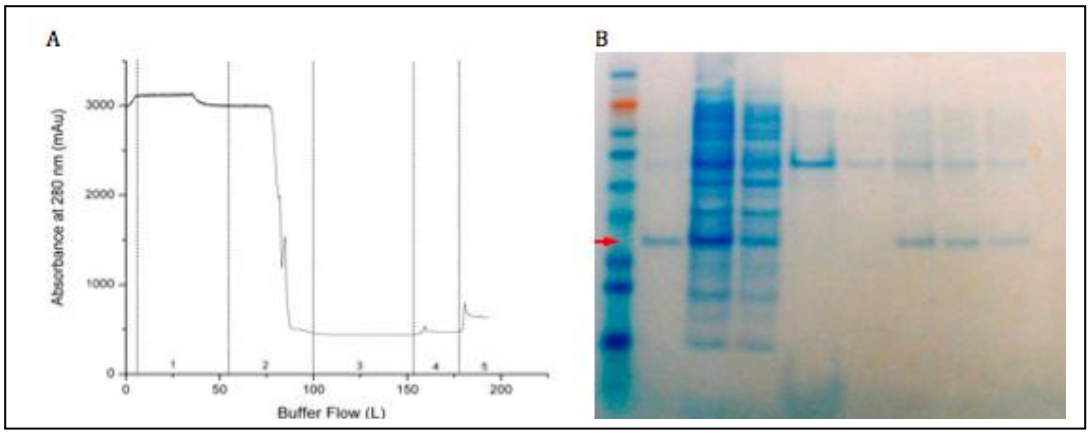

Figure 4. A: Chromatogram of IMAC column. Fractions 1–5 correspond to: load, deoxycholate wash, urea wash, low-imidazole wash, elution. B: Coomassie-stained SDS-PAGE gel of IMAC column fractions. Lanes 1–10 correspond to: ladder, NY-ESO-1 standard, load, load FT, deoxycholate wash, low-imidazole wash, early high-imidazole elution, mid-high-imidazole elution, late high-imidazole elution, and blank. Arrow indicates NY-ESO-1 monomer

Subsequent column steps are able to reduce endotoxin to below detectable limits, as seen in Table 2. The detergent wash step is additionally important because it removes latent endotoxin that later dissociates from NY-ESO-1. A previous batch of NY-ESO-1 that did not originally include a detergent wash step was measured at less than 0.1 EU/µg, and over a fourteen month period rose to 0.6 EU/µg. Another batch behaved similarly, rising from 0.27 EU/µg to 1.6 EU/µg over ten months. Batches made using the process described here have maintained undetectable levels of endotoxin for a year at the time of this article.

Figure 4A3 shows that the urea wash is able to remove the detergent from the protein preparation, as seen from the drop in 280 nm absorbance. Figure 4A4 and 4A5 shows the low imidazole wash and high imidazole elution. Figure 4B illustrates the purification resulting from the IMAC column step. Although some NY-ESO-1 is lost in the load flow-through (FT), as seen in Figure 4B lane 4, most host proteins pass through the IMAC column. A single band is seen in the deoxycholate wash and low Imidazole wash lanes, but does not react on an anti-NY-ESO-1 western blot (data not shown). Figure 4B lanes 7-9 show consistent elution of NY-ESO-1 throughout the elution step. The upper band eluted does appear in an anti-NY-ESO-1 western blot. Note the slightly lower molecular weight as compared to the band appearing in the deoxycholate wash lane. The eluted protein was then buffer exchanged into an AXC buffer with a seven percent loss of total protein mass.

Anion exchange chromatography was performed following the IMAC column, as an initial polishing step (Figure 5). The chromatogram of the process can be seen in Figure 5A. In addition, contaminants such as host proteins and endotoxin, with a

Sample	Endotoxin Concentration (EU/ml)
IMAC Load	4913800
QXL Load	316.1
QXLElution	10.9
HIC Load	< 5
HIC Elution	< 5
Final Bulk	< 5

Table 2. Endotoxin Concentration During Processing

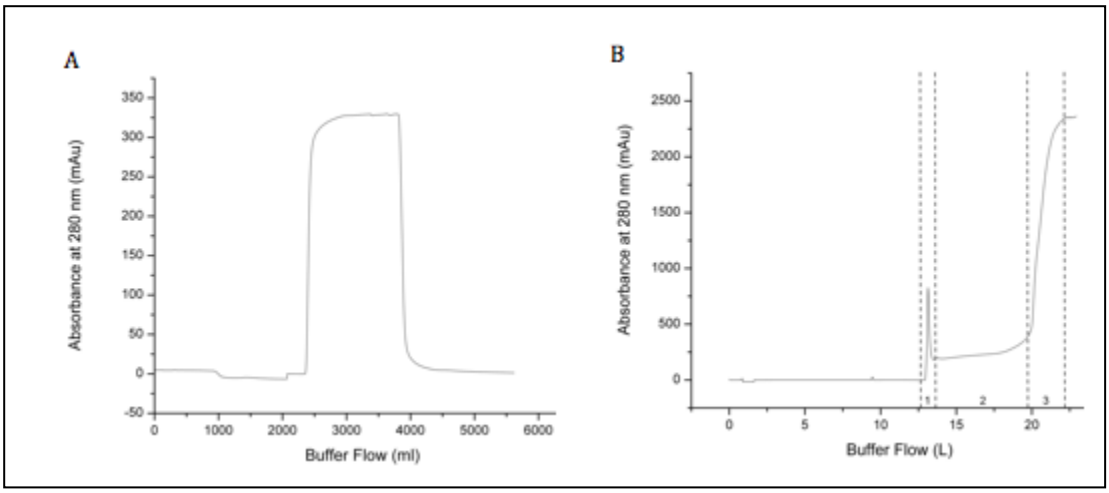

Figure 5. A: Anion exchange column chromatograph and B: HIC chromatograph. Elution fractions indicated by dotted lines and numbers

higher binding affinity to the anion exchange matrix under these conditions, remained bound. No decrease in NY-ESO-1 yield was observed as seen in Figure 6, lanes 3 and 4. The AXC flow through was then diluted and supplemented with 0.7 M ammonium sulfate in preparation for the HIC column.

Hydrophobic interaction chromatography was used as the third and final polishing step for NY-ESO-1 purification (Figure 5B). After protein loading and urea buffer wash, NY-ESO-1 was eluted in three fractions with a 0.1% (v/v) Trition-114 solution in aqueous 4M urea, as seen in Figure 5B. No conditions were changed during the elution, but three distinct fractions are obtained. The protein profile in each of these fractions was identical despite the higher protein concentration in fraction 1 (Figure 6, lanes 8-10). As a result of its hydrophobic nature, elution of NY-ESO-1 from the HIC column required formulation of the elution buffer with Triton-114.The elution pattern of the protein is believed to have occurred because of an interaction between the detergent and the hydrophobic resin. The initial spike in absorbance seen in fraction 1 occurred as expected, when the presence of detergent in the elution buffer assisted in release of a majority of protein. As the elution step continued, NY-ESO-1 could still be detected in fraction 2 and a slow rise in absorbance was observed. We believe detergent buildup on the hydrophobic column released in fraction 3. The sharp rise in 280 nm absorbance was associated with the strong UV absorbance of Triton-114. The fraction collection was ended prior to the plateau of the peak where a majority of the Triton was found. No protein was detected in the plateau portion of the chromatogram. Previous experiments showed the importance of cutting the peak prior to the plateau, as it greatly reduces Triton-114 contamination in the protein preparation.

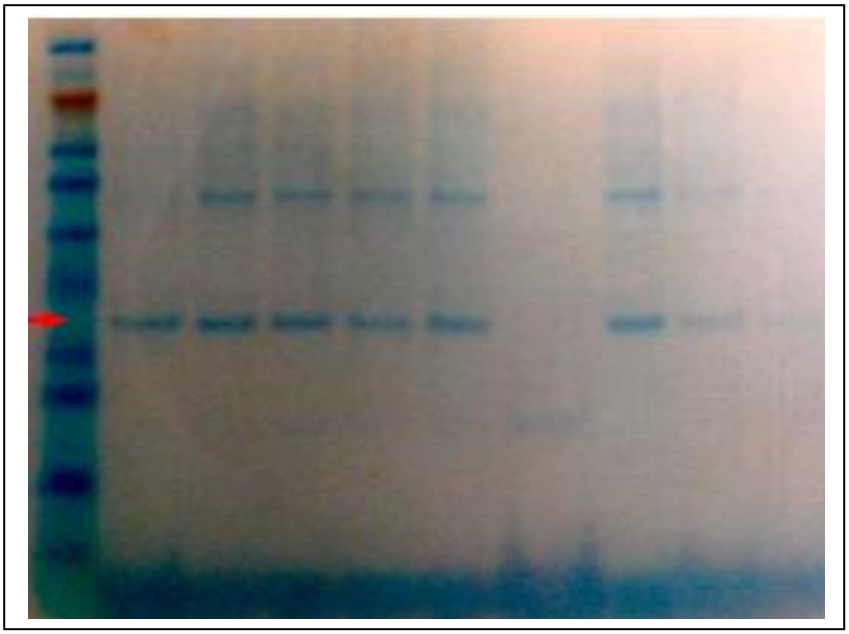

Figure 6. Coomassie-stained SDS-PAGE gel of AXC and HIC fractions. Lanes 1–10 correspond to ladder, NY-ESO-1 standard, AXC load, AXC FT, prefiltered HIC load, HIC load, HIC FT, HIC fraction 1, HIC fraction 2, and HIC fraction 3. Arrow indicates NY-ESO-1 monomer.

The three HIC elution fractions were pooled then buffer exchanged into the final bulk buffer and terminally filtered under sterile conditions. Confirmation of detergent removal was achieved by HPLC (data not show). A summary SDS-PAGE and western blot using anti-NY-ESO-1 can be seen in Figure 7A&B respectively. Figure 7A shows that most of the protein purification occurs at the IMAC step, as would be expected. Some higher molecular weight proteins remain throughout the purification process. The higher molecular weight bands have been determined by mass spectrometry to be NY-ESO-1 bound to chaperone proteins such as DNA J, DNA K, and GroEL, as well as multimers of NY-ESO-1 (data not shown). The presence of NY-ESO-1 in these higher molecular bands was also confirmed by anti-NY-ESO-1 western blot (Figure 7B). Release of NY-ESO-1 from the chaperone proteins was extensively investigated, but could not be achieved, despite methods such as reducing agents, chromatography, and altering the salt compositions and concentrations in buffers.

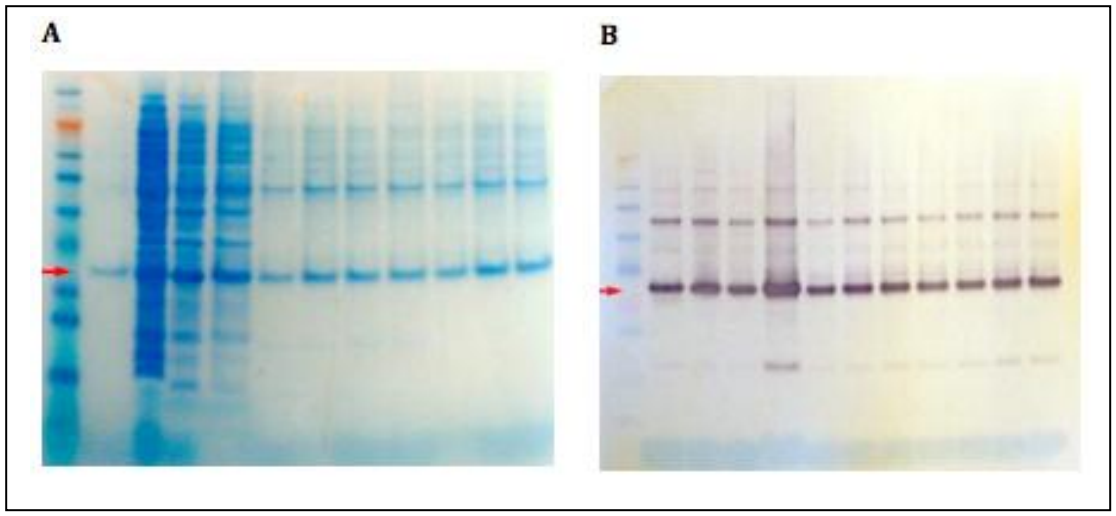

Figure 7. A: Coomassie stained summary SDS-PAGE gel. B: Anti-NY-ESO-1 Western blot of summary gel. Lanes 1–12 for A and B correspond to: ladder, NY-ESO-1 standard, crude lysate, TFF retentate, IMAC load, IMAC elution, QXL load, QXL elution, HIC load, HIC-pooled elution, prefiltered final bulk, and filtered final bulk. Arrow indicates NY-ESO-1 monomer

Conclusions:

This protein typifies CT antigens in that it was challenging to produce at the pilot scale under GMP conditions. Due to its hydrophobic nature, which leads to extremely low solubility in aqueous solution, NY-ESO-1 requires 8M urea during initial stages of purification and 4M urea once it has been eluted from the IMAC column. NY-ESO-1 strongly binds endotoxin and requires a multi-detergent wash to remove the majority of this contaminant before polishing on secondary chromatography columns. Despite these challenges however, we were able to produce over 3 g of GMP grade NY-ESO-1 from a single 20 L fermentation. Most importantly, this material will enter limited phase-1 clinical trials where it is anticipated it will save patients' lives.

References:

1. Vaughan, H. A.; Svobodova, S.; Macgregor, D.; Sturrock, S.; Jungbluth, A. A.; Browning, J.; Davis, I. D.; Parente, P.; Chen, Y. T.; Stockert, E.; St Clair, F.; Old, L. J.; Cebon, J., Immunohistochemical and molecular analysis of human melanomas for expression of the human cancer-testis antigens NY-ESO-1 and LAGE-1. *Clin Cancer Res* **2004,** 10, (24), 8396-404.

2. Rodolfo, M.; Luksch, R.; Stockert, E.; Chen, Y. T.; Collini, P.; Ranzani, T.; Lombardo, C.; Dalerba, P.; Rivoltini, L.; Arienti, F.; Fossati-Bellani, F.; Old, L. J.; Parmiani, G.; Castelli, C., Antigen-specific immunity in neuroblastoma patients: antibody and T-cell recognition of NY-ESO-1 tumor antigen. *Cancer Res* **2003,** 63, (20), 6948-55.

3. Jungbluth, A. A.; Antonescu, C. R.; Busam, K. J.; Iversen, K.; Kolb, D.; Coplan, K.; Chen, Y. T.; Stockert, E.; Ladanyi, M.; Old, L. J., Monophasic and biphasic synovial sarcomas abundantly express cancer/testis antigen NY-ESO-1 but not MAGE-A1 or CT7. *Int J Cancer* **2001,** 94, (2), 252-6.

4. Simpson, A. J.; Caballero, O. L.; Jungbluth, A.; Chen, Y. T.; Old, L. J., Cancer/testis antigens, gametogenesis and cancer. *Nat Rev Cancer* **2005,** 5, (8), 615-25.

5. Szmania, S.; Tricot, G.; van Rhee, F., NY-ESO-1 immunotherapy for multiple myeloma. *Leuk Lymphoma* **2006,** 47, (10), 2037-48.

6. Caballero, O. L.; Chen, Y. T., Cancer/testis (CT) antigens: potential targets for immunotherapy. *Cancer Sci* **2009,** 100, (11), 2014-21.

7. Guillaudeux, T.; Gomez, E.; Onno, M.; Dr√©nou, B.; Segretain, D.; Alberti,

S.; Lejeune, H.; Fauchet, R.; J√©gou, B.; Le Bouteiller, P., Expression of HLA class I genes in meiotic and post-meiotic human spermatogenic cells. *Biol. Repro.* **1996,** 55, (1), 99-110.

8. Davis, I. D.; Chen, W.; Jackson, H.; Parente, P.; Shackleton, M.; Hopkins, W.; Chen, Q.; Dimopoulos, N.; Luke, T.; Murphy, R.; Scott, A. M.; Maraskovsky, E.; McArthur, G.; MacGregor, D.; Sturrock, S.; Tai, T. Y.; Green, S.; Cuthbertson, A.; Maher, D.; Miloradovic, L.; Mitchell, S. V.; Ritter, G.; Jungbluth, A. A.; Chen, Y. T.; Gnjatic, S.; Hoffman, E. W.; Old, L. J.; Cebon, J. S., Recombinant NY-ESO-1 protein with ISCOMATRIX adjuvant induces broad integrated antibody and CD4(+) and CD8(+) T cell responses in humans. *Proc Natl Acad Sci U S A* **2004,** 101, (29), 10697-702.

9. Velazquez, E. F.; Jungbluth, A. A.; Yancovitz, M.; Gnjatic, S.; Adams, S.; O'Neill, D.; Zavilevich, K.; Albukh, T.; Christos, P.; Mazumdar, M.; Pavlick, A.; Polsky, D.; Shapiro, R.; Berman, R.; Spira, J.; Busam, K.; Osman, I.; Bhardwaj, N., Expression of the cancer/testis antigen NY-ESO-1 in primary and metastatic malignant melanoma (MM)--correlation with prognostic factors. *Cancer Immun* **2007,** 7, 11.

10. Yuan, J.; Gnjatic, S.; Li, H.; Powel, S.; Gallardo, H. F.; Ritter, E.; Ku, G. Y.; Jungbluth, A. A.; Segal, N. H.; Rasalan, T. S.; Manukian, G.; Xu, Y.; Roman, R. A.; Terzulli, S. L.; Heywood, M.; Pogoriler, E.; Ritter, G.; Old, L. J.; Allison, J. P.; Wolchok, J. D., CTLA-4 blockade enhances polyfunctional NY-ESO-1 specific T cell responses in metastatic melanoma patients with clinical benefit. *Proc Natl Acad Sci U S A* **2008,** 105, (51), 20410-5.

11. Huang, C. J.; Chen, R. H.; Vannelli, T.; Lee, F.; Ritter, E.; Ritter, G.; Old, L. J.; Batt, C. A., Expression and purification of the cancer antigen SSX2: a potential cancer vaccine. *Protein Expr Purif* **2007,** 56, (2), 212-9.

12. Bateman, A.; Bycroft, M., The structure of a LysM domain from E. coli membrane-bound lytic murein transglycosylase D (MltD). *JMB* **2000,** 299, (4), 1113-1119.

13. Khang, T.; Jungyuen, C.; Carla, M. F.; Francesca, M. M., Bcl-XL as a fusion protein for the high-level expression of membrane-associated proteins. *Prot. Sci.* **2005,** 14, (4), 948-955.

14. Pos, K. M.; Diederichs, K., Purification, crystallization and preliminary diffraction studies of AcrB, an inner-membrane multi-drug efflux protein. *Act. Cryst. Sect. D* **2002,** 58, (10 Part 2), 1865-1867.

15. Tse, E.; Lobato, M. N.; Forster, A.; Tanaka, T.; Chung, G. T. Y.; Rabbitts, T. H., Intracellular antibody capture technology: application to selection of intracellular antibodies recognising the BCR-ABL oncogenic protein. *JMB* **2002,** 317, (1), 85-94.

16. Miroux, B.; Walker, J. E., Over-production of Proteins inEscherichia coli: Mutant Hosts that Allow Synthesis of some Membrane Proteins and Globular Proteins at High Levels. *JMB* **1996,** 260, (3), 289-298.

17. Kim, B. S.; Lee, S. C.; Lee, S. Y.; Chang, Y. K.; Chang, H. N., High cell density fed-batch cultivation of Escherichia coli using exponential feeding combined with pH-stat. *Bioprocess Biosyst Eng* **2004,** 26, (3), 147-50.

18. Chen, R. H.; Huang, C., Jr.; Newton, B. S.; Ritter, G.; Old, L. J.; Batt, C. A., Factors affecting endotoxin removal from recombinant therapeutic proteins by anion

exchange chromatography. *Protein Expr Purif* **2009,** 64, (1), 76-81.

APPENDIX II

PROCESS DEVELOPMENT AND PRODUCTION OF CGMP GRADE MELAN-A FOR CANCER VACCINE CLINICAL TRIALS

Abstract:

Melan-A is a cancer testis antigen commonly found in melanoma, and has been shown to stimulate the body's immune response against cancerous cells. We have developed and executed a process utilizing current good manufacturing practices (cGMP) to produce the 6x-His tagged protein for use in Phase I clinical trials in C41DE3 *Escherichia coli*. Half of a 20 L fed-batch fermentation produced over 5.5 grams of purified Melan-A with less than 0.005 EU/ml endotoxin levels. Purification was achieved through a three column process utilizing immobilized metal affinity, anion exchange, and cation exchange chromatography with a buffer system optimized for low-solubility, high LPS binding capacity proteins.

Introduction:

The Melan-A protein, also known as MART-1, has been used as a diagnostic marker[1] for melanoma as well as an immunotherapeutic agent.[2] The tumor associated antigen (TAA) contains 118 amino acids, with 21 amino acids predicted to compose a transmembrane domain and 92 solvent exposed.[3] Melan-A was originally cloned by the Ludwig Institute for Cancer Research[4] and was independently cloned by the NIH who termed it MART-1 (Melanoma Antigen Recognized by T-cells)[5]. The protein is expressed only in melanocytes, the retina, and most melanoma cancers. While it is expressed in virtually all metastatic melanomas, some primary, cutaneous melanomas have stained Melan-A negative.

Melan-A is a member of the MAGE gene family,[6] which includes many TAAs that are recognized by cytotoxic T lymphocytes (CTL). Once recognized, CTLs lyse the cancerous cell.[7] NY-ESO-1[8] and SSX-2[9] are two related TAAs which provoke similar reactions from CTLs and have had some success as cancer vaccines. Interestingly, it has been demonstrated that HLA phenotype strongly influences the efficacy of Melan-A vaccination due to the ability of the HLA molecule to present the antigen.[10] Other TAAs appear to be antigenic when displayed by multiple HLA phenotypes.[5, 11]

Melan-A peptides have been delivered through viral vectors and directly as peptide solutions for use as cancer vaccine antigens. Virally, Melan-A has been expressed using lentiviral[12], adenoviral[13], and poxviral[14, 15] vector systems. The studies' results strongly supported the use of Melan-A as an immunotherapy. This is especially

well supported by the phase I/II clinical trials using inactivated vaccinia virus. Individuals have also been vaccinated with Melan-A peptides intravenously as part of clinical trials. In order to elicit a stronger CTL response, adjutants[16] and combination therapies have been used. There has been significant evidence that masking the CTLA-4 protein on helper T-cells can significantly increase the immune response to vaccine antigens.[17-19] As with any selective agent, resistance to CTLs has been observed[20] and is further evidence that combination therapies are required for these vaccine treatments.

We have developed and successfully conducted a process to produce His-tagged cGMP grade Melan-A at the pilot-scale for clinical trials. The process utilizes a 20 L fed-batch fermentation and a three column purification scheme to remove contaminating proteins and endotoxin. With the protein's initial successes, a demand has grown for clinical grade protein that exceeds lab scale but is not economically viable for industrial scale. Here will fill the gap between laboratory and industry scale to provide Melan-A for use in vaccine clinical trials under a variety of conditions.

Materials and Methods:

Materials:

All materials used were obtained at the highest purity level possible. All equipment was cleaned and tested in accordance with cGMP guidelines. Production staff followed strict cGMP training and operating procedures during production of the biopharmaceutical material. *Water for injection* grade water was used for all solutions (Hyclone Inc. Logan, UT). All chromatography was performed using an Akta Purifier (GE Healthcare, Piscataway, NJ) controlled by Unicorn software version 4.12 (GE Healthcare, Piscataway, NJ). Our production technicians packed all chromatography columns. The columns were then checked for symmetry and plate count as directed by the manufacturer. Protein and endotoxin concentrations were established using Bradford and Limulus Amebocyte Lysate assays respectively, as previously described.[21]

Plasmid & Strain Development:

The Melan-A gene sequence as deposited into Genbank (Accession Number NM_005511.1 was synthesized by IDT (Coralville, IA), with a 6x His tag added to the C-terminus to assist in purification. During gene synthesis, IDT performed codon optimization for *E. coli* for optimal recombinant expression, The Melan-A expression plasmid was constructed by sub-cloning the synthesized gene into the pET9a24a expression vector.[8] The constructed plasmid was sequenced with four fold redundancy using the forward primer 5'-taatacgactcactataggg and reverse primer 5'-caaaaaacccctcaagacccgttta. From a single positive clone, master and working cell

banks were established using the C41DE3 *E. coli* strain. Banks were subjected to extensive identity and expression testing as previously described.[8]

Methods:

Fermentation:

A vial from the working cell bank was used to inoculate 50 ml of production culture medium, as previously described[21], in a sterile 250 ml flask. The culture was shaken at 250 RPM overnight at 37˚C. The entire culture volume was then aseptically inoculated into 350 ml of production media in a sterile 2 L shake flask. Cells were shaken at 37˚C for two hours, after which they were aseptically inoculated into a 25L BioFlo 4500 Bioreactor (New Brunswick Scientific, New Brunswick, NJ) containing 7L of production media. AFS-Biocommand Bioproessing software version 2.6 (New Brunswick Scientific, New Brunswick, NJ) controlled the fermentation and logged all reaction conditions. During fermentation, dissolved oxygen (DO) was maintained at 40% of saturation and was controlled by a DO cascade of agitation (maximum of 1000 rpm) followed by supplementation with pure oxygen as needed. The temperature, pH, and gas flow were set to 37°C, 6.8, and 20 standard liters per minute respectively. 5M NaOH controlled the reactor pH during the batch phase. Upon exhaustion of the glucose in the batch phase, the base feed was turned off and 12.5 L of glucose feed containing IPTG was initiated, as previously formulated. [21] A pH-stat feedback mechanism regulated the feed rate.

Buffer Composition:

Lysis buffer: 50 mM Tris Base, 100 mM NaCl, 1 mM $MgSO_4$, 1 mM ß-mercaptoethanol, $2.5x10^{-3}$ % (v/v) "Turbo" DNase (Ambion, Inc., Austin, TX) at pH 8.0. **Solubilization buffer**: 2% m/v deoxycholate (sodium salt), 1% v/v Triton-114, 8M urea, 50 mM phosphate, 200 mM NaCl, 100 mM KCl, 10 mM imidazole, 2.5 mM ß-mercaptoethanol at pH 7.5. **Urea buffer**: 4M urea, 50 mM phosphate, 2.5 mM ß-mercaptoethanol at pH 7.5. **Imidazole buffer**: Formulated as urea buffer with 500 mM imidazole. **Carbonate buffer:** 4M urea, 10 mM Carbonate, 1 mM 2-Mercaptoethanol at pH 10.5 **Carbonate elution buffer:** Formulated as carbonate buffer with 1M sodium chloride at pH 10.5 **Final Bulk Buffer:** 4M urea, 50 mM phosphate, 145 mM NaCl, 50 mM glycine at pH 6.5

Harvest & Lysis:

The fermentate was harvested into a sterile bioprocess bag, and then fed into a Carr Powerfuge Pilot (Pneumatic Scale Corp., Cuyahoga Falls, OH) spinning at 18500 RPM, from which the resulting cell pellet was collected. Approximately one half of the concentrated biomass was frozen at -20°C to be processed later in a manner identical to the first, while the second half was resuspended in 15 L of lysis buffer. Portions of the cell suspension were sequentially disrupted in a 4 L Waring laboratory blender and transferred to a clean, sterile bioprocess bag. The disrupted cells were subjected to three passes through a Microfluidics Microfluidizer M100EH (Microfluidics International Corp., Newton, MA) at 23 Kpsi.

Solubilization and Filtration:

The lysate was solubilized for 18 hours while mixing via large stir-bar in 35 L of solubilization buffer. The solution was then passed through a 10" 1.2 µm low protein binding filter (LPBF) (Millipore Corp., Billerica, MA) and subsequently a 10" 0.5 µm LPBF (Millipore Corp., Billerica, MA).

Immobilized Metal Affinity Chromatography & Buffer Exchange:

All chromatography and mixing was done using a Akta Purifier FPLC (GE Healthcare, Piscataway, NJ) controlled by Unicorn software (GE Healthcare, Piscataway, NJ). The filtered lysate was loaded at 100 mL/min onto a 5 L column containing nickel-bound Chelating Sepharose Fast Flow resin (GE Healthcare, Piscataway, NJ), previously equilibrated with two column volumes (CVs) of solubilization buffer. Each chromatography fraction was collected into sterile bioprocess bags. The purification program used the scheme: 11 CV load, 7 CV solubilization buffer wash, 5 CV urea buffer wash, 5 CV 15% imidazole buffer diluted into urea buffer, and 3 CV elution with 100% imidazole buffer. The elution fraction was concentrated to 1 L using a Millipore ProFlux M12 TFF system with two 4 KDa Centramate cassettes (Pall). The retentate was then exchanged five-fold volumetrically with carbonate buffer and collected into a sterile bioprocess bag. The M12 system was run at 25% pump speed producing an inlet pressure of 30 PSI and outlet pressure of 20 PSI for both the concentration step and diafiltration step.

Anion Exchange Chromatography:

A 1 L column containing Q Sepharose XL resin (GE Healthcare, Piscataway, NJ) was equilibrated for 3 CVs at 50 ml/min with carbonate buffer. The retentate was then loaded with carbonate buffer at a 70:30 ratio at 50 ml/min for 3.8 CVs. The protein was then washed with 2.5 CVs of carbonate buffer and subsequently eluted with 5 CVs of carbonate elution buffer. Each fraction was collected in a separate, sterile bioprocess bag.

Cation Exchange Chromatography:

The cation exchange column was conducted as a flow through column using 50 ml/min as a constant flow rate. The column was equilibrated with 2 CVs carbonate elution buffer then was loaded with the anion exchange eluate for approximately 5 CV. The column was then washed out with 1.5 CVs of carbonate elution buffer. The load flow-through and the wash out fractions were collected into a single, sterile bioprocess bag.

Final Buffer Exchange and Terminal filtration:

The fraction collected from the cation exchange column was concentrated to 1 L as described above in an M-12 TFF system and then buffer exchanged with 6 L of final bulk buffer. The protein solution was then passed through a sterile 0.22 μm disc filter (Millipore, catalog number MPGL06GF2) under sterile conditions into a bioprocess bag for storage.

Results and Discussion:

Plasmid and Cell bank Construction

A synthetic version of Melan-A was developed to improve its production and purification. The genetic sequence was codon optimized for *E. coli* to avoid stringent responses from amino acid starvation due to codon bias [22]. The synthetic Melan-A sequence was further modified with a 6x-polyhistidine tag on the C terminus for purification. This version of Melan-A (Syn-Melan-A) has 375 base pairs encoding 124 amino acids with a mass weight of 14.1 kDa. The expression plasmid was constructed from the Syn-Melan-A insert and the pET9a24a plasmid (Figure 1). The C41 strain of *E. coli* was used as the host strain for its ability to produce high levels of membrane-derived recombinant proteins.[23]

Fermentation

The fed-batch fermentation was conducted under pH control using a feedback control loop. The DO, pH, glucose feed volume, base feed volume, and oxygen flow rate were all recorded during vessel preparation and post-inoculation. The vessel was inoculated at hour 21 of the fermentation. The batch phase is marked by acidification of the medium by the cells triggering addition of a proportionally controlled amount of sodium hydroxide into the vessel to maintain pH at 6.8. After approximately 30 ml of base was added to the vessel, the glucose feed loop was initiated but base was not added until the pH of the media increased above the set point. As shown in Figure 2, the dissolved oxygen concentration (DO) begins to plummet at 22 hours into the

A

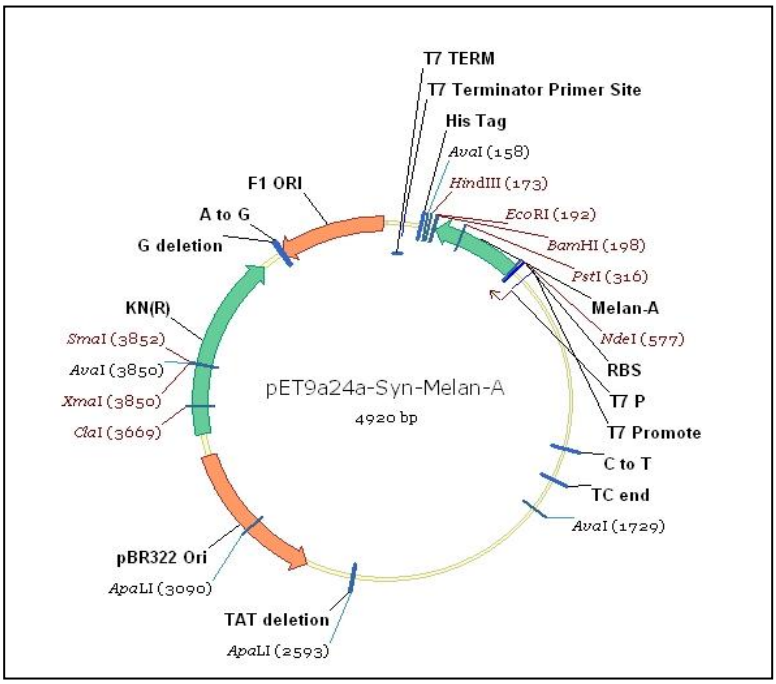

B

Feature	Description	Location	Purpose
CDS	Melan-A	203-577	His tagged synthetic Melan-A
	KN(R)	3546-4358	Kanamycin resistance gene
PBS	T7 Terminator	68-86	Primer binding site
	T7 Promoter	638-657	Primer binding site
PRO	T7 P	841-657	Expression promoter
RBS	RBS	587-592	Ribosomal binding site
ORI	pBR322 ORI	2804-3447	Origin of replication
	F1 ORI	4453-4908	Origin of replication
TERM	T7 TERM	25-71	Transcription terminator

C

Mpredahfiygypkkghghsyttaeeaagigiltvilgvllligcwycrrrngyralmdkslhvgtq caltrrcpqegfdhrdskvslqekncepvvpnappayeklsaeqspppysphhhhhh***

Asterisks denote opal stop codon (tga).

Figure 1: **A)** pET9a24a plasmid map containing Syn-Melan-A. **B)** Plasmid map key highlighting purification, antibiotic resistance, and expression control features. **C)** Amino acid sequence.

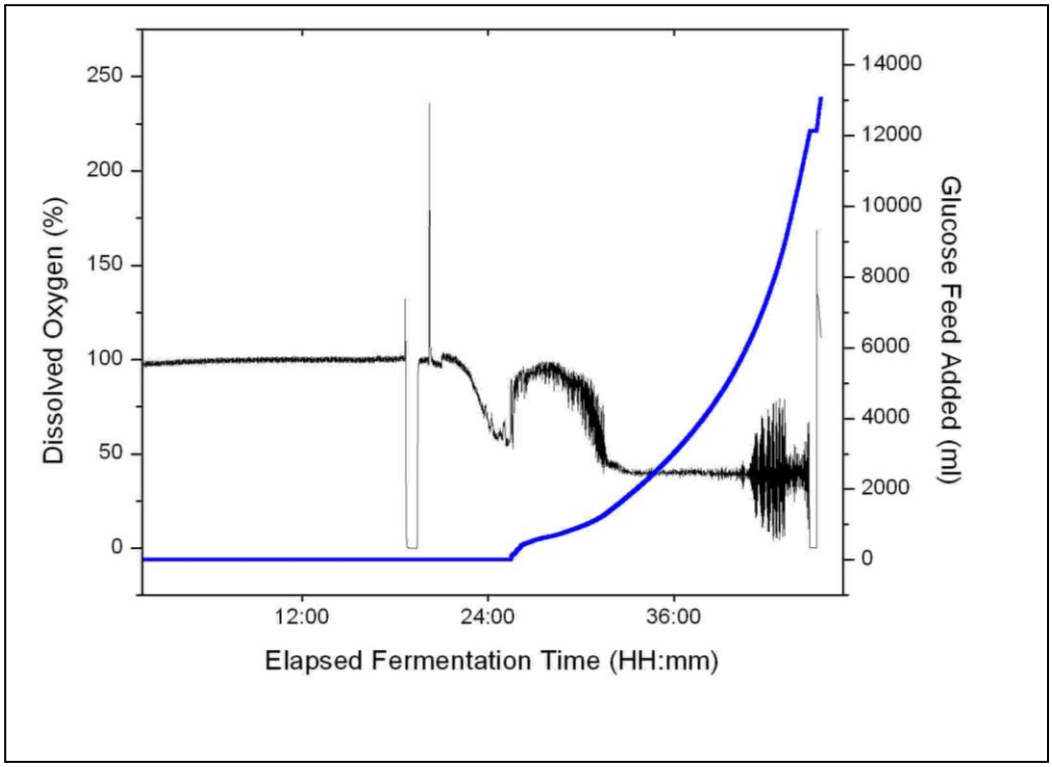

Figure 2: Fermentation profile for Melan-A. Dissolved oxygen concentration (black) follows the profile seen for pH stat control. Glucose feed (blue) increases exponentially at the conclusion of the batch phase of the fermentation

fermentation indicating consumption of glucose by the cells. DO concentration spiked 26 hours into the fermentation indicating an exhaustion of the carbon source in the media. The pH of the media changed due to an accumulation of ammonium ions after the depletion of the primary carbon source [24, 25]. This rise in pH triggered the addition of feed and was used to control the feed rate into the vessel. The glucose feed, containing IPTG, was introduced into the vessel at an exponential rate allowing for a constant growth rate during the induction process. The DO was maintained at 40% during the feed stage. The cells were deemed ready to harvest once the addition of feed did not cause an appreciable increase in the oxygen consumption rate. Fermentation completion reproducibly occurs 23 hours after inoculation.

Purification

The cells were pelleted and lysed immediately after harvest to obtain inclusion bodies containing Melan-A. The lysate was solubilized in phosphate buffer containing 8M urea, 1% Triton-114 and 2% w/v deoxycholate for 16 hours. The solubilized inclusion bodies were then filtered through a 1.2 µm and 0.5 µm low-protein binding capsule filter and loaded onto a 5L nickel column. Immobilized metal affinity chromatography (IMAC) was used as the initial purification column for Melan-A. The chromatogram in Figure 3A shows the results for the IMAC purification. Following a protocol developed previously by our group [8], the solubilized lysate was loaded onto the column (Figure 3AI) and subsequently washed with a solution of 8M urea, 2% w/v deoxycholate, and 1.0% v/v Triton X-114 (figure 3AII) to remove a significant amount of the endotoxin that is associated with the CT antigen. As described in our

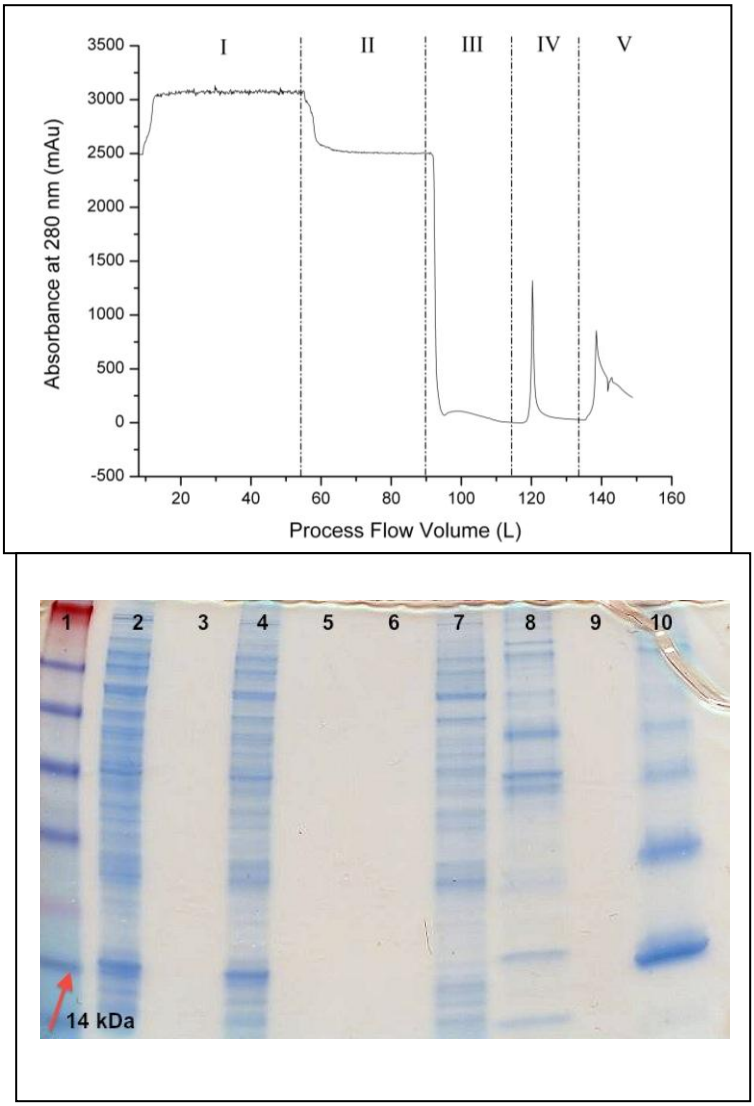

Figure 3: **A)** Immobilized metal affinity chromatography (IMAC) column chromatogram for Melan-A. Sections I-V correspond to load, deoxycholate wash, urea wash, low imidazole, and high imidazole respectively. **B)** Coomassie stained SDS-PAGE gel. Lanes 1-10 correspond to protein ladder, crude lysate, sample buffer (blank), filtrate (IMAC load), deoxycholate wash flow through, sample buffer (blank), IMAC load flow through, IMAC low imidazole, sample buffer (blank), and IMAC high imidazole. The red arrow indicates the Melan-A monomer band at 14 kDa.

previous reports, we determined that many CT-antigens bind the lipopolysacchrides produced by *E. coli* to high concentrations [8, 26]. For example, the CT-antigen NY-ESO-1 had endotoxin levels at 1,362.95 EU/µg prior to loading onto the IMAC column. Additionally NY-ESO-1 had latent endotoxin which gradually diffused out during storage if a detergent wash step was not included in the IMAC purification.[8] Melan-A solubilized inclusion bodies were found not to have as high of an endotoxin concentration as NY-ESO-1 (143.0 EU/µg in IMAC load). Even at these concentrations, the detergent wash step on the IMAC is essential to reduce endotoxin before the downstream columns. Table 1 details the endotoxin levels measured at several points in the purification process. Endotoxin was reduced to 0.00049 EU/µg in the IMAC High Imidazole elution. The majority of the endotoxin eluted with the host proteins in the load flow through (319.9 EU/µg) and in the deoxycholate wash step (15,000 EU/ml). Excess detergent was washed off of the column during the urea wash step. The detergents used in the previous step have a high 280 nm absorbance which plummeted after 1.5 column volumes of urea wash. A small amount of endotoxin is removed in this step with only a slight loss of protein (Table 1). Figure 3AIV-V shows the low and high imidazole fractions respectively. The quality of the IMAC purification was analyzed by Coomassie gel and Western blot. As shown in figure 3B, a large portion of the host proteins elute in the load flow through (lane 7). The deoxycholate wash removes a small fraction of target protein but as mentioned earlier it also removes a majority of the bound endotoxin (see Table 1). A faint 14 kDa band corresponding to the Melan-A monomer is seen in the low imidazole fraction indicating some loss of product during this step. Most of the product, however, elutes

Sample	Protein Concentration (mg/ml)	Volume (ml)	Total Protein (g)	Endotoxin Concentration (EU/µg)
IMAC Load	11.4	42000	478.8	143.0
IMAC Load Flow Through	5.13	41993	215.4	319.9
Deoxycholate Wash	--†	34860	--	15,000†
Urea Wash	< 0.025	24933	--	0.404
IMAC High	0.81	14985	12.2	0.00049
AXC Load Flow Through	0.04	3656	0.15	0.0675
AXC Elute	2.44	5000	~12	0.012
CXC Flow Through	1.89	6600	~12	0.013
Final Bulk Buffer Retentate	7.09	1390	9.8	0.0073
Filtered Final Bulk Melan-A	4.53	1388.6	6.3	0.0096

Table 1. Endotoxin and protein concentration measured during several points in the production process. Endotoxin limit is 1.4 EU/µg for a dose of 250 µg.

† Deoxycholate wash endotoxin concentration reported as EU/ml. Protein concentration by Bradford was inaccurate due to high levels of Triton X-114.

in the high imidazole fraction. The eluted product was concentrated to 1 L and buffer exchanged using tangential flow filtration (TFF) into 10 mM carbonate buffer for anion exchange chromatography.

In our previous report on the production of NY-ESO-1, we used an anion exchange column (AXC) as a flow though column followed by final polishing with a hydrophobic interaction column (HIC). During process development for Melan-A, the HIC column was deemed impractical for purification of Melan-A due to inefficient elution off of the column even with the addition of non-polar excipients. Additionally, detergent or alcohol removal after the HIC column is extremely difficult and results in a significant loss of product. Therefore, the downstream polishing column process was amended by converting the AXC into an elution column and replacing the HIC with a flow through cation exchange column. Figure 4A shows the chromatogram of the AXC purification. The retentate from the post-IMAC buffer exchange was loaded onto the column in a 70:30 dilution ratio (V/V) with carbonate buffer. This dilution step allowed for increased loading capacity of the column compared to undiluted load by increasing flow and preventing resin fouling at the top of the column. During development, the retentate was also found to be slightly lower than the desired pH after five diafiltration volumes. Loading at a lower pH would affect column performance due to the protein carrying a net positive charge at a pH below the isoelectric point reducing binding to the strong anion exchangers in the resin. Figure 4A-IV shows the elution of the product over six column volumes with carbonate buffer containing 1M NaCl. Figure 5A shows a Coomassie stained SDS-PAGE gel of samples from the AXC polishing step. The Melan-A monomer (14 kDa) is collected in

A

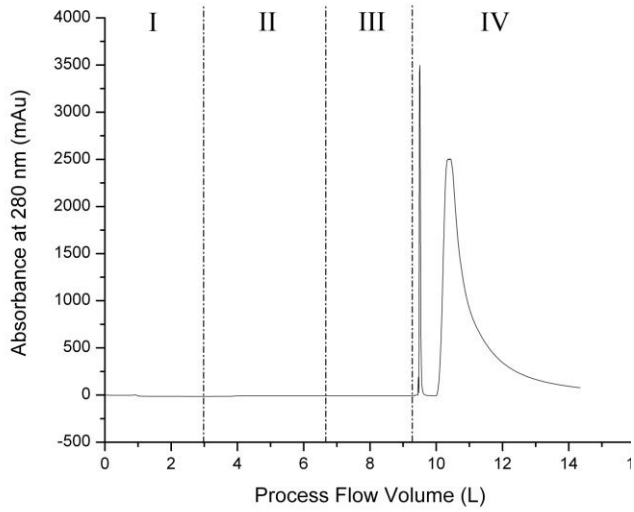

B

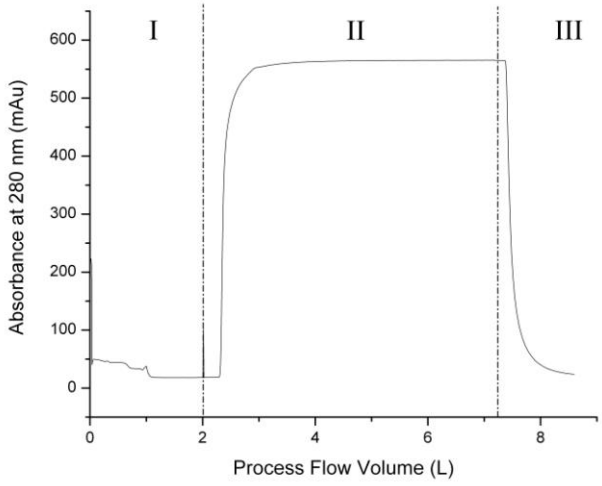

Figure 4: **A)** Chromatogram for anion exchange chromatography. Section I-III are column equilibration, load flow through and wash respectively. Section IV shows the elution peaks for Melan-A with 1M NaCl. **B)** Chromatogram for cation exchange chromatography. The antigen flows through the column in section II and the wash is completed in section III.

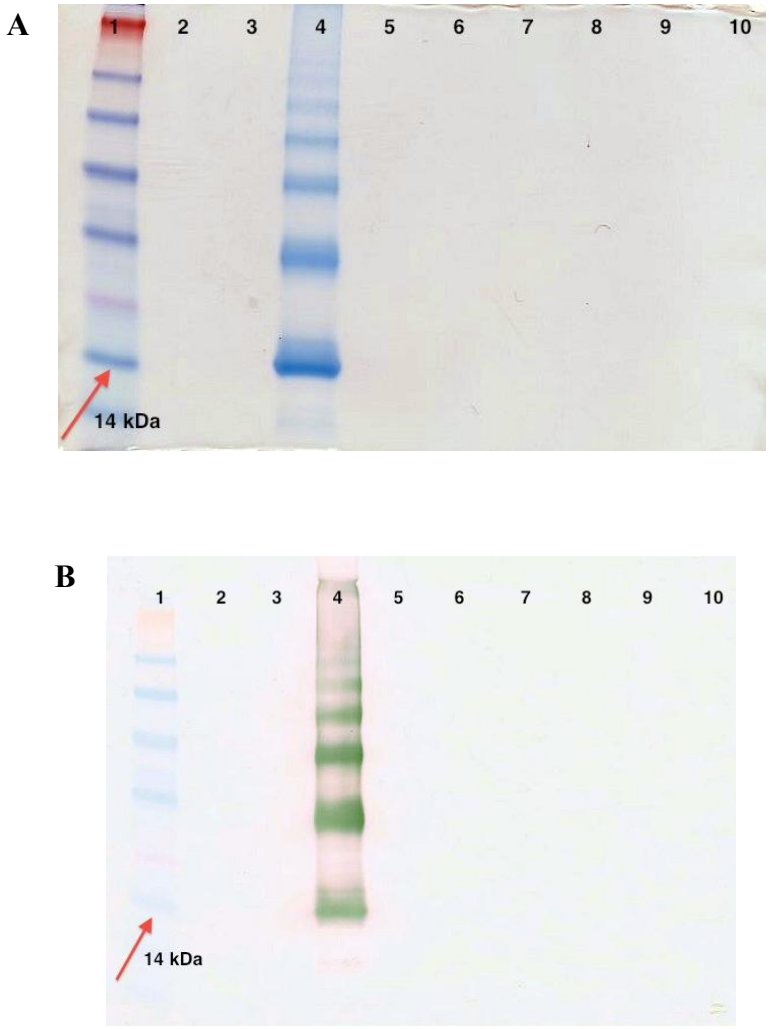

Figure 5: **A)** Coomassie stained SDS-PAGE gel for anion exchange column. Lanes 1-8 are as follows: protein ladder, sample buffer (blank), blank, AXC elute, blank, AXC load flow through, blank, AXC wash. **B)** Anti-Histidine western blot for anion exchange column. Lane assignments are as previously stated. A large band of Melan-A monomer is seen at the 14 kDa band. No detectable amount of Melan-A is seen in the AXC load flow through or wash.

the AXC elution. There was a 1% loss of total protein in the load flow through (Table 1) and no detectable loss of total protein in the wash step. Figure 5B shows a western blot (Anti-His) confirming the presence of the Melan-A monomer in the elution fraction and the absence of product in the previous fractions.

Figure 4B is the chromatogram for the cation exchange column (CXC). The column was equilibrated with two column volumes of the AXC elution buffer to ensure no binding to the column by the product. In this instance, the net negative charge of the protein and competition from other charged species would cause the product to flow through the cation resin. The product flow through was collected over 8 column volumes, which includes a 1.5 column volume washout step with AXC elution buffer. The CXC flow through was concentrated and buffer exchanged into the final formulation bulk buffer. Figure 6A and B show the Coomassie gel and western blot of the CXC column flow through and final bulk retentate. No product was lost in permeate during the final concentration step (lane 6). The product was subjected to dead-end sterile filtration through a 0.22 µm disk filter for final storage. Dead-end filtration resulted in a 35% loss in total protein (Table 1). A final summary Coomassie gel and western blot are shown in figure 7A & B. The IMAC provides a majority of the purification and endotoxin removal by including a deoxycholate wash in this step. The final columns serve to further reduce endotoxin levels and contaminants while limiting loss of product. The higher molecular weight bands that stain positive in the anti-histidine western blot are presumed to be Melan-A bound to chaperone proteins. Both DnaK and GroEL have been shown to be strongly associated with bacterial inclusion bodies (IB) and in the case of GroEL may play a role in the formation and

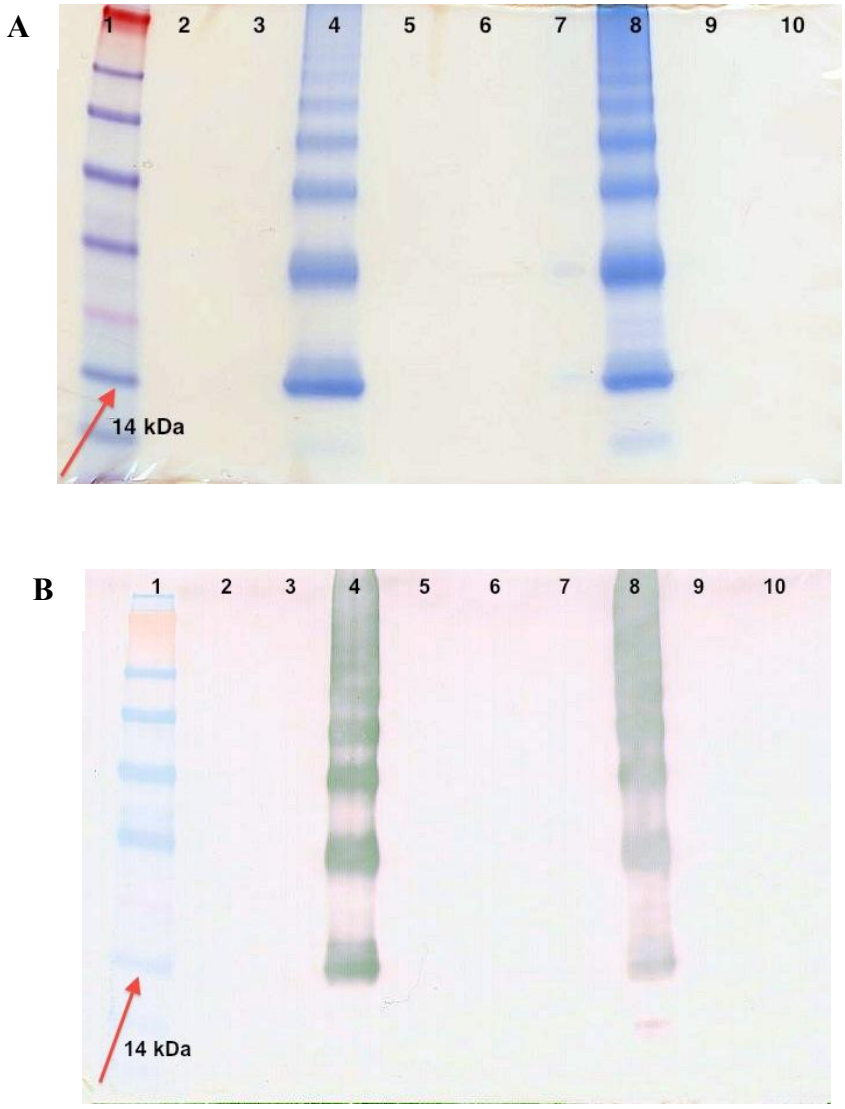

Figure 6: A) Coomassie stained SDS-PAGE gel for cation exchange chromatography and final buffer exchange. Lane assignments (1-8) are as follows: protein ladder, blank, blank, CXC flow through, blank, final concentration permeate, blank, final bulk retentate. B) Anti-Histidine western blot for CXC and final buffer exchange. Lane assignments are as previously stated.

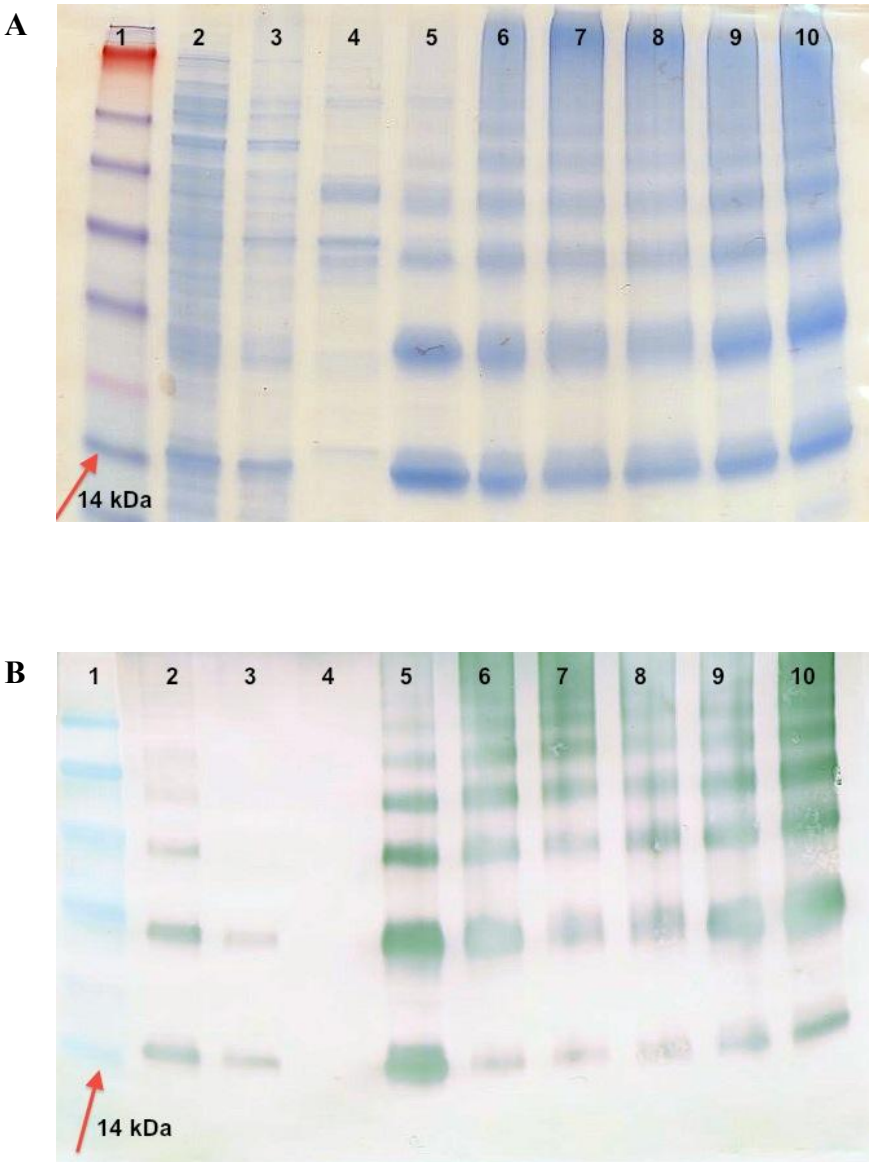

Figure 7: **A)** Coomassie stained SDS-PAGE gel summarizing GMP production of Melan-A. Lane assignments (1-10) are as follows: protein ladder, crude lysate, filtrate (IMAC load), IMAC low imidazole, IMAC high imidazole, post IMAC TFF retentate, AXC elute, CXC flow through, final bulk retentate, final filtered Melan-A**. B)** Anti-Histidine western blot of Melan-A summary gel. Lane assignments are as previously stated.

stability of IB[27-29]. Attempts to separate the chaperones from Melan-A proved to be unsuccessful despite using strong reducing agents (DTT), hydrophobic interaction chromatography, and varying the osmolarity of the buffer solutions (Unpublished Observations). The hydrophobicity of Melan-A may cause the chaperones to bind more tightly. A yield of 6.3 g was produced from half of the fermentation. Endotoxin levels in the final filtered product were less than 0.01 EU/µg. The final filtered product was two orders of magnitude below the LICR prescribed limit for endotoxin in a 250 µg dose.

Conclusion

GMP pilot scale production of Melan-A showed similar challenges to those seen in our previous report on NY-ESO-1 [8]. Melan-A is highly insoluble in aqueous solution and requires the presence of high concentrations of urea to stay in solution. Melan-A also has a strong affinity for endotoxin and like NY-ESO-1 requires a detergent wash step during IMAC purification to significantly reduce endotoxin levels before downstream purification. However, several modifications to purification process to tailor it to Melan-A resulted in higher yields per fermentation when compared to our previous work with NY-ESO-1. Additionally, endotoxin levels in the final bulk product were well below the specified limit for a 250 µg dose. Our final yield was 11.1 grams of protein from a twenty liter fermentation. This material meets the standards for use in phase 1 clinical trials.

References:

[1] K.J. Busam, A.A. Jungbluth, Melan-A, a new melanocytic differentiation marker. Adv Anat Pathol 6 (1999) 12-18.

[2] E. Balasse, G. Gatouillat, D. Patigny, M.C. Andry, C. Madoulet, In vivo anti-melanoma activities of the Melan-A/MART-1(101-115) T CD4+ cell peptide. Vaccine 27 (2009) 6107-6109.

[3] H.M. Berman, J. Westbrook, Z. Feng, G. Gilliland, T.N. Bhat, H. Weissig, I.N. Shindyalov, P.E. Bourne, The Protein Data Bank. Nucleic Acids Res 28 (2000) 235-242.

[4] P.G. Coulie, V. Brichard, A. Van Pel, T. Wolfel, J. Schneider, C. Traversari, S. Mattei, E. De Plaen, C. Lurquin, J.P. Szikora, J.C. Renauld, T. Boon, A new gene coding for a differentiation antigen recognized by autologous cytolytic T lymphocytes on HLA-A2 melanomas. J Exp Med 180 (1994) 35-42.

[5] Y. Kawakami, S. Eliyahu, C. Jennings, K. Sakaguchi, X. Kang, S. Southwood, P.F. Robbins, A. Sette, E. Appella, S.A. Rosenberg, Recognition of multiple epitopes in the human melanoma antigen gp100 by tumor-infiltrating T lymphocytes associated with in vivo tumor regression. J Immunol 154 (1995) 3961-3968.

[6] P. Chomez, O. De Backer, M. Bertrand, E. De Plaen, T. Boon, S. Lucas, An Overview of the MAGE Gene Family with the Identification of All Human Members of the Family. Cancer Research 61 (2001) 5544-5551.

[7] P. van der Bruggen, C. Traversari, P. Chomez, C. Lurquin, E. De Plaen, B. Van den Eynde, A. Knuth, T. Boon, A gene encoding an antigen recognized by cytolytic T lymphocytes on a human melanoma. Science 254 (1991) 1643-1647.

[8] A.J. Lowe, K.A. Anderson, C.L. Bardliving, C. Huang, Jr., L.M. Teixeira, L.M. Damasceno, G. Ritter, L.J. Old, C.A. Batt, Expression and purification of cGMP grade NY-ESO-1 for clinical trials. Biotechnology Progress n/a-n/a.

[9] C. Huang, Jr., K. Anderson, L. Damasceno, G. Ritter, L. Old, C. Batt, Improved secretion of the cancer-testis antigen SSX2 in <i>Pichia pastoris</i> by deletion of its nuclear localization signal. Applied Microbiology and Biotechnology 86 243-253.

[10] M.P. Bettinotti, C.J. Kim, K.H. Lee, M. Roden, J.N. Cormier, M. Panelli, K.K. Parker, F.M. Marincola, Stringent allele/epitope requirements for MART-1/Melan A immunodominance: implications for peptide-based immunotherapy. J Immunol 161 (1998) 877-889.

[11] X. Kang, Y. Kawakami, M. el-Gamil, R. Wang, K. Sakaguchi, J.R. Yannelli, E. Appella, S.A. Rosenberg, P.F. Robbins, Identification of a tyrosinase epitope recognized by HLA-A24-restricted, tumor-infiltrating lymphocytes. J Immunol 155 (1995) 1343-1348.

[12] L. Lopes, K. Fletcher, Y. Ikeda, M. Collins, Lentiviral vector expression of tumour antigens in dendritic cells as an immunotherapeutic strategy. Cancer Immunology, Immunotherapy 55 (2006) 1011-1016.

[13] M.S. Plog, C.A. Guyre, B.L. Roberts, M. Goldberg, J.A. St George, M.A. Perricone, Preclinical safety and biodistribution of adenovirus-based cancer vaccines after intradermal delivery. Hum Gene Ther 17 (2006) 705-716.

[14] A. Schutz, D. Oertli, W.R. Marti, C. Noppen, E. Padovan, G.C. Spagnoli, M. Heberer, P. Zajac, Immunogenicity of nonreplicating recombinant vaccinia expressing

HLA-A201 targeted or complete MART-1/Melan-A antigen. Cancer Gene Ther 8 (2001) 655-661.

[15] P. Zajac, D. Oertli, W. Marti, M. Adamina, M. Bolli, U. Guller, C. Noppen, E. Padovan, E. Schultz-Thater, M. Heberer, G. Spagnoli, Phase I/II clinical trial of a nonreplicative vaccinia virus expressing multiple HLA-A0201-restricted tumor-associated epitopes and costimulatory molecules in metastatic melanoma patients. Hum Gene Ther 14 (2003) 1497-1510.

[16] D. Lienard, M.F. Avril, F.A. Le Gal, P. Baumgaertner, W. Vermeulen, A. Blom, C. Geldhof, D. Rimoldi, S. Pagliusi, P. Romero, P.Y. Dietrich, N. Corvaia, D.E. Speiser, Vaccination of melanoma patients with Melan-A/Mart-1 peptide and Klebsiella outer membrane protein p40 as an adjuvant. J Immunother 32 (2009) 875-883.

[17] D.R. Leach, M.F. Krummel, J.P. Allison, Enhancement of antitumor immunity by CTLA-4 blockade. Science 271 (1996) 1734-1736.

[18] P. Shrikant, A. Khoruts, M.F. Mescher, CTLA-4 blockade reverses CD8+ T cell tolerance to tumor by a CD4+ T cell- and IL-2-dependent mechanism. Immunity 11 (1999) 483-493.

[19] A.M. Eggermont, A. Testori, M. Maio, C. Robert, Anti-CTLA-4 antibody adjuvant therapy in melanoma. Semin Oncol 37 455-459.

[20] A.R. Jazirehi, S. Baritaki, R.C. Koya, B. Bonavida, J.S. Economou, Molecular Mechanism of MART-1+/A*0201+ Human Melanoma Resistance to Specific CTL-Killing Despite Functional Tumor-CTL Interaction. Cancer Res.

[21] C.J. Huang, R.H. Chen, T. Vannelli, F. Lee, E. Ritter, G. Ritter, L.J. Old, C.A.

Batt, Expression and purification of the cancer antigen SSX2: a potential cancer vaccine. Protein Expr Purif 56 (2007) 212-219.

[22] J.F. Kane, Effects of rare codon clusters on high-level expression of heterologous proteins in Escherichia coli. Current Opinion in Biotechnology 6 (1995) 494-500.

[23] B. Miroux, J.E. Walker, Over-production of Proteins inEscherichia coli: Mutant Hosts that Allow Synthesis of some Membrane Proteins and Globular Proteins at High Levels. Journal of Molecular Biology 260 (1996) 289-298.

[24] B. Kim, S. Lee, S. Lee, Y. Chang, H. Chang, High cell density fed-batch cultivation of <i>Escherichia coli</i> using exponential feeding combined with pH-stat. Bioprocess and Biosystems Engineering 26 (2004) 147-150.

[25] T. Suzuki, T. Yamane, S. Shimizu, Phenomenological Background and Some Preliminary Trials of Automated Substrate Supply in pH-Stat Modal Fed-Batch Culture Using a Setpoint of High Limit. Journal of Fermentation and Bioengineering 69 (1990) 292-297.

[26] R.H. Chen, C. Huang, Jr., B.S. Newton, G. Ritter, L.J. Old, C.A. Batt, Factors affecting endotoxin removal from recombinant therapeutic proteins by anion exchange chromatography. Protein Expression and Purification 64 (2009) 76-81.

[27] M.M. Carrió, A. Villaverde, Role of molecular chaperones in inclusion body formation. FEBS Letters 537 (2003) 215-221.

[28] N. González-Montalbán, M.M. Carrió, S. Cuatrecasas, A. Arís, A. Villaverde, Bacterial inclusion bodies are cytotoxic in vivo in absence of functional chaperones DnaK or GroEL. Journal of Biotechnology 118 (2005) 406-412.

[29] M. Mar Carrio, A. Villaverde, Localization of Chaperones DnaK and GroEL in Bacterial Inclusion Bodies. Journal of Bacteriology 187 (2005) 3599-3601.